CHARACTERIZATION OF TIN CRYSTAL ORIENTATION EVOLUTION DURING THERMAL CYCLING IN LEAD-FREE SOLDER JOINTS

By

Bite Zhou

A DISSERTATION

Submitted to
Michigan State University
in partial fulfillment of the requirements
for the degree of

DOCTOR OF PHILOSOPHY

Materials Science and Engineering

2012

ABSTRACT

CHARACTERIZATION OF TIN CRYSTAL ORIENTATION EVOLUTION DURING THERMAL CYCLING IN LEAD-FREE SOLDER JOINTS

By

Bite Zhou

To address the long term reliability of lead-free solder joints in electronic devices during thermal cycling, the fundamental understanding of deformation mechanisms was studied using polarized light optical microscopy (PLM), electron backscatter diffraction (EBSD) in scanning electron microscopy (SEM), and synchrotron X-ray diffraction (XRD). Near-eutectic Sn-3.0(wt %) Ag-0.5(wt %) Cu (SAC305) lead-free solder joints were assessed in three different package designs: low-strain plastic ball grid array (PBGA), medium-strain fine-pitch ball grid array (BGA), and high-strain wafer-level-chip-scale package (WLCSP). The effect of microstructure evolution on solder failure is correlated with dislocation slip activities.

The major failure mode in lead-free solder joints during thermal cycling that causes the electrical failure of the device is cracking in the bulk Sn near the Si chip/solder interface. Microstructure and Sn grain orientation evolution usually precedes crack development. A combined approach of both statistical analysis of a large number of solder joints, and detailed studies of individual solder balls was used to investigate the causes of fracture. Sn crystal orientation evolution and its effect on deformation was characterized in solder joints with different thermal histories, and compared with those from other package designs with different effective strain levels. The relationship between the initial dominant and localized recrystallized Sn grain orientations on crack development was investigated. It is found that in the low-strain package design, cracking is strongly correlated with Sn grain orientations with the [001]

direction (*c*-axis) nearly aligned with the chip/solder interface. But no cracks were observed in solder balls with dominant orientations that have the *c*-axis normal to the interface plane.

In higher-strain packages, however, cracking occurred in a variety of Sn grain orientations, and even solder balls with dominant orientations that are resistant to facture in the low-strain package design cracked. Nevertheless, at the early stage of deformation in WLCSP samples, more dramatic plastic deformation and damage was observed in a row of solder balls with similar *c*-axis orientations (with the [001] direction nearly aligned with the interface plane).

Microstructure evolution preceding crack propagation is apparent in all package designs. Both continuous and discontinuous recrystallization processes were observed in solder joints after thermal cycling. More significant microstructure evolution and recrystallization occurred in higher strain package designs. Statistical analysis reveals that there is an increase in the number of high energy high angle grain boundaries and a decrease of low energy low angle and twin boundaries during thermal cycling. Crack propagation was facilitated by the high angle random boundaries developed during recrystallization, whereas the twin boundaries (with near 60 ° misorientation about the Sn [100] axis) were more resistant to cracking. The relative ease of the deformation of different Sn grain orientations also influenced crack development. Crack propagation was impeded by the hard orientations (with *c*-axis normal to the interface) that developed during continuous recrystallization.

The gradual lattice rotation during the continuous recrystallization process is correlated with dislocation slip on facile slip systems. Local concentration of elastic strain and orientation gradients inside a continuously recrystallized grain are correlated with slip activities, and locally recovered regions may become nucleation sites for the primary recrystallization upon further straining.

ACKNOWLEDGEMENTS

Part of this research was supported by Cisco Systems, Inc., San Jose, CA, by means of a Gift to the Michigan State University College of Engineering. The later part of the work was supported by NSF-GOALI Contract 1006656. Use of Advanced Photon Source was supported by the United State Department of Energy, Office of Science, Office of Basic Energy Sciences, under Contract No. DE-AC02-06CH11357.

I would like to express my sincere gratitude to my advisor, Dr. Thomas Bieler, who has always been nice and patient in guiding me through this work. His passion and enthusiasm for science and research stimulated my great interests in exploring this area in the first place. I am thankful for the many opportunities that he provided for me to present my work at the annual conferences, from where I started to establish my own networking in this field. It has been exciting to have insightful discussions with him, from time to time, thanks to his "open-door" policy.

I would also like to thank my dissertation committee members Dr. Martin Crimp, Dr. Andre Lee, and Dr. Farhang Pourboghrat for their valuable guidance and suggestions during my study. I appreciate the fruitful discussions we had during the metallurgy weekly group meeting with Dr. Martin Crimp, and the solder group meeting with Dr. Farhang Pourboghrat. I am also grateful for the advice from Dr. Andre Lee based on his many years of experience in the same research field.

My gratitude also goes to Dr. Tae-Kyu Lee at Cisco Systems, Inc., without whom this collaboration would not be a success. His consistently great support on experiments and

specimens is an essential part in finishing this work. I benefited a lot from his knowledge and experience. I would also like to thank Dr. Govindarajan Muralidharan at Oak Ridge National Laboratory (ORNL) for giving me an opportunity to utilize my expertise to solve a different problem through the summer internship at the ORNL. I thank Dr. Wenjun Liu, Dr. Ruqing Xu and Dr. Douglas Robinson for their assistance in the synchrotron X-ray diffraction experiments at the Advanced Photon Source at Argonne National Laboratory. I am also very grateful for the help and emotional support from my fellow graduate students, and all my friends. It has been great few years with you guys.

Finally, my deepest gratitude goes to my parents, my grandma, and Hongmei for their selfless love and support, for their understanding and forgiveness, and for their encouragements and belief in me. I would not have accomplished this without you.

TABLE OF CONTENTS

LIST OF TABLES

LIST OF FIGURES

CHAPTER 1

Introduction and literature review

1.1 Rationale

In the second-level interconnection in electronic devices, solder joints are used to mechanically support and electrically connect the Si chip (or chip carrier) to the printed wiring board (PWB) by means of pin-through-hole (PTH) and surface mount technology (SMT). Fabrication using PTH is done by wave soldering, in which solder joints are formed from a molten solder bath by filling a hole through capillary force. Surface mount technology, in contrast, involves a reflow process consisting of the following steps: 1) application of solder pastes and 2) heating up and cooling down using a controlled profile to form the solder interconnection [Abtew and Selvaduray (2000)].

Solder joints in an electronic package are often configured as a solder joint array, and the configuration (including the number of joints per package, the joint location, the ball pitch size, etc.) varies in different package designs. For instance, the ball grid array (BGA) design utilizes a full-matrix array or multiple rows (around the perimeter) of solder balls to achieve high input/output (I/O) densities. According to the chip-carrier substrate material, a BGA can be classified as plastic ball grid array (PBGA), ceramic ball grid array (CBGA), ceramic column grid array (CCGA), metal ball grid array (MBGA), or tape ball grid array (TBGA). In order to push the I/O density even higher, chip-scale-packaging (CSP) was proposed, and the size and weight of the devices were significantly decreased. In the CSP design, the electronic package body has the same or slightly larger size than the silicon die. In contrast, wafer-level packaging (WLP) involves fabricating the die and package on the Si wafer, and thus the package has the same size as the chip. This packaging technique is often referred to as wafer-level-chip-scale packaging (WLCSP) [Ulrich and Brown (2006)].

The eutectic Sn-37Pb (wt %) solder (with melting temperature 183 ℃) has been most widely used historically, particularly in consumer products [Kang and Sarkhel (1994), EPA (2005), Trumble (1998)]. Eutectic Sn-Pb solder alloy has sound reflow properties and good reliabilities. For instance, this alloy has a low wetting angle and interfacial energy with copper, which help produce a good metallic bonding between the solder and the substrate during the reflow process. Eutectic Sn-37Pb solder also has good balance of strength and ductility when subject to mechanical and thermal loadings [Zeng and Tu (2002), Trumble (1998), EPA (2005)]. However, in the past decades, concerns have been raised globally upon the potential threat of heavy metal Pb component in electronics, both to the environment and human health during the life-cycle and the disposal of these devices. The "Restriction of Hazardous Substances Directive" (RoHS 2002/95/EC), promoted by the European Union prohibited the use of Pb (and four other toxic substances) in new electrical and electronic devices after July 2006 [EPA (2005)]. This has served as a model for the rest of the world to eliminate Pb in the electronic packaging industry.

A variety of lead-free solder alloys have been studied to replace the eutectic Sn-Pb solder [Kang et al. (2005), Frear et al. (2001), Handwerker et al. (2007), Liu et al. (2011), Trumble (1998), Loomans and Fine (2000), Moon et al. (2000)]. It was suggested that Sn-3.9Ag-0.6Cu (wt %) is suitable for reflow, and Sn-0.7Cu (wt %) and Sn-3.5Ag (wt %) for wave soldering applications. Other alloy systems, for instance, Sn-Bi, Sn-In, Sn-Ag-Bi, were also assessed extensively as replacements for eutectic Sn-Pb solders [Glazer (1994), Kang and Sarkhel et al. (1994), Kang et al. (2005), Hua et al. (1998), Kattner and Boettinger (1994)]. Among these alloys, eutectic or near eutectic Sn-Ag-Cu (SAC) systems are often favored for their good reliability and solderability [Handwerker et al. (2007), Anderson (2007), Henderson et al. (2004)].

The ternary eutectic point and the microstructure of SAC alloys have been studied. It was found that the eutectic composition is close to Sn-3.5Ag-0.9Cu (wt %) and the liquidus temperature is approximately at 217 ℃ [Moon et al. (2000), Loomans and Fine (2000)]. More often, near eutectic SAC alloys Sn-(3.5-4) Ag-(0.5-1) Cu (wt %) are used and the liquidus temperature of near eutectic SAC alloys is between 217 ℃ and 220 ℃ with similar microstructure as the eutectic composition [Handwerker et al. (2007), Kang et al. (2005)]. This alloy system contains three phases upon solidification: β-Sn, Ag_3Sn, and Cu_6Sn_5 intermetallic compound (IMC) [Handwerker et al. (2007), Henderson et al. (2002)]. The primary plate-like Ag_3Sn and rod-like Cu_6Sn_5 phases, the Sn-rich dendrites, and the dispersed fine Ag_3Sn and Cu_6Sn_5 precipitates constitute the microstructure of the SAC alloy. Depending on the composition and cooling speed, the primary IMC phases can be effectively suppressed [Henderson et al. (2002)]. The solidification behavior of SAC alloys is described in detail later. Elimination of undesirable large plate-like primary Ag_3Sn phases was realized by lowering the Ag content to a hypoeutectic level [Henderson et al. (2002)], and this has led to widespread use of the Sn-3.0Ag-0.5Cu (SAC 305) alloy. In this dissertation, only the SAC 305 solder alloy composition was used, and it has been reported that this alloy has similar characteristics to the other SAC alloys [Handwerker et al. (2007)]. The effect of the alloy composition on solder properties (although important) is beyond the scope of this work.

The integrity of lead-free solder joints ensures the functionality of electronic devices, and the reliability of solder interconnections have been studied in a variety of aspects under different deformation conditions. The focus of this dissertation is on the fundamental understanding of the deformation behaviors leading to microstructural evolution in lead-free solder joints caused by the accelerated thermal cycling.

The cyclic change of temperature during thermal cycling introduces thermal strains on solder joints due to the mismatch of coefficient of thermal expansion (CTE) on two levels. At the microscopic-level, strain concentrations are found along grain boundaries due to the CTE mismatch from the intrinsic anisotropy in Sn, causing boundary sliding and/or decohesion [Henderson et al. (2004), Choi et al. (2000), Sundelin et al. (2008)]. At the package level, the CTE mismatch occurs between different components (Si chip or chip carrier, solder joints and PWB) in the electronic package, facilitating microstructural evolution and cracking in solder joints near the chip-side interface [Bieler et al. (2008), Yin et al. (2012), Chen et al. (2011), Terashima et al. (2004), Zhou et al. (2010)].

The reliability of solder interconnects due to high current density, corrosive environment, and high strain rate impact (drop) testing has also been assessed in the literature. The degradation of lead-free solder joints due to electromigration were studied [Lee et al. (2007), Lin et al. (2007), Lu et al. (2008), Chen et al. (2009), Lee K. et al. (2011)]. During electromigration, extensive transport of Cu and Ni leads to void formations in the intermetallic interfacial phases on both the chip and substrate side interfaces. The corrosion mechanism during an exposure to the moisture and other corrosives was assessed and correlated with the alloy composition [Abtew and Selvaduray (2000)] and the microstructure [Lee et al. (2011b)] of solder joints. Studies on the high strain rate impact testing on electronic packages have linked the deformation mechanism and failure behaviors of solder joints to the effect of the pre-aging condition, the board design, the relative strain levels, and the microstructure in solder joints [Peng and Marques

(2007), Noh et al. (2011), Zhu and Marcinkiewicz (2005), Lee et al. (2011c)]. Since the scope of this dissertation is to understand the microstructure evolution and its correlation with damage development during thermal cycling, deformation behavior in solder joints under this particular testing condition is discussed in greater detail as follows.

The major failure mode in lead-free solder joints (configured in the BGA or CSP packages) during thermal cycling that causes the electrical failure of the device is cracking in the bulk Sn phase near the chip-side interface. Microstructure and Sn crystal orientation evolution preceding crack propagation has been widely reported in the literature [Yin et al. (2012), Mattila and Kivilahti (2012), Mattila et al. (2010), Shnawah et al. (2012), Bieler et al. (2008), Zhou et al. (2010), Zhou et al. (2012b)]. Recovery and recrystallization processes change the original microstructure of the solder joint, which establishes a pre-condition for damage development. High angle grain boundaries developed during recrystallization facilitate crack propagation [Sundelin et al. (2008), Terashima et al. (2004), Bieler et al. (2008), Zhou et al. (2010)].

The microstructure evolution and damage development in solder joints during thermal cycling depends on several factors. First of all, the bulk Sn phase plays an important role in the response of solders to the thermal strain, and both the Sn grain orientation and grain boundary characteristics influence crack propagation. In the SAC lead-free solder alloy system, there are only a limited number of Sn grain orientations in one solder joint, and they tend to be either near single crystal or multi-crystalline [Henderson et al. (2004), Bieler et al. (2008), Park et al. (2007), Sundelin et al. (2008), and Yang et al. (2010)]. It has been reported in the literature that a strong correlation exists between the dominant Sn grain orientation and cracking [Bieler et al. (2008), Zhou et al. (2010)]. Secondly, grain boundary misorientation and rotation axis also affect damage development [Telang et al. (2006)]. It has been demonstrated that special boundaries are more effective in enduring damage propagation, whereas high angle random boundaries are more susceptible to cracking [Terashima et al. (2009), Matin et al. (2005)].

The rate of microstructure evolution also depends on the interaction between the package design and the pre-aging conditions. During thermal cycling, different cumulative strain/stress levels arise from various package designs and Si die configurations [Lee et al. (2011)]. It has been reported that in the higher strain package design, more severe degradation to the lifetime of solder joints was observed during thermal cycling due to the pre-aging effect [Lee et al. (2012)]. The annealing process during the pre-aging treatment alters the morphology and the distribution of dispersed intermetallic compound (IMC) particles in the solder joints. The coarsening of these particles apparently accelerates the Sn grain boundary mobility due to less effective pinning on dislocation movements [Qasaimeh et al. (2011), Bieler et al. (2012)]. In other words, with no pre-aging treatment, the fine IMC particles are able to retard microstructural evolution by hindering Sn grain boundary movements during recrystallization [Shanawah et al. (2012), Terashima et al. (2009)].

To address the plastic responses of lead-free solder joints to the cyclic thermal straining during thermal cycling, the activity of Sn slip systems is of great interest [Matin et al. (2006), Zhou et al. (2010)]. Studies on the active slip systems based upon the slip trace analysis depend on known Sn crystal orientations [Zhou et al. (2009b)]. Sn grain orientation can be qualitatively assessed using polarized light microscopy (PLM) [Lehman et al. (2010), Telang et al. (2004), Seo et al. (2009)], or quantitatively measured by electron backscatter diffraction (EBSD) [Bieler et al. (2008), Chen et al. (2011), Terashima et al. (2004b)]and synchrotron X-ray diffraction (XRD) [Bieler et al. (2009b), Lee et al. (2007), Zhou et al. (2012, 2012b)]. The effects of Sn grain orientation and grain boundary characteristics on the failure mechanisms of solder joints during thermal cycling are discussed in detail in this dissertation.

In the following sections in Chapter 1, background knowledge for the current work is introduced and reviewed, and three characterization techniques identified above are discussed. Microstructure evolution and damage development in solder joints during thermal cycling will be characterized in detail. Work completed and published while completing this study contributes to this introductory description, particularly references indicated by Lee, Zhou, or Bieler from 2009 to 2012. Hence, the focus of this dissertation in Chapters 2-5 is built upon the foundation laid in several prior publications, specifically [Zhou et al. (2009, 2009b, 2010), Lee et al. (2009, 2011]. Some of the newer papers contain information that is presented and discussed in greater detail in the later chapters of this dissertation [Zhou et al. (2012b), Bieler et al. (2012), Lee et al. (2012b)].

Chapter 2 describes the materials and the experimental set-ups, as well as the parameters used for data post-processing. The method used for slip-trace analysis and calculation of Schmid factors is also explained in detail.

Chapters 3 through 5 characterize the Sn crystal orientations and their correlation with the microstructure evolution and fracture in the low-strain PBGA, medium-strain fine-pitch BGA, and high-strain WLCSP package designs, respectively. The effect of varying strain levels on Sn crystal orientation evolutions is studied using statistical analysis and detailed analysis of selected joints. The deformation mechanism and fracture modes are discussed for each design.

Chapter 6 concludes this dissertation and discusses potential further work.

1.2 Sn anisotropy in SAC lead-free solders

SAC lead-free solder alloys consist of β-Sn phase, Ag_3Sn, and Cu_6Sn_5 intermetallic compound (IMC) phases. The β-Sn has a body-centered tetragonal (BCT) crystal structure with lattice parameters a=b=0.583 nm, c=0.318 nm with $c/a \approx 0.545$ [Lyman (1961)]. Four atoms reside at (0, 0, 0), (0.5, 0.5, 0.5), (0, 0.5, 0.25) and (0.5, 0, 0.75) positions, as shown in Figure 1.1. The Ag_3Sn phase has an orthorhombic crystal structure with lattice parameters a=0.597, b=0.478, c=0.518 nm [Sidhu et al. (2007)]. The low-temperature η'-Cu_6Sn_5 has a monoclinic structure (C_2/c) with a=1.1022 nm, b=0.728 nm, c=0.983 nm, and β=98.84 ° [Larsson et al. (1994)]. The high-temperature modification η-Cu_6Sn_5 phase has a hexagonal cell with a=0.419 nm and c=0.5086 nm [Westgren and Phragmén (1928)]. As discussed earlier, the focus of this work is on the β-Sn phase.

Nucleation of the β-Sn phase is difficult in a small volume solder joint, and a large undercooling (15 °-80 °C) is often required [Henderson et al. (2002), Kinyanjui et al. (2011), Kang et al. (2003), Arfaei et al. (2011), Lehman et al. (2004)]. To understand the solidification behavior of the SAC alloy system, a three-dimensional representation of the liquidus surfaces of the Sn and IMC phases in the Sn-rich region of the ternary phase diagram is shown in Figure 1.2 [Borgesen et al. (2007)]. For a particular near-eutectic SAC alloy (Sn-3.9Ag-0.6Cu), the idealized cooling trajectory is marked by the red arrows. Along this path, the primary plate-like Ag_3Sn phase forms first, followed by the β-Sn phase, and the final solidification occurs at the eutectic point. However, to better reflect the effect of undercooling, the liquidus surfaces are extrapolated to lower temperatures in Figure 1.2, and a more realistic cooling path is shown by white arrows. Following this trajectory, as the undercooling increases, the remaining liquid becomes even more Sn-rich as the Ag and Cu are consumed to form IMC phases [Borgesen et al. (2007)]. Due to the high enthalpy of fusion, recalescence occurs when the Sn phase nucleates in the undercooled Sn-rich liquid environment, and the released heat can then re-melt the nuclei, and thus suppress the nucleation of multiple Sn grains [Moon et al. (2000), Henderson et al. (2004)].

Upon nucleation, the β-Sn phase grows by a dendritic growth mechanism, and the direct effect of a large undercooling is a rapid growth of the Sn dendrites [Gong et al. (2009), Henderson et al. (2004)]. Given that an individual Sn dendrite may be hundreds of microns in size, the Sn grain size in a solder ball is largely influenced by the Sn dendrites [Gong et al. (2009)]. Consequently, recalescence and a large undercooling contribute to a rapid dendritic growth from only a few nuclei and thus a limited number of Sn grains are present in the SAC alloy system. As reported in the literature, the Sn grains in the SAC solder alloys tend to form either a near single crystal, a tri-crystal consisting of cyclic solidification twins, or in rare cases a multi-grain structure [Henderson et al. (2004), Bieler et al. (2008), Park et al. (2007), Sundelin et al. (2008), Yang et al. (2010)]. Therefore, due to the limited number of Sn grains present in the solder joint, the anisotropy of the Sn phase needs to be emphasized.

Various Sn properties exhibit anisotropy, as summarized in Table 1.1. The anisotropy in the diffusion coefficients of Cu and Ni in Sn has a big impact in the reliability of lead-free solder joints during electromigration [Lee K. et al. (2011), Lu et al. (2008)]. In the context of the thermal cycling condition, the anisotropy in CTE and elastic modulus is of great importance with regard to the elastic responses of solders to a cyclic change of temperature. The CTE value in the *c*-axis and *a*-axis differs by a factor of two. The *c*-axis has a CTE of $30.5 \times 10^{-6}/℃$ and the

CTE in the *a*-axis is 15.6×10^{-6}/ ℃. Young's modulus also varies in different crystallographic directions. As described earlier, in the BGA and CSP assembly, solder balls are used to mechanically support and electrically connect the Si chip (or chip carrier) to the PWB. When the electronic device is subject to a cyclic change of temperature, the CTE mismatches between different components in the devices impose strain upon the solder joints.

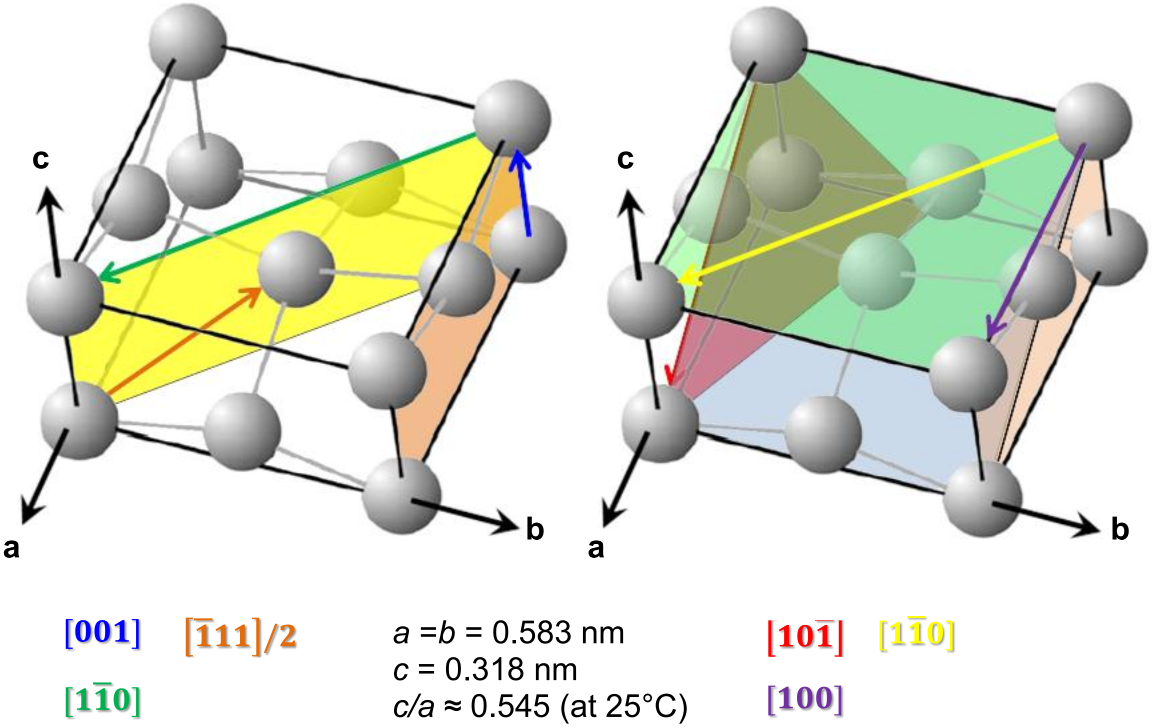

Figure 1.1 Sn unit cell showing a body-center tetragonal crystal structure with the lattice parameters in the inset; slip directions are listed and marked by the corresponding colored lines; selected slip planes are highlighted by different colors: the (110) in yellow, (010) plane in light orange, (101) in light blue, and (121) in red [adapted from Lee et al. (2010)]. For interpretation of the references to color in this and all other figures, the reader is referred to the electronic version of this dissertation.

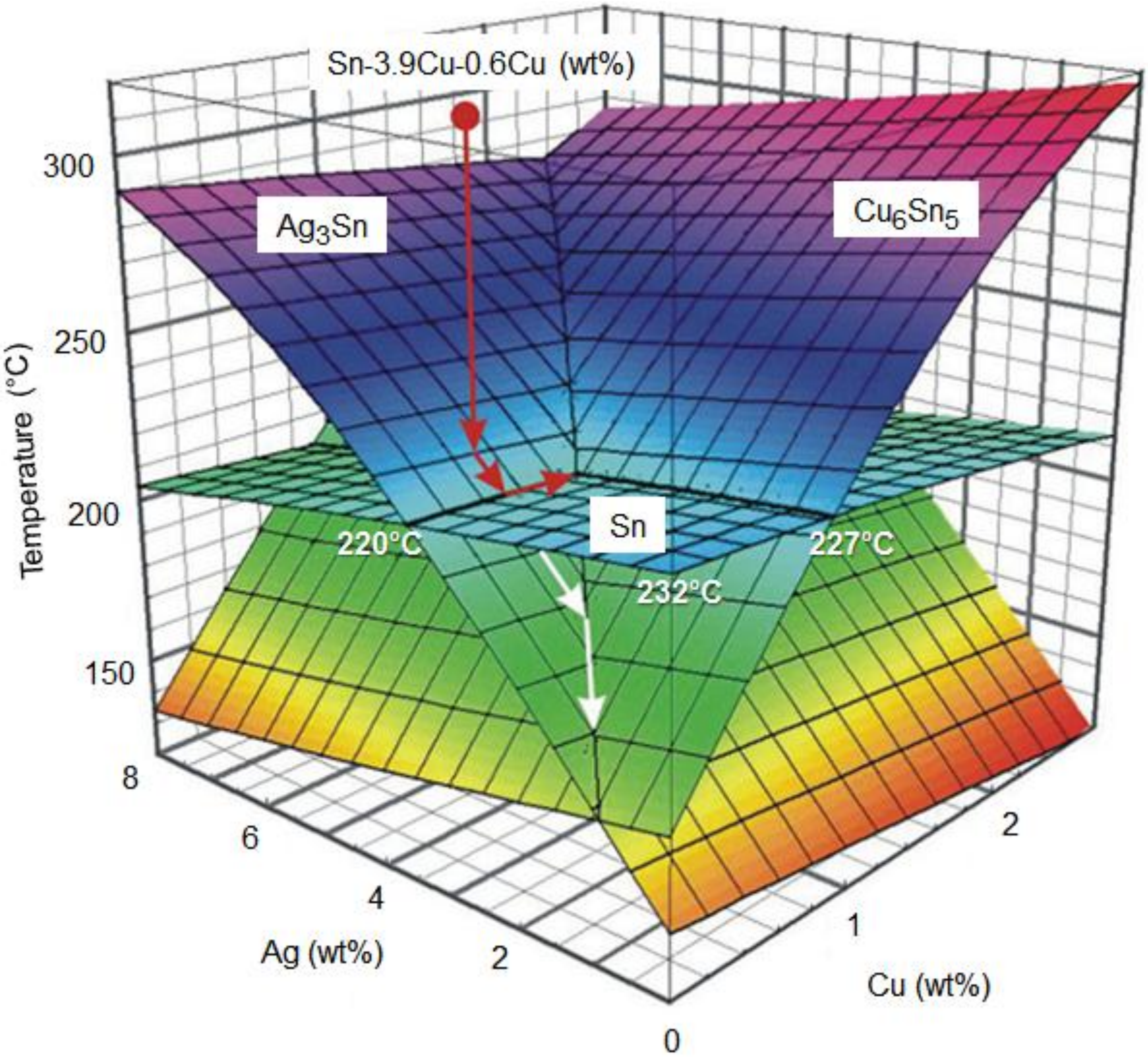

Figure 1.2 A three-dimensional representation of the liquidus surfaces of the Sn, Ag_3Sn, and Cu_6Sn_5 phases in the Sn-rich portion of the Sn-Ag-Cu ternary phase diagram. The liquidus surfaces are extended to lower temperatures to reflect the undercooling. Two cooling trajectories show the idealized (red arrows) and a more realistic (white arrows) solidification process for the Sn-3.9Ag-0.6Cu (wt %) alloy [adapted from Borgesen et al. (2007)].

Table 1.1 Anisotropic properties in Sn

	Lattice parameter (nm)	**CTE (10^{-6}/ ℃) (27 ℃)**	**Young's Modulus (GPa) (27 ℃)**	**Diffusivity Cu in Sn (27 ℃)**	**Diffusivity Ni in Sn (120 ℃)**
Sn <100]	0.583	15.4	23	$\sim 4\times 10^{-9}$ cm^2/sec	$\sim 1.3\times 10^{-9}$ cm^2/sec
Sn <001]	0.318	30.5	67	$\sim 2\times 10^{-6}$ cm^2/sec	$\sim 8\times 10^{-5}$ cm^2/sec

Lyman (1961), Lee et al. (2002), Bieler et al. (2008),

Telang et al. (2004b), Dyson et al. (1967), Yeh and Huntington (1984)

Shear strain is introduced on the solder joint due to the package-level CTE mismatch and the sense of shear is parallel to the interface plane from the solder ball to the geometric center of the package. The distribution of CTE-induced shear strain is heterogeneous due to varying CTE values from different components in the electronic package. For instance, larger CTE mismatch occurs at the chip-side interface, and the mismatch becomes more dramatic when the solder joint is directly attached to a Si chip with a CTE value of 2.6×10^{-6}/ ℃ at 27 ℃ [Lyon et al. (1977)]. Depending on the Sn grain orientation, the CTE mismatch at the chip-side interface varies by a factor of two: mismatch from 12.8×10^{-6}/ ℃ (when the Sn *a*-axis is aligned with the interface) to 27.9×10^{-6}/ ℃ (when the Sn *c*-axis is aligned with the interface). At the board side interface, CTE mismatch between the solder joint and the commonly used woven glass reinforced epoxy FR-4 (NEMA grade) PWB is much smaller. The CTE for the FR-4 on the interface plane (noted X/Y CTE) has varying values for different types, but they are mostly within the range of $12\text{-}16 \times 10^{-6}$/ ℃ when the temperature is between 40 ℃ and 125 ℃ [Coombs (2008)]. Consequently, depending on the Sn grain orientation, the CTE mismatch at the PWB side interface will yield a value approximately between 0 (when the Sn *a*-axis is nearly aligned with the interface) and 18.5×10^{-6}/ ℃ (when the Sn *c*-axis is aligned with the interface), which is lower than the chip-side interface. During thermal cycling, it is expected that larger strain accumulation and damage occur in the solder ball on the chip-side, which has been confirmed with experimental observations [Terashima et al. (2004, 2009), Lee et al. (2009)].

Aside from the shear strain, solder joints also experience tensile/compressive strain with a cyclic change of temperature due to the difference in Sn crystal orientations between neighboring joints [Bieler et al. (2008, 2012)]. The differential CTE normal to the chip-side interface between the neighboring joints can impose uniaxial strain in addition to the shear strain arisen from the ball position in the solder array. Therefore, for each solder joint, the induced thermal strain state during thermal cycling is complex, which is a function of the Sn grain orientation of the joint, its neighboring joints, and its relative position in the solder array. Generally speaking, each solder ball is a special case when there are only a few grains present in the joint, and the stress history is different from one joint to another [Bieler et al. (2012)].

1.3 Slip systems and dislocation activities in Sn

Upon thermal cycling, the intrinsic (between different Sn grain orientations) and extrinsic (between different components in the package) CTE mismatch introduce a complex strain state on the solder joint, during which plastic deformation occurs. To understand how solder responses plastically during a thermomechnical deformation, the activity of Sn slip systems needs to be addressed. Commonly used lead-free solders (particularly SAC alloys) contain more than ninety-five weight percent Sn, and the slip behavior of pure Sn servers as a good reference.

According to Fujiwara and Hirokawa (1987) and Bieler et al. (2008), commonly observed Sn slip systems can be categorized into ten slip system families in terms of relative activity. Slip in the Sn $\langle 001]$ direction on $\{100)$ and $\{110)$ types of planes are most facile (left in Figure 1.1). In contrast, slip in the $\langle 01\bar{1}]$ direction on $\{011)$ and $\{211)$ planes are less active (right in Figure 1.1). However, contradictory results regarding active Sn slip systems exist in the literature. A summary of published results is shown in Table 1.2, and the mixed brackets $\{hkl)\langle uvw]$ indicate tetragonal crystal symmetry [Bieler and Telang (2009)]. Table 1.2 is populated according to the relative activity of different slip systems from the easiest to the least active. This ranking is based upon the theory of forest dislocations acting as obstacles to dislocation movements [Fujiwara and Hirokawa (1987), Bieler et al. (2008)].

Table 1.2 Commonly observed Sn slip systems (CRSS with a superscript star is an estimated value from [Matin et al. (2006)])

SS family		**CRSS (MPa)**	**References**
#1	$\{100)\langle 001]$	1.9	[Obinata and Schmid (1933), Fiedler and Lang (1972), Fiedler and Vagera (1975)]
#2	$\{110)\langle 001]$	1.3	[Chu and Li (1979), Sidhu and Chawla (2008), Matin et al. (2006), Obinata and Schmid (1933), Fiedler and Lang (1972), Fiedler and Vagera (1975)]
#3	$\{100)\langle 010]$	3.3*	[Chu and Li (1979), Weertman and Breen (1956), Ojima and Hirokawa (1983), Düzgün et al. (1999), Düzgün and Aytaş (1993), Nagasaka (1989), Honda (1978)]
#4	$\{110)\langle 1\bar{1}1]/2$	2.3*	[Chu and Li (1979), Weertman and Breen (1956), Honda et al. (1979), Matin et al. (2006), Nagasaka et al. (1989), Fiedler and Lang (1972), Fiedler and Vagera (1975)]
#5	$\{110)\langle 1\bar{1}0]$		[Weertman and Breen (1956)]
#6	$\{010)\langle 101]$	3.8*	[Düzgün et al. (1999), Düzgün and Aytaş (1993), Fujiwara and Hirokawa (1987), Nagasaka et al. (1989), Fiedler and Vagera (1975)]
#7	$\{001)\langle 100]$		[Telang et al. (2007), Fiedler and Vagera (1975)]
#8	$\{001)\langle 110]$		[Telang et al. (2007)]
#9	$\{101)\langle 10\bar{1}]$	1.6	[Sidhu and Chawla (2008), Obinata and Schmid (1933), Fiedler and Vagera (1975), Düzgün and Aytaş (1993)]
#10	$\{121)\langle \bar{1}01]$	1.7	[Düzgün et al. (1999), Sidhu and Chawla (2008), Matin et al. (2006, 2007), Fiedler and Vagera (1975), Düzgün and Aytaş (1993)]

Slip systems $(211)[\bar{1}11]/2$, $(101)[\bar{1}11]/2$, and (101)[010] were also reported in [Fiedler and Vagera (1975)], as discussed in the text.

A similar yet different ranking was reported, in which the relative activity of slip systems is studied based on the calculated elastic energy of dislocations belonging to different slip systems [Fiedler and Vagera (1975)]. The relationship between the choice of slip systems and the elastic energy of dislocations was assessed in different materials based on the “criterion of minimum dislocation energy”. Generally speaking, the choice of slip systems may be determined by the energy increase to produce the dislocations required for continued deformation, or by the stress required to move the dislocations against the resistance of the crystal lattice [Foreman and Lomer (1955), Tyson (1967)]. Adopting this criterion in the study of Sn slip systems, Fiedler and Vagera (1975) assessed eleven Burgers vector and plane combinations, and the elastic energy was calculated for dislocations on five of the most closely packed planes in Sn. Among the list, all ten slip systems except $\{110)\langle 1\bar{1}0]$ (slip system #5) and $\{001)\langle 110]$ (slip system #8) in Table 1.2 were examined. In addition, dislocations associated with $(211)[\bar{1}11]/2$, $(101)[\bar{1}11]/2$, and (101)[010] slip systems were also studied.

It was found that dislocations with the Burgers vector [001] lying on (100) or (110) planes have the lowest elastic energy, followed by $[\bar{1}11]/2$ on (110). This suggests that glide on slip systems $\{100)\langle 001]$ (#1) and $\{110)\langle 001]$ (#2) may be the easiest. Among the list in [Fiedler and Vagera (1975)], those that were experimentally verified to be active slip systems are slip systems #1, #2, $\{110)\langle 1\bar{1}1]/2$ (#4), $\{101)\langle 10\bar{1}]$ (#9), $\{010)\langle 101]$ (#6), and $\{121)\langle \bar{1}01]$ (#10), from the lowest to the highest elastic energy. Although slip system $\{100)\langle 010]$ (#3) had not been reported as an active slip system prior to the study by Fiedler and Vagera (1975), it has been frequently reported in more recent publications (Table 1.2), and based on its calculated elastic energy, this slip system ranks between #4 and #9. The less active slip systems #3, #6, and #9 were also reported in [Zhou et al. (2009b)]. Although listed in Fiedler and Vagera (1975), three additional slip systems $(211)[\bar{1}11]/2$, $(101)[\bar{1}11]/2$, and (101)[010] are not commonly observed in the literature. Nevertheless, it is consistent that slip systems #1 and #2 are the most facile, and #10 is the least facile. It is important to note that other factors may change this ranking, and one of them is temperature. The effect of temperature and dislocation reactions on the activity of slip systems will be reviewed briefly later.

The relative ease of slip on different systems can also be evaluated by their critical resolved shear stress (CRSS). CRSS values listed in Table 1.2 are from [Matin et al. (2006)]. Numbers with a superscript star are estimated assuming the ratio of the CRSS of different co-planar slip systems is the same as the ratio of their linear atomic density in the slip direction (a similar method used in [Tyte (1938)]). Hence, the CRSS of slip system $\{110)\langle 1\bar{1}1]/2$ (#4) can be estimated from the coplanar slip system $\{110)\langle 001]$ (#2). Based on the CRSS values in Table 1.2, slip systems $\{110)\langle 001]$ (#2), $\{101)\langle 10\bar{1}]$ (#9), $\{121)\langle \bar{1}01]$ (#10), and $\{100)\langle 001]$ (#1) are the most active, whereas slip system $\{110)\langle 1\bar{1}1]/2$ (#4), $\{100)\langle 010]$ (#3), and $\{010)\langle 101]$ (#6) are less active. It is important to note that the measurement of CRSS (τ_{CRSS}) of slip systems are greatly affected by the purity of the Sn crystal, the amount of prior strain, and the temperature at which it is measured [Matin et al. (2006), Düzgün et al. (1999)]. Consequently, CRSS may not be reliable in estimating the relative activities of slip systems, and the temperature effect on the CRSS is discussed as follow.

The temperature dependence of the CRSS is different for different slip systems. For instance, Nagasaka (1989) reported that the CRSS of slip system $\{110)\langle 1\bar{1}1]/2$ (#4) decreases exponentially with rising temperature within the range from 160K-435K. In contrast, slip system $\{100)\langle 010]$ (#3) was operative in a large temperature range. The CRSS of this system shows a plateau between 320K and 380K, whereas in other temperatures ranges, it varies nearly exponentially. Slip system $\{010)\langle 101]$ (#6) was observed to be operative at low temperature, and the CRSS of this system is insensitive to temperature. However, instead of thinking of CRSS, when measuring the relative activity of slip systems based upon the passage rate of dislocation through forest dislocations (the method used in [Fujiwara and Hirokawa (1987)]), the operation of slip system $\{010)\langle 101]$ (#6) is likely to be influenced by temperature between 0K to 480K.

Aside from the CRSS, Matin et al. (2006) also suggested using effective yield strength (EYS), defined as the CRSS over the Schmid factor for different slip systems (τ_{CRSS}/m), to evaluate their relative activity. Higher activity is expected in a particular slip system when the EYS value is smaller. The EYS depends on both the values of CRSS and Schmid factor (which varies with the stress state and the crystal orientation), and it is not suitable for general assessments of different slip systems. Hence, the values of EYS are not listed in this review.

It is noted in Table 1.2 that controversial results were reported in the literature regarding the relative activity of slip systems $\{101)\langle 10\bar{1}]$ (#9) and $\{121)\langle \bar{1}01]$ (#10). For instance, slip systems #9 and #10 rank lowest in Table 1.2, suggesting that they are less facile. However, these two also have comparable or even lower CRSS than the highest ranking slip systems $\{100)\langle 001]$ (#1) and $\{110)\langle 001]$ (#2), indicating higher activities of slip system #9 and #10. In some cases, slip system #10 was verified to be active with low calculated EYS in both mechanical [Matin et al. (2006)] and thermomechanical fatigue experiments [Matin et al. (2007), Sidhu and Chawla (2008)]. In contrast, also with low EYS, slip systems that rank higher in Table 1.2 (and thus more active than slip system #10) were not observed to be operative. In other cases, however, slip system #10 may be less facile. For instance, [Bieler and Telang (2009)] showed a good agreement between the experiment and simulation when slip in slip systems #9 and #10 were suppressed, suggesting that these slip systems may be less active.

Even though slip systems $\{101)\langle 10\bar{1}]$ (#9) and $\{121)\langle \bar{1}01]$ (#10) were reported to be more active than slip systems $\{100)\langle 001]$ (#1) and $\{110)\langle 001]$ (#2) in some cases, the later were more frequently observed to be the most active slip systems [Tyte (1938)]. As suggested in [Tyte (1938)], the operation of slip systems #1 and #2 was accounted for the deformation when the elastic limit was once reached, and slip in slip system #9 and #10 followed that when the secondary critical load and temperature condition was met. This was further confirmed by the results from [Obinata and Schmid (1933)], in which slip in the [001] direction on either (100) or (110) plane (slip systems #1 or #2) was responsible for most slip activities, and only in rare cases were slip systems #9 and #10 operative.

The varying activities of slip system $\{121)\langle \bar{1}01]$ (#10) may be attributed to the effect of temperature and experimental conditions. Düzgün and co-workders [Düzgün et al. (1999)] observed that within samples with similar crystal orientations, this slip system was found to be operative only in specimens deformed at high temperatures (373K and 383K). Also as discussed earlier, this slip system was active during the mechanical or thermomechanical fatigue deformation. Consequently, it is speculated that in order to activate this slip system, energy barrier needs to be overcome either by raising temperature and/or with more energy input (for instance, cyclic loading in fatigue tests).

Unlike slip system $\{121)\langle \bar{1}01]$ (#10), the activity of slip system $\{101)\langle 10\bar{1}]$ (#9) may not be significantly affected by temperature, but it is rather influenced by the dislocation reaction and/or interaction with other slip systems. For slip system #9, [Fiedler and Vagera (1975)] suggested relatively high elastic energy for dislocations associated with this slip system.

However, slip in this system was still observed in some cases (Table 1.2). The following dislocation decomposition may have occurred, as proposed in [Fielder and Vagera (1975)], which leads to two dislocations with lower energy Burgers vectors.

$$[\bar{1}01] \rightarrow \frac{1}{2}[\bar{1}11] + \frac{1}{2}[\bar{1}\bar{1}1]$$

If this reaction occurs, dislocations associated with slip system #9 will instead have a $\langle 111]/2$ type Burger vector glide on a $\{101)$ type plane. However, given that $(101)[\bar{1}11]/2$ is not a commonly observed slip system, it is unclear whether the proposed dislocation reaction could increase the activity of this slip system. Nevertheless, the elastic energy of dislocations associated with this system was calculated in [Fielder and Vagera (1975)], and it ranks between slip systems $\{110)\langle 1\bar{1}1]/2$ (#4) and $\{100)\langle 010]$ (#3).

Another dislocation reaction that produces low-energy Burgers vectors results in a different ease of slip between slip systems $\{100)\langle 010]$ (#3) and $\{110)\langle 1\bar{1}1]/2$ (#4). Honda et al. (1987) illustrated the split reaction of a single dislocation gliding on slip system #3 into two dislocations in slip system #4, as shown below.

$$(010)[100] \rightarrow \frac{1}{2}(\bar{1}10)[111] + \frac{1}{2}(110)[1\bar{1}\bar{1}]$$

Split dislocations from different reactions may coalescence into a single dislocation again. Therefore, even though slip system #3 has a relatively high CRSS compared to other systems in Table 1.2, glide on $\{100)$ type planes in $\langle 010]$ direction can still be active due to this type of dislocation reaction.

Slip systems $\{110)\langle 1\bar{1}0]$ (#5), $\{001)\langle 100]$ (#7) and $\{001)\langle 110]$ (#8) were observed only occasionally in Table 1.2, and it is probable that these slip systems are more difficult to be activated. The activation of these slip systems may require higher temperature and/or stress.

In summary, slip systems $\{110)\langle 001]$ (#2), $\{100)\langle 001]$ (#1), and $\{110)\langle 1\bar{1}1]/2$ (#4) are believed to be the most facile in order; slip system $\{010)\langle 101]$ (#6) may be the least active, followed by slip systems $\{101)\langle 10\bar{1}]$ (#9) and $\{100)\langle 010]$ (#3); the relative activity of slip system $\{121)\langle \bar{1}01]$ (#10) may vary with temperature and experimental conditions. Slip systems $\{110)\langle 1\bar{1}0]$ (#5), $\{001)\langle 100]$ (#7), and $\{001)\langle 110]$ (#8) are not as frequently observed as the others. Based their rankings in Table 1.2, they may be less active than slip system #3. Nevertheless, these three slip systems (#5, #7, and #8) were reported to be active in monotonic shear deformation of SAC305 lead-free solder joints [Zhou et al. (2009b)]. However, lack of either CRSS or many observations in the literature indicates that the relative activity of these slip systems are not well understood. Nevertheless, some knowledge of active Sn slip systems is beneficial for the present work. Development of certain grain boundary characteristics and crystal orientations can thus be correlated with dislocation slip activities, which promotes the understanding of the deformation mechanism and the damage development in solder joints.

1.4 Characterization techniques for microstructure and crystal orientations

Knowing the Sn crystal orientation in solder joints is crucial to the understanding of the responses of different crystal orientations to thermal straining. To assess the evolution of Sn crystal orientation during thermal cycling, three main characterization techniques were used in the present study.

1.4.1 Polarized light microscopy

Polarized light microscopy (PLM) is effective in qualitative assessments of the grain structure and crystal orientations. This technique utilizes the birefringent property of non-cubic materials (with more than one refractive index) to reveal contrasts from different crystal orientations under the optical microscopy. For the tetragonal structure Sn, there are two refractive indices n_ε and n_ω. By changing the relative orientation of the near cross-polarized light with respect to the sample (by rotating the sample stage), the variation in the refractive index produces distinguishable contrast [Lee et al. (2009)]. A 90 °rotation of the stage will change the contrast of a crystal from the brightest to extinction (Figure 1.3).

The relatively easy set-up of a polarized light microscopy system enables wide applications for qualitative analyses of Sn crystal orientations. A simple configuration of a polarized light microscope consists of a bright-field optical microscope, a rotating stage, a plane-polarizing filter as “the polarizer” below the sample, and an analyzer filter above the sample [Weaver (2003)]. The use of cross-polarized light microscopy has successfully revealed different grain structures in various studies [Bieler et al. (2008), Seo et al. (2009), Seo et al. (2010), Telang et al. (2004), Elmer et al. (2010), Lehman et al. (2004, 2010), Lee et al. (2009)]. Among these, a six-fold grain structure (also known as Kara’s beachball) in a SAC alloy solder joint was discovered [Lehman et al. (2004)], and the twinning relation between neighboring grains (58 ° and 63 ° misorientation about the Sn [010] direction for the (101) and (301) twins, respectively) was confirmed based on the EBSD analysis in [Telang et al. (2002)]. PLM has also been used to differentiate recrystallized fine grains from the parent orientations [Mattila et al. (2010), Yin et al. (2012), Sundelin et al. (2008), Henderson et al. (2004), Chen et al. (2011), Bieler et al. (2011), and Mattila and Paulasto-Kröckel (2011)].

Although PLM is effective in differentiating different orientation structures in large batches of samples in a time-efficient way, the nature of this technique limits its use for an accurate and quantitative assessment. In some cases, grains with different crystal orientations are not shown in different contrasts using the PLM. As described earlier, the change of the relative sample orientation between the cross-polarized light source and the specimen changes the contrast. A 90 ° rotation switches the view from the maximum brightest to extinction. Figure 1.3 shows an example that clearly illustrates this phenomenon. Note that two pairs of grain boundaries (designated by pairs of red and yellow arrows) in a six-fold microstructure containing three different crystal orientations disappear at the 17 ° and 52 ° rotation of the specimen under the polarized light. In addition, the brightest upper right grain in the first micrograph becomes darkest after a 90 ° rotation. A few other examples listed in [Zhou et al. (2009)] illustrated how a multi-grain structure may be counted as a single crystal or a multi-grain under PLM. Consequently, in order to correctly interpret what is revealed by PLM, different sample orientations need to be assessed through the sample stage rotation.

PLM serves well as a preliminary method to qualitatively identify grain and crystal structures in lead-free solders, and is very efficient in analyzing large number of samples with a small amount of sample preparation effort. However, to obtain accurate crystal orientation information in a quantitative way, electron backscatter diffraction (EBSD) and/or X-ray diffraction (XRD) are required.

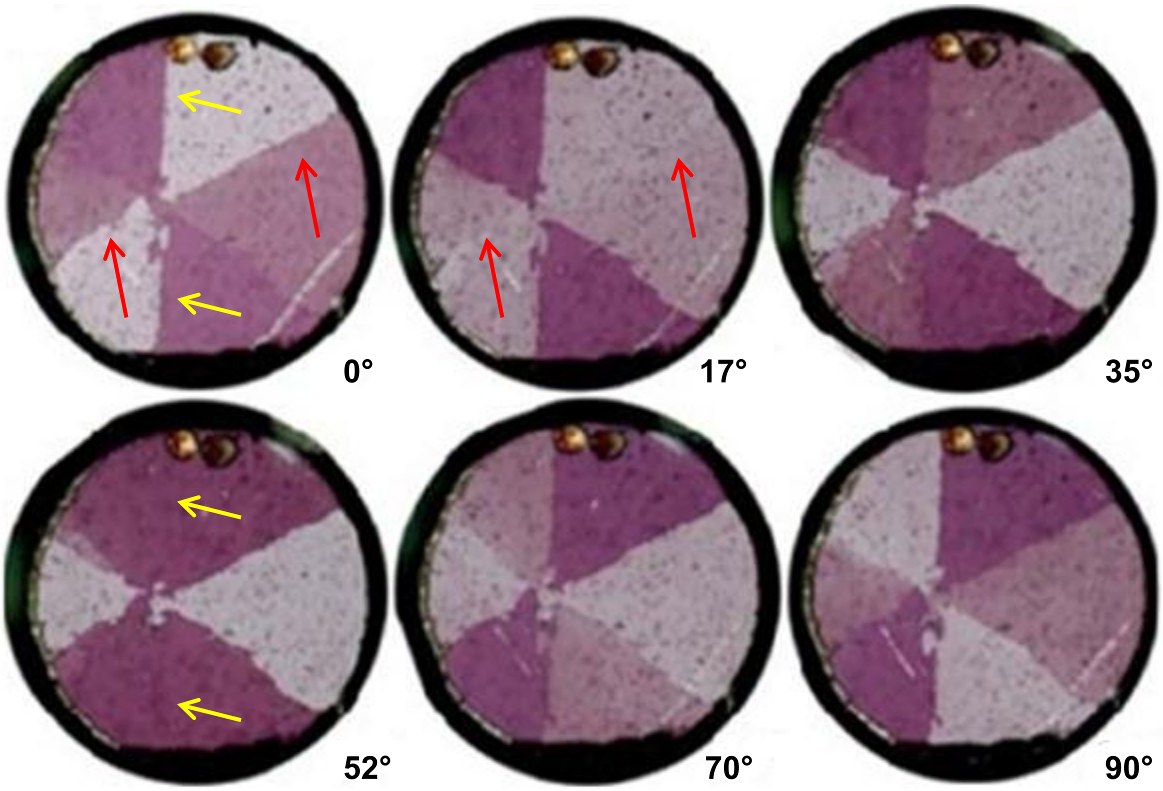

Figure 1.3 Effect of the sample orientation on the viewing contrast of a six-fold twinning structure in a SAC lead-free solder joint under the PLM; two sets of grain boundaries (marked by pairs of red and yellow arrows) disappear at 17 °and 52 °rotation, respectively [adapted from Lee et al. (2009)].

1.4.2 Electron backscatter diffraction

EBSD is an effective means to quantitatively characterize the grain orientation (distribution) across the sample surface using a scanning electron microscope (SEM). This technique utilizes Kikuchi patterns to determine grain orientations in the crystal. Nishikawa and Kikuchi first observed an electron diffraction pattern containing a band feature, and regarded the formation of the pattern as the inelastic and elastic scattering of electrons within the sample [Nishikawa and Kikuchi (1928)]. Later, in a heavily cited paper [Alam et al. (1954)], the same diffraction phenomenon was reported in back reflection. During the 1980s, computer control and algorithms were incorporated to assist the indexing of EBSD patterns [Dingley and Babakishi (1986)]. However, it was not until the 90s that fully automatic pattern recognition and indexation for EBSD was successful in mapping of crystal orientations over a sample surface. This new metallography method was named “Orientation Imaging Microscopy” [Adams et al. (1993)]. An orientation map constructed by collecting the crystal orientation point by point over the sample surface was first obtained by Wright and Adams (1992). Ever since then, EBSD has been further developed to become one of the most important means for obtaining spatially based crystal orientation information.

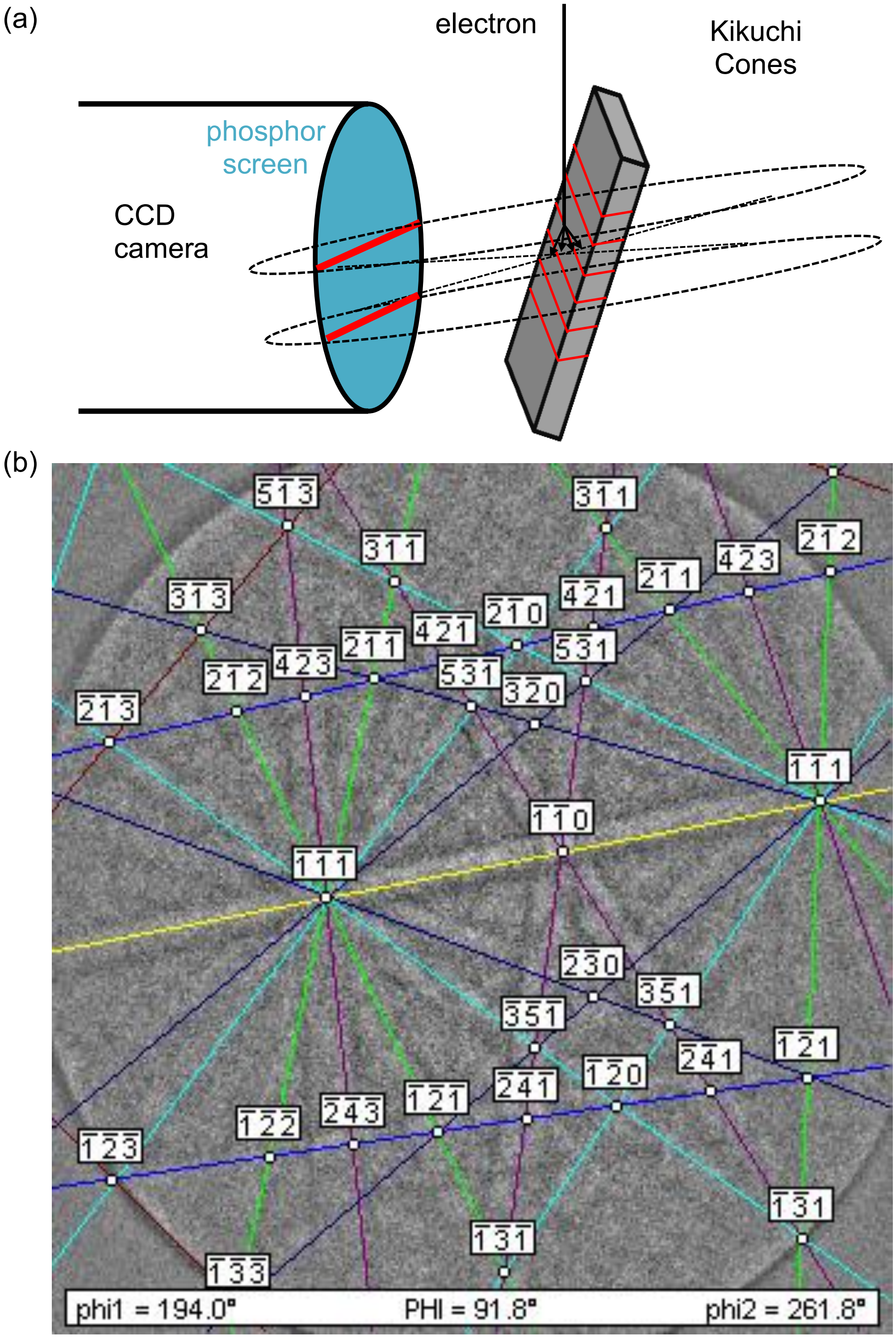

Figure 1.4 (a) Formation of Kikuchi lines from a tilted Sn sample inside a SEM; (b) sets of Kikuchi bands intercept and form a Kikuchi pattern from a SAC305 lead-free solder specimen with background subtraction to enhance contrast, and indexation showing zone axes and the crystal orientation (based on the identified Euler angles phi1, PHI, and phi2).

In order to determine the crystal orientation, a Kikuchi pattern is formed from a tilted sample surface inside a SEM, as shown in Figure 1.4. Electron hits and penetrates the top surface of a sample at a high tilt angle (~70 °). The inelastic scattered electrons can be elastically scattered when the Bragg condition is met for some crystallographic planes (red lines), and sets of Kikuchi cones form. When the cones intersect a detector, pairs of parallel lines are observed, and each pair is named a Kikuchi band. Intersections of bands define zone axes to form a Kikuchi pattern in Figure 1.4(b). The width of the Kikuchi band (prescribed by the diffraction angle θ) corresponds to the d-spacing of a particular crystallographic plane via the Bragg's law. A Kikuchi pattern also includes interzone and interplanar angles, which are correlated with symmetries from different crystal structures. By using a charge couple device (CCD) camera, Kikuchi patterns revealed on the detector are captured for further computer-assisted processing [Wright and Adams (1992)]. After acquiring a Kikuchi pattern, a computer-assisted automatic indexation follows three processing steps: 1) diffraction pattern image processing and band detection, 2) indexing zone axes, and 3) determining crystal orientation based on the interplanar and interzone angles.

The most commonly used algorithm today in EBSD to differentiate bands from the Kikuchi pattern is by the Hough transformation [Krieger Lassen et al. (1992)]. The main idea of the Hough transformation is to represent a Kikuchi pattern in Hough space, where lines in the original pattern are represented by points in Hough space, following equation (1.1).

$$\rho = x\cos\theta + y\sin\theta \tag{1.1}$$

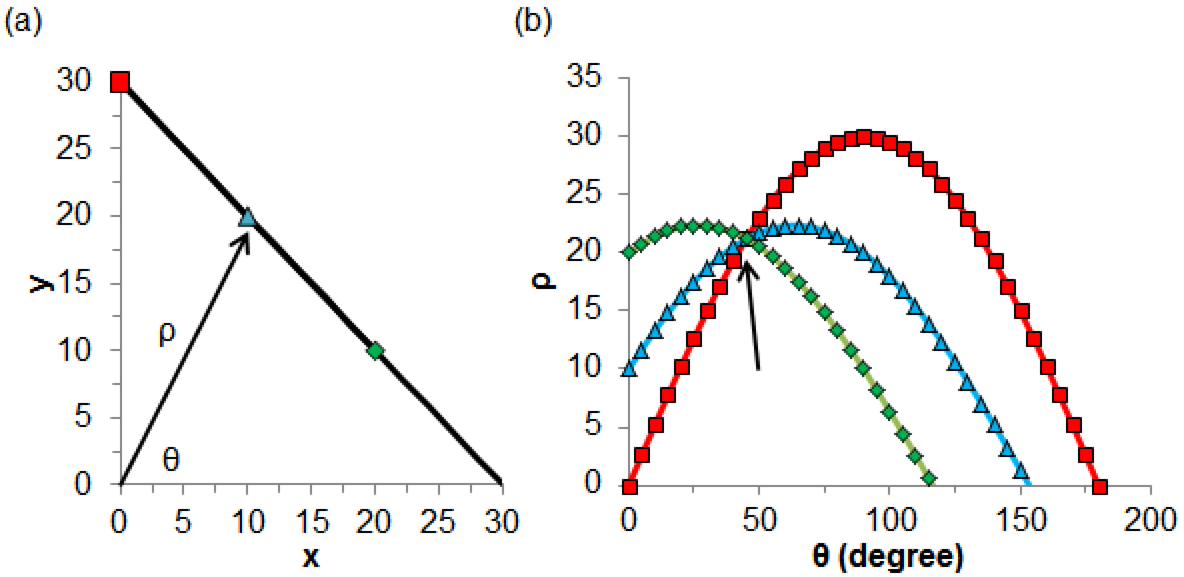

Figure 1.5 Different representations of a line in the pixel space (a) using (*x*, *y*) coordinates, and (b) in Hough space using (ρ, θ); a single point in (b) illustrated by the intersection of multiple curves represents the same line in (a); summation of all curves from the corresponding points in the same line in (a) reflects the intensity of the Hough peak.

In the image space with pixel coordinates, a line can be represented by (x, y) as shown in Figure 1.5 (a), and represented alternatively by the Hough parameters (ρ, θ) in Figure 1.5 (b). For instance, three points on a line in the image space are shown in Figure 1.5 (a). Whereas, in the Hough space (Figure 1.5 (b)), the intersection of multiple curves (which come from points along the same line in the image space) defines a single point, and this point represents the same line in Figure 1.5 (a). By calculating each line (Kikuchi band) using equation (1.1), Kikuchi patterns in the image space are converted into the Hough space. At the same time, the intensity of the pattern at each pixel is also added to the curves in the Hough space, shown as a curvature in the intensity profile at a given point. Consequently, by searching for a peak with the highest intensity in the Hough space, a band can be found.

Once the bands are detected, the band width and the angles between bands (at least three bands are needed) can thus be measured and compared with standard sets of interzone axes angles derived from a known crystal structure and its lattice parameters. All possible combinations of zone axis indices are searched by the computer. The most probable solution is the one that appears most often in the solution sets that match between the measured and theoretical calculated interzone axes angles [Wright and Adams (1992)].

The crystal orientation can be derived once the indices of at least two bands are identified. An orientation matrix relating the sample coordinate system with the crystal lattice frame can thus be calculated when the vectors defining each frame are known [Wright (2000)]. The output of crystal orientation is expressed in three Euler Angles φ_1, Φ, φ_2 (Figure 1.4 (b)). Since the electron beam scans across the sample surface at a chosen step size, the EBSD pattern at each step is captured and indexed, and the corresponding crystal orientation is acquired. An orientation map populated by individual data points is able to reveal grain orientation distribution over a large sample surface. Local orientation gradients and grain boundary characteristics (misorientation angle and rotation axes) can also be obtained.

EBSD has been proven to be an important technique for surface characterization of grain orientations. However, due to the fact that the penetration of electron in the sample is limited, EBSD does not allow a characterization into the bulk material unless serial sectioning or ion milling is performed. In order to preserve the sample, and to be able to assess its crystal orientation non-destructively, X-ray diffraction (XRD) is needed. Another advantage of XRD over EBSD (which requires a damage-free flat surface) is that the sample surface condition does not usually affect the characterization using XRD, and only minimum sample preparation is required. In the following section, only synchrotron X-ray diffraction techniques are addressed.

1.4.3 Synchrotron X-ray diffraction

Unlike a conventional X-ray source, 3rd generation synchrotron X-ray beam has high energy, high flux, and ultra-brightness [Mills (2002)]. In the context of crystallographic study, a synchrotron X-ray source can be integrated into different optics and instrumental configurations, providing capabilities of high energy X-ray diffraction (HEXRD) and three-dimensional X-ray diffraction (3D-XRD).

One approach using the HEXRD technique for a volumetric characterization is the high-energy transmission X-ray diffraction. This technique was first published by Daymond and Withers (1996) and Korsunsky et al. (1998) using a monochromatic beam. A high energy synchrotron X-ray beam has a similar penetration capability as the neutron source, yet the X-ray has a better spatial resolution and a faster measurement due to its higher flux [Daymond and Withers (1996), Korsunsky et al. (1998)]. The diffraction geometry of this HEXRD technique is similar to that of a transmission electron microscopy and the wavelength of the X-ray is considerably small compared to the d-spacings of low-index planes in the sample. Bragg's conditions are met when those planes are nearly parallel to the incident beam [Wanner and Dunand (2001)].

The experimental set-up of this type of HEXRD is relatively simple. The sample is placed on the X-ray diffractometer. The incident X-ray beam penetrates the sample (which can be as thick as several millimeters), and the diffracted beams are collected by a high-resolution area detector or a charge couple device (CCD) camera placed some distance away from the sample. The distance from sample to detector is an important parameter in the strain calculation, and can be adjusted depending on the maximum Bragg's angle of interest, the size of the detector, and the wavelength of the X-ray beam. Fewer diffraction peaks with more pixels for each peak (which is useful for measuring peak shifts) are captured, when the detector is further from the sample. For strain analysis using HEXRD, the distance is typically 0.5 to 1m for a 10-20cm diameter detector [Wanner and Dunand (2001)].

Obtaining crystal orientation information using this experimental configuration was a challenge. For an *in-situ* experiment, the specimen does not have much freedom of rotation in the diffractometer, so that only a small portion of the orientation space is sampled during the experiment. This becomes even more difficult on the study of lead-free solders. Since only a limited number of Sn grains are present in a SAC lead-free solder joint, the diffraction pattern usually contains only a small number of isolated diffraction peaks. Those peaks come from crystallographic planes with normal directions that are nearly perpendicular to the incident beam. The lack of freedom of rotation limits the ability to sample a large orientation space (and to produce more diffraction peaks), and thus makes it difficult to find the correct crystal orientation based on interplanar angles. Moreover, orientation gradients and low-angle grain boundaries are usually present in the solder joint even before thermal straining. Consequently, the full volume of a solder ball often produces streaked diffraction peaks [Bieler et al. (2009b) and Bieler et al. (2012)], which makes it difficult to determine the peak center. Nevertheless, studies have shown that indexation of the diffraction pattern (acquired by HEXRD) was successful using an algorithm which is able to differentiate and index overlapping patterns for transmission electron microscopy [Wu and Zaefferer (2009), Bieler et al. (2009b), and Zhou et al. (2012)].

In addition to the grain orientation, the use of high-energy transmission synchrotron XRD is capable of evaluating the change of elastic strain in the materials. An algorithm reported in the literature is able to analyze the lattice strain (change of d-spacing d from an unstrained reference value d^0 of the same plane) during *in-situ* deformation of a polycrystalline specimen [Wanner and Dunand (2000), Korsunsky et al. (1998)]. In both studies, diffraction ring patterns were captured by a two-dimensional detector (a CCD camera). To extract lattice strain information from a 2-D diffraction pattern, four steps are described as follow. The pattern center is firstly identified by analyzing diffraction peaks in both horizontal and vertical directions across approximately the middle of the diffraction pattern from a powder standard specimen. With a known pattern center, 2) a 2-D pattern can be converted into a radius/azimuth angle (R/φ) profile using polar re-binning of the pixel intensity. During this process, a full circle space is divided into a number of radial lines, and the number of lines depends on the chosen φ step size. This is followed by 3), in which the radius R at each of the angular slices is derived by a Gaussian peak fitting. In order to minimize the influence from the choice of the pattern center on the strain value, instead of using R, 4) the ring diameter $D(\varphi)$ is acquired by Gaussian fitting the peak center positions of diametrically opposite peaks.

The strain is measured by the change of d-spacing d from a reference un-strained value d^0. The relationship between d and D is derived via equations (1.2)-(1.6), in which L is the specimen-to-detector distance, θ is the diffraction angle, and λ is the wavelength of the X-ray [Wanner and Dunand (2000)]. Equation (1.2) is obtained from the trigonometry, and the diffraction angle θ in this equation can be expressed alternatively by λ and d from the Bragg's law in equation (1.3), yielding equation (1.4). For small Bragg angles (when $D/2L<<1$), equation (1.4) can be simplified as equation (1.5). D-spacing d and ring diameter D are related via equation (1.6), which serves as the basis to calculate strain. As described earlier, the diffraction ring diameter value at a given azimuth angle φ (at a particular strain direction) $D(\varphi)$ is calculated by the step 4 above. This value is inserted in equation (1.5) to compute the d-spacing d and the elastic strain on the corresponding lattice plane.

$$\theta = \frac{1}{2}\arctan(\frac{D}{2L}) \qquad (1.2)$$

$$d = \frac{\lambda}{2\ \sin\theta} \qquad (1.3)$$

$$d = \frac{\lambda}{2\ \sin(\frac{1}{2}\arctan(\frac{D}{2L}))} \qquad (1.4)$$

$$d \approx \frac{2\lambda L}{D} \qquad (1.5)$$

$$\varepsilon = \frac{d - d^{0}}{d^{0}} \approx \frac{D^{0} - D}{D} \qquad (1.6)$$

In the case of lead-free solder joints, lattice strain was assessed *in-situ* during thermal cycling using a similar approach [Bieler et al. (2009b), Bieler et al. (2012)]. Due to a limited number of grains with a large grain size (near single crystal or multi-crystal) in the joint, a ring pattern is not generated. Thus, it is not possible to consider the whole ring, and only isolated diffraction peaks in particular directions can be analyzed. The unstrained reference d-spacing d^{0} of a particular plane was calculated from the lattice parameters at a particular temperature $a(T)$ and $c(T)$. Elastic strains on a set of chosen lattice planes (reflecting strains in different directions) were derived using equation (1.6) from the measured d-spacing d and the corresponding calculated un-strained reference value d^{0}.

Instead of characterizing the whole volume of the solder joint using the high energy transmission synchrotron XRD, local crystal orientation gradients and elastic strain distribution can be assessed using synchrotron X-ray micro-diffraction techniques. This non-destructive characterization method has gained popularity on the studies of strain effects on the Sn whisker growth [Choi et al. (2003), Sobiech et al. (2009), Tu et al. (2007)], and electromigration in solder joints [Lee et al. (2007), Chen et al. (2009)]. One configuration of the microbeam X-ray diffraction using ultra-brilliant 3rd generation synchrotron beam is named differential aperture X-ray microscopy (DAXM) which is a form of 3-D X-ray diffraction analysis, as shown in Figure 1.6. In this particular set-up at beamline 34-ID-E at the Advanced Photon Source (APS) at Argonne National Laboratory, a polychromatic X-ray beam is focused to sub-micron scale (0.5μm×0.5μm) by a pair of elliptical non-dispersive Kirkpatrick-Baez (K-B) mirrors [Liu et al. (2005)]. A high energy X-ray beam allows measurements to be made up to hundreds of microns (depending on the absorption) beneath the sample surface. A Pt wire (50μm in diameter) is used as a differential aperture, which traverses along the sample surface driven by stepper motor, blocking a portion of the diffraction beam. At each step, the position of the wire is recorded and the Laue patterns are captured by an area detector.

Both the grain orientation and elastic strain tensor components can be obtained using DAXM via the automatic re-construction, indexation and strain calculation processes. The re-construction algorithm operated on a computer cluster is able to extract Laue patterns that come from each ~1μm^3 diffraction volume element (voxel), and a depth re-solved diffraction pattern from each voxel can thus be acquired. Along the re-construction process, Laue patterns can be automatically indexed when the crystal structure and its lattice parameters are known. The indexation works by first detecting the peak locations, and then computing the angles between diffraction peaks (and thus the angles between crystallographic planes). The angles between different planes are compared with a look-up table generated from a pre-defined initial trial crystal orientation of this crystal structure. Automatic indexation ensures a relatively efficient post data processing method, and orientation maps can thus be plotted in both 2-D and 3-D representations [Ice and Barabash (2007), Larson et al. (2002), Liu et al. (2004), Liu et al.

(2005)]. A Laue pattern from a particular voxel can also be individually indexed using an analysis package developed by Oak Ridge National Laboratory (ORNL) and APS [Sector 34-ID-E].

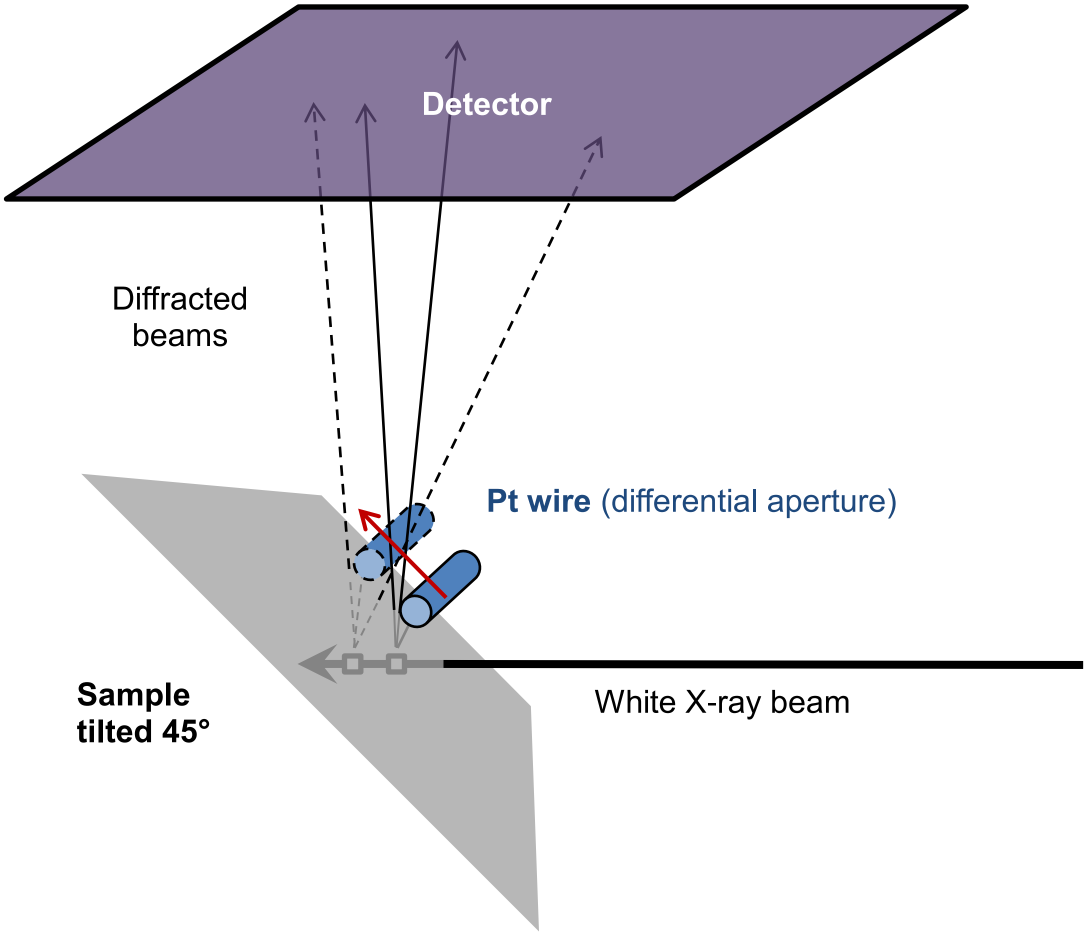

Figure 1.6 A Schematic showing the experiment set-up of DAXM. The Pt wire (as a differential aperture) traverses along the sample surface. Depth-resolved profile is generated from the automatic re-construction and indexation algorithm [Zhou et al. (2012b)].

For each voxel, the strain tensor components can be calculated during the automatic post-processing. This is based on single crystal diffraction, and the local strain tensor is derived via the orientation of the crystal and the distortion of the lattice parameters from the un-strained values [Ice et al. (2005), Ice and Barabash (2007)]. Imagine that Cartesian coordinates (represented by $\boldsymbol{u}_1$, $\boldsymbol{u}_2$ and $\boldsymbol{u}_3$) are attached to the real-space crystal unit cell (represented by lattice parameters $\boldsymbol{a}_1$, $\boldsymbol{a}_2$, $\boldsymbol{a}_3$, $\boldsymbol{\alpha}_1$, $\boldsymbol{\alpha}_2$, and $\boldsymbol{\alpha}_3$). A transformation matrix $\boldsymbol{A}$ is introduced which translates between a position vector $\boldsymbol{v}_\mathrm{u}$ in the Cartesian coordinate system and a vector $\boldsymbol{v}$ in the crystal coordinates, as shown in equation (1.7).

$$v_\mathrm{u} = \boldsymbol{A}v$$

$$\boldsymbol{A} = \begin{pmatrix} a_1 & a_2\cos\alpha_3 & a_3\cos\alpha_2 \\ 0 & a_2\sin\alpha_3 & -a_3\sin\alpha_2\cos\beta_1 \\ 0 & 0 & 1/b_3 \end{pmatrix} \quad (1.7)$$

In equation (1.7), b_3 and β_1 are the reciprocal lattice parameters and angles for the unit cell.

The movement of a vector position in a crystal can be attributed to either a rigid body translation, or the distortion of the crystal lattice due to the presence of strain. The average strain of a measured unit cell can be calculated by comparing the measured unit cell parameters with those from an un-distorted unit cell. Two translation matrices $\boldsymbol{A}_\mathrm{measure}$ and $\boldsymbol{A}_0$ are introduced to convert a position vector $\boldsymbol{v}$ from the measured and unstrained crystal coordinate systems to the Cartesian coordinates, respectively. During this process, the rigid body translation is omitted between the measured and un-strained unit cell when the origin of the unit vectors coincide. A transformation matrix $\boldsymbol{T}$ is introduced to relate $\boldsymbol{A}_\mathrm{measure}$ and $\boldsymbol{A}_0$ via equation (1.8).

$$\boldsymbol{A}_{\text{measure}} = \boldsymbol{TA}_0 \qquad (1.8)$$

Equation (1.8) is related with the strain tensor ε_{ij}, which is represented in the strained Cartesian coordinates as,

$$\varepsilon_{\text{ij}} = (T_{\text{ij}} + T_{\text{ji}}) /2 \qquad (1.9)$$

Both hydrostatic strain and deviatoric strain components are included in equation (1.9), and the strain tensor can be represented alternatively as,

$$\varepsilon_{\text{ij}} = \begin{pmatrix} \varepsilon'_{11} - \mathit{\Delta}/3 & \varepsilon_{12} & \varepsilon_{13} \\ \varepsilon_{21} & \varepsilon'_{22} - \mathit{\Delta}/3 & \varepsilon_{23} \\ \varepsilon_{31} & \varepsilon_{32} & \varepsilon'_{33} - \mathit{\Delta}/3 \end{pmatrix} + \begin{pmatrix} \mathit{\Delta}/3 & 0 & 0 \\ 0 & \mathit{\Delta}/3 & 0 \\ 0 & 0 & \mathit{\Delta}/3 \end{pmatrix} \qquad (1.10)$$

$$\text{where } \mathit{\Delta} = \varepsilon'_{11} + \varepsilon'_{22} + \varepsilon'_{33}$$

Note that the Laue measurement yields precise values of only the off-diagonal deviatoric strain tensor components (shear strain) in equation (1.10). The hydrostatic strain components in the full strain tensor are not determined by this method. Nevertheless, their relative values are related via the parameter Δ, which can be quantified by measuring the energy of at least one reflection in the Laue patterns using a monochromatic X-ray beam [Ice et al. (2005)].

The three characterization techniques described above provide important tools in assessing the microstructural evolution in lead-free solder joints during thermal cycling.

1.5 Recrystallization and microstructural evolution during thermal cycling

As discussed earlier, the primary failure location that causes the electrical failure of an electronic device during thermal cycling is cracking in the bulk solder near the chip-side interface [Park et al. (2007), Matin et al. (2007), Mattila et al. (2010b), Lee et al. (2009), Bieler et al. (2012), Terashima et al. (2003)]. Microstructure and Sn grain orientation evolution preceding crack propagation has been widely reported in the literature [Yin et al. (2012), Shnawah et al. (2012), and Bieler et al. (2008)]. High angle grain boundaries developed during recrystallization facilitate crack propagation [Sundelin et al. (2008), Terashima et al. (2004), Bieler et al. (2008)]. Consequently, in order to understand the failure mechanisms of solder joints during thermal cycling, it is crucial to address the microstructure evolution behavior, which creates a **pre-condition** for solder fractures.

During the plastic deformation in metals, the stored energy (mostly in the form of lattice defects) can be released by the recovery, recrystallization, and grain growth mechanisms. Consequently, in the discussion of microstructural evolution, these processes need to be addressed. During recovery, the material may lower its energy by annihilation and re-arrangements of dislocations through glide, climb, and cross-slip, which may lead to the formation of low-angle (subgrain) boundaries. The recovery process does not usually affect the grain boundaries in the deformed microstructure, and the initial mechanical properties are only partially restored. Further release of energy is achieved by the recrystallization, which requires the movement of high angle grain boundaries. A recrystallized microstructure is thermodynamically unstable due to the presence of grain boundaries. Further energy reduction occurs by the process of grain coarsening which lowers the grain boundary area and energy, to achieve a lower energy boundary configuration [Humphreys and Hatherly (2004), Doherty et al. (1997)].

Depending on the characteristic details, these three phenomena can be categorized into "discontinuous" and "continuous" processes. The former is heterogeneous with distinguishable stages of nucleation and growth, whereas the latter occurs more uniformly and without noticeable nucleation and growth. Specifically, discontinuous processes include "discontinuous subgrain growth", "primary recrystallization", and "abnormal grain growth" (selective growth of a few large grains). Continuous processes, however, consist of "recovery by subgrain growth", "continuous recrystallization", and "normal grain growth" [Humphreys and Hatherly (2004)].

Humphreys and Hatherly (2004) described the stages of recovery process as: 1) formation of dislocation cell in a deformed microstructure; 2) annihilation of dislocation within cells; 3) subgrain formation; and 4) subgrain growth. The reduction of dislocation density occurs during the recovery process. Re-arrangement of dislocations is accomplished by polygonization to form low angle grain boundaries or by subgrain formation. In some cases, dynamic recovery leads to formation of subgrains instead of a cell structure during deformation when the following conditions are met: high stacking fault energy (like Sn), low solute content (Sn-rich solder alloys), large strain and high temperature deformation. In the context of thermomechanical deformation of lead-free solder joints, it is likely that subgrain formation dominates.

In a discontinuous process, the nucleation of recrystallization can be initiated from the recovered microstructure. It is commonly known that recovery and recrystallization are competing processes, and the former may decrease the driving force for the latter significantly, retarding recrystallization [Mattilla et al. (2010b)]. Nevertheless, a recovered microstructure containing subgrains may still be able to further release stored energy by a subgrain coarsening mechanism to reduce the amount of low angle boundaries. In a microstructure with an orientation gradient (which is often the case in lead-free solder joints [Telang and Bieler (2005), Bieler et al. (2012)]), the growth of subgrain during recovery plays an important role in the nucleation of recrystallization [Humphreys and Hatherly (2004)]. In this case, the nucleus for recrystallization may be initiated from the pre-existing subgrains, which is accomplished by subgrain coarsening through boundary migration. In the strain-induced grain boundary migration process, it is required that high angle grain boundaries are present for recrystallization [Humphreys and Hatherly (2004)]. The formation of high angle boundaries by this mechanism can only be achieved with the presence of an orientation gradient. The presence of high angle grain boundaries is a major factor in differentiating the recrystallization process from the discontinuous subgrain growth which involves only low angle boundaries [Humphreys and Hatherly (2004)]. Consequently, primary recrystallization proceeds once it nucleates from the recovered microstructure. .

Recrystallization process can also occur continuously, during which a homogeneous evolution of microstructures is observed. This transformation also involves high angle grain boundaries, which are formed gradually through recovery by 1) subgrain growth (as described earlier), 2) subgrain coalescence [Hornbogen (1979), Doherty et al. (1997), Chen et al. (2011)], and 3) the increase of boundary misorientations through the accumulation of dislocations into subgrain boundaries [Hales et al. (1991)]. During the continuous recrystallization, a deformed texture may sharpen, and stable orientations may be retained, which has similar characteristics as recovery, and may be categorized as an extended recovery process. However, the involvement of high angle grain boundary migration emphasizes its recrystallization characteristics [Doherty et al. (1997), Telang et al. (2007)].

In solder joints, during the recovery processes at the isothermal aging condition, or at the early stage of thermal cycling, more low-angle grain boundaries developed (with misorientation less than 15 °) [Mattila and Kivilahti (2012), Telang et al. (2002)]. As reported by Telang et al. (2002), a number of 5-10 ° low angle boundaries developed by the consumption of small grains with high angle misorientations. The formation of subgrain boundaries during the recovery process was found to be dependent on the active slip systems [Telang et al. (2002), Bieler et al. (2011)]. The knowledge of what slip systems are activated during thermal cycling, as reviewed earlier, provides insight into the evolution mechanisms that follow. In addition to the evolution of grain boundary characteristics, the morphology and distribution of dispersed IMCs in solder joints also changed and coarsening of IMC particles were reported in the literature [Qasaimeh et al. (2011), Bieler et al. (2012)]. Along this, the eutectic network decorating Sn dendrites in the solidified microstructure gradually fades during recovery [Mattila and Kivilahti (2012)].

With further straining, the microstructure evolution in solder joints is dominated by recrystallization. Recrystallization is often observed in the highly stressed regions, for instance, near the interfaces net region [Henderson et al. (2004), Terashima et al. (2004), Yin et al. (2012), Sundelin et al. (2008), Matilla et al. (2010b)], in shear bands [Telang et al. (2002)], and near voids [Sundelin et al. (2008)]. The correlation between the induced thermal strain and recrystallization in solder has been demonstrated in the literature [Henderson et al. (2004), Bieler et al. (2008), Terashima et al. (2004b), Telang et al. (2007), Li et al. (2010)]. The heterogeneous distribution of recrystallized microstructure may be attributed to the different rates of strain energy accumulation, and a more rapid change of microstructure and cracking occurs on the chip-side when the inelastic deformation is more significant [Li et al. (2009), Chen et al. (2011), Sundelin et al. (2008), Terashima et al. (2004)]. In addition to the highly strained corner regions, the recrystallization volume may also expand toward the center of the solder joint as deformation proceeds [Mattila and Kivilahti (2012)].

Continuous recrystallization events have been observed in lead-free solders subjected to mechanical or thermomechanical deformation. Telang et al. (2007) reported continuous recrystallization in single shear lap solder samples with a eutectic Sn-Ag solder alloy on copper substrates during thermal cycling. From EBSD, it was discovered that a minority Sn crystal orientation grew and consumed the initial dominant orientation by gradual lattice rotation. The driving force of this transformation was explained by the maximum strain energy release mechanism. It was calculated using an idealized elastic 3-D finite element model (FEM) that the final resulting orientation by recrystallization has a 20-100% lower elastic strain energy than the initial dominant orientation. Continuous recrystallization was thus accomplished incrementally after each thermal cycle, reducing elastic strain energy.

Continuous recrystallization can also be stimulated when dislocations are absorbed into the subgrain boundaries to form high angle boundaries by increasing misorientations. In this case, gradual lattice rotation develops new crystal orientations that have a large misorientation with the parent grain. This evolution is evident by the change of synchrotron X-ray diffraction patterns during *in-situ* thermal cycling experiment. The same Sn diffraction peaks became more streaked with further straining, and the elastic strain associated with that crystallographic plane increased [Bieler et al. (2009), Bieler et al. (2012)].

In addition to the continuous recrystallization mechanism, evidence of the discontinuous recrystallization was also observed [Bieler et al. (2008), Chen et al. (2011b), Chen et al. (2012)]. The nucleation of the discontinuous recrystallization may be attributed to minority twin orientations with higher dislocation density than their neighboring grains [Bieler et al. (2008)], pre-existing grain/subgrain boundaries [Chen et al. 2012], or IMC particles [Li et al. (2010b)]. The highly misoriented grains developed by the discontinuous recrystallization, due to a greater CTE mismatch, may cause grain boundary sliding and/or decohesion as the grains grow [Henderson et al. (2004), Choi et al. (2000), Sundelin et al. (2008)]. Crack propagated more readily intergranularly along the high angle random boundaries developed by recrystallization [Chen et al. (2012), Chen et al. (2011b), Yin et al. (2012), Sundelin et al. (2008), Terashima et al. (2004)].

The extent of recrystallization is affected by the recovery process. In some cases, recovery may completely suppress recrystallization. As discussed earlier, recovery and recrystallization are competing processes, and the stored energy during deformation can thus be released by recovery, decreasing the driving force for recrystallization. For instance, Miettinen (2005) observed no recrystallization in the near-eutectic SAC solders after extensive deformation and subsequent annealing. Similarly, Korhonen et al. (2007) observed that no recrystallization occurred in the room temperature fatigue deformation. Both studies suggested that recovery may be more effective, and recrystallization can be completely suppressed because of that.

In other cases, recrystallization can still occur when the accumulation of stored energy during the strain-hardening process is not completely released by the recovery process [Mattila et al. (2012)]. The interplay between recovery and recrystallization may contribute to a certain period of incubation time for recrystallization. For instance, Mattila and co-workers [Mattila et al. (2010b)] observed that in the Sn-0.2Ag-0.4Cu lead-free solder joints, during thermal cycling, the incubation time for recrystallization is about 50% of the average cycles-to-failure. In other words, during thermal cycling, recrystallization was not observed in solder joint until about half of its lifetime. In a different study [Yin et al. (2012)], recrystallization in solder joints with a different package design appeared to occur earlier (within 25%-50% of the characteristic life), independent of the distance to neutral point (DNP) and thermal cycling conditions. Since different package design and solder alloys were used in these two studies, it is expected that the effective strain imposed on the solder joints varied, which led to a different rate of recovery and recrystallization.

Intermetallic phases also affect recrystallization. The presence of the Cu_6Sn_5 precipitates (that can serve as nucleation sites for recrystallization) in solder joints with organic surface preservative (OSP) surface finish [Yin et al. (2012)] can reduce the incubation time for recrystallization. In comparison, solders with Ni/Au surface finish have a slower recrystallization speed when subjected to a similar cyclic thermal loading condition [Mattila et al. (2004)]. The amount of Ag content and the morphology of Ag_3Sn IMC particles in the Sn-Ag-Cu alloys also play a role in the rate of microstructure evolution and recrystallization. Sundelin et al. (2008) suggested that SAC alloys with a hypoeutectic composition tend to recrystallize more easily. This result was further confirmed by Terashima et al. (2003), which reported that in the Sn-*x*Ag-0.5Cu (*x*=1, 2, 3, and 4) alloys, lower silver showed a faster failure rate than the higher silver solder joints. The degradation of thermal fatigue life in the low silver content SAC alloys may be attributed to the lack of finely dispersed Ag_3Sn IMC particles to suppress microstructural coarsening. In other words, fine Ag_3Sn IMC particles that are arranged as a eutectic network in the higher silver SAC alloys are effective in pinning Sn grain boundaries migrations during recrystallization, which retards microstructural evolution [Shnawah et al. (2012), Terashima et al. (2009)].

Isothermal aging does not appear to be the driving force for recrystallization in lead-free solder joints, yet it does influence the recrystallization process. It has been reported in the literature that no obvious recrystallization was observed after the isothermal aging alone [Terashima et al. (2004b)]. Moreover, Telang and co-workers [Telang et al. (2004)] discovered that during the isothermal aging process, the distribution of special boundaries in solder joints with similar alloy compositions and cooling rate is similar, and this distribution did not change dramatically with aging. Nevertheless, pre-aging treatment prior to thermal cycling can apparently accelerate recrystallization due to the coarsening of IMC precipitates that accelerates the grain boundary mobility.

1.6 Grain boundary sliding and crack propagation

In solder joints upon thermal cycling, the recrystallized region has distinct microstructural and mechanical features. As stated above, initially the near-eutectic SAC alloy solders have fine Cu_6Sn_5 and Ag_3Sn particles decorating the Sn-rich dendrites [Henderson et al. (2002)]. Upon recrystallization, however, fewer IMC particles was observed (as a result of coalescence), and the coarsening of these particles was apparent in comparison to the non-recrystallized region. The lack of obvious Sn dendrite structures in the recrystallized region was also reported [Chen et al. (2011), Yin et al. (2012), Lee et al. (2011)]. Vickers micro-hardness testing revealed that recrystallized microstructures in lead-free solder joints have lower hardness than the non-recrystallized region, the as-solidified microstructure, and the strain-hardened microstructure [Chen et al. (2011, 2011c)].

During thermal cycling, grain boundary sliding and decohesion occur [Choi et al. (2000), Henderson et al. (2004), Telang et al. (2002)]. The cause of the grain boundary decohesion may be attributed to the absorption of impurities and IMC particles, whereas grain boundary sliding depends on the boundary characteristics during the plastic deformation [Chen et al. (2011), Telang et al. (2004), Bieler et al. (2008), Telang et al. (2002)].

Damage development in solder joints depends both on the Sn grain orientation and the grain boundary characteristics. A strong correlation between the dominant Sn grain orientation and cracking in a BGA package has been reported in the literature [Bieler et al. (2008), Bieler et al. (2012)]. Bieler et al. (2008) demonstrated that in a thermally cycled BGA package with SAC305 solder joints, cracks were only found in solder balls that have the Sn [001] direction (*c*-axis) parallel or nearly parallel to the chip-side interface (noted “red/orange orientation”), but no crack when the Sn [001] direction is perpendicular to the interface (noted “purple/blue orientation") or when multiple Sn grain orientations are present. The corresponding color code of the *c*-axis orientation map is described in detail in Chapter 2.

Grain boundaries with different characteristics developed by recrystallization during thermal cycling can have different effects on the crack propagation. It has been demonstrated in the literature that coincident site lattice (CSL) boundaries in Sn (listed in Table 1.3) are effective in enhancing the endurance of thermal fatigue for solder joints, whereas random high angle boundaries tend to facilitate grain boundary sliding and intergranular cracking [Terashima et al. (2009), Matin et al. (2005)]. According to Terashima et al. (2009), damage was found in random high angle boundaries that developed during recrystallization, while the neighboring high angle CSL boundaries were more stable and remained intact during deformation. Statistics in the same work indicated that the samples with more stable special boundaries exhibited better thermal fatigue lives. Moreover, Watanabe and co-workers demonstrated in a few studies that under high temperature deformation conditions, a random boundary can be considered as a potential crack due to its high energy, which is preferentially vulnerable to intergranular crack propagation [Watanabe (1993), Watanabe et al. (2005)]. This may help explain the above observations.

Table 1.3 Commonly observed CSL boundaries in Sn [Telang and Bieler (2005)]

Low angle		**High angle**					
7.3 °@ [110]	14.3 °@ [100]	22.3 °@ [110]	28 °@ [001]	43 °@ [100]	58 °@ [100]	63 °@ [100]	71 °@ [100]
Σ 30	Σ 16	Σ 27	Σ 17	Σ 21	twin	twin	Σ 21

Grain boundary sliding on a low angle boundary was also observed during thermal cycling, which is likely to be correlated with dislocation climb [Telang et al. (2006)]. The slid boundary has a ⟨110] type of rotation axis lying in the boundary plane, suggesting that this could be a low angle tilt boundary. Given that the Burgers vector is normal to the boundary plane, in order to introduce displacement parallel to the boundary (which is the movement causing grain boundary sliding), dislocation climb is required. Due to the high homologous temperature for thermomechanical deformation in solder joints, the observed sliding in the low angle boundary (with a near CSL misorientation) was attributed to the climb of misfit dislocations in the boundary plane [Telang et al. (2006)]. An important factor that may have contributed to the **development** of this boundary with the ⟨110] rotation axes is dislocation slip on facile slip systems, as will be discussed later in this dissertation.

As described earlier, crack initiation and propagation were often observed to occur at the high-angle recrystallized grain boundaries. The rate of crack initiation and propagation is greatly influenced by the rate of recrystallization [Mattila and Kivilahti (2012)]. The thermal cycling process can be considered as a combination of the creep and fatigue deformation. Due to the high homologous temperature during creep, the role of the grain boundary is crucial when considering the boundary damage. The fine grain developed by recrystallization may facilitate grain boundary sliding and vacancy diffusion, which may lead to void formations and cracking. In the context of fatigue, cracking involves plastic deformation to alternately sharpen and blunt the crack tip during cyclic straining, often revealed as a fatigue striation in the fracture surface [Chen et al. (2011b)]. Mattila et al. (2010b) examined the nucleation rate of cracks in the BGA solder joints during thermal cycling, and concluded that the nucleation of cracks occurred within a relatively narrow range. Crack initiation during deformation depends only on the number of thermal cycles, yet independent of thermal cycling conditions and microstructural evolution [Mattila and Kivilahti (2012)].

In some cases, initiation of cracks may occur before an apparent recrystallization was observed [Chen et al. (2011)]. However, without the assistance from recrystallization, crack growth was impeded [Shnawah et al. (2012), Chen et al. (2011), Mattila et al. (2012)]. One example is that in the fractured solder joints with no apparent recrystallization, only partial cracks were observed, and no crack had propagated entirely through the joint. Chen et al. (2011) observed recrystallization in all failed solder joints, suggesting a strong correlation between the recrystallization and cracking. It was also reported that cracks did not propagate further than the recrystallized region.

Cracks can also propagate transgranularly when the conditions (stress state, crystal orientation, and geometry of the grain) are not favored for intergranular cracking [Mattila and Kivilahti (2012)]. In some cases, both transgranular and intergranular fractures were observed at the same time [Terashima et al. (2003, 2004b)]. Nevertheless, recrystallized grain boundaries evidently provide favorable energy paths for cracks to propagate intergranularly.

1.7 Summary of the literature review

In Sn-rich lead-free solders, Sn anisotropy plays an important role in the responses of solders to the thermomechanical loading. Upon thermal cycling, the cyclic change of temperature introduces thermal strains due to the CTE mismatches, both extrinsically between different components in the electronic package, and intrinsically between different Sn crystal orientations.

During thermal cycling, the dominant failure mode in solder joints is cracking and microstructure evolution that precedes crack propagation is widely reported. Cracks are often found in the bulk Sn near the chip-side interface where the CTE induced thermal strain is higher. Both continuous and discontinuous recrystallization processes are responsible for the development of vulnerable high angle grain boundaries. These boundaries have a high energy configuration and are more susceptible to intergranular crack propagation. Transgranular cracks occur occasionally when stress, crystal orientation and other factors are not favored for intergranular cracking.

The plastic response of a solder joint to thermal straining depends on the deformation behavior of Sn grains. Active Sn slip systems are reviewed in the literature, and it is found that slip in the Sn [001] (*c*-axis) direction on $\{100\rangle$ and $\{110\rangle$ planes (slip systems #1 and #2) are the easiest. Slip system $\{110\rangle\ \langle 1\bar{1}1]/2$ (#4) is also facile. In contrast, slip in the $\langle 101]$ and $\langle 010]$ directions are usually not as facile. Development of certain grain boundary misorientations are directly correlated with slip activity, and the characteristic details of grain boundaries define their relative resistance to boundary damage and crack propagation.

In the literature, recrystallization and microstructure evolution in lead-free solders during thermal cycling are often studied phenomenologically, and there is lack of information regarding the contribution of dislocation slip, particularly in solder joints in commercial packages. Moreover, the effect of strain on microstructure evolution due to different package designs is not well understood. Statistical analysis of Sn grain orientations and their evolutions in a large number of samples are not well documented prior to this work. Continuous characterization of the same solder ball throughout its thermal history using non-destructive method is also not reported prior to this work.

The scope of this study is to characterize the Sn crystal orientation evolution, and to identify its role in the development of vulnerable microstructures for crack development using both conventional and non-destructive methods. Importantly, a correlation between the Sn slip systems (and dislocation activities), and sub-grain formation and recrystallization are discussed. Different electronic package designs are used to explore the role of relative strain levels on different recrystallization behaviors during thermal cycling. For selected solder joints in three package designs, microstructural and Sn grain orientation evolution phenomena are examined in detail. The effects of Sn crystal orientation and grain boundary characteristics on the failure mechanisms of solder joints during thermal cycling are addressed in this dissertation.

Chapter 2

Experimental and characterization methods

2.1 Samples and sample preparation

Commercial lead-free solder joint samples from three different electronic package designs were provided and prepared by Cisco Systems, Inc. (Figure 2.1), and only one solder alloy Sn-3.0Ag-0.5Cu (wt %) was used. Similar reflow profiles (peak temperature of 240 ℃ and 60 seconds above the liquidus) were used to fabricate all packages.

The first package that was analyzed is the **low-strain** plastic ball grid array (PBGA), which contains a full array of 14×14 solder joints. This design has fairly large package size (15×15 mm), ball size (600 μm in diameter), and ball pitch size (1mm). The silicon die (5 mm×5 mm) is attached to a 2.4 mm thick high glass transition temperature T_g FR4 print wiring board (PWB) through the solder joints. Different surface finishes were applied to the solder ball. The chip-side has an electrolytic Ni/Au surface finish, whereas the board side has an organic surface preservative (OSP) Cu surface finish.

Medium-strain fine-pitch ball grid array (BGA) has a 13×13 mm package body size with two different Si die sizes: 10.05mm large die (as shown in Figure 2.1) and 5mm small die (in Figure 4.4). The solder ball diameter (300μm) and ball pitch (0.4 mm) is the same for both Si die configurations, and are much smaller than the PBGA design. Both the chip-side and board-side have an OSP Cu surface finish. A 2.4 mm thick 370HR PWB was used in this package design.

In the **high-strain** wafer-level-chip-scale package (WLCSP) design, the size of the silicon die (7×6mm) is the package body size. The solder balls (10×10 array with 98 I/Os) used to connect the Si die to a 2.4mm thick FR4 PWB are 250μm in diameter with 0.5mm ball pitch size. The chip-side of the solder joint has a Ni/Au surface finish and the board side has an OSP Cu surface finish.

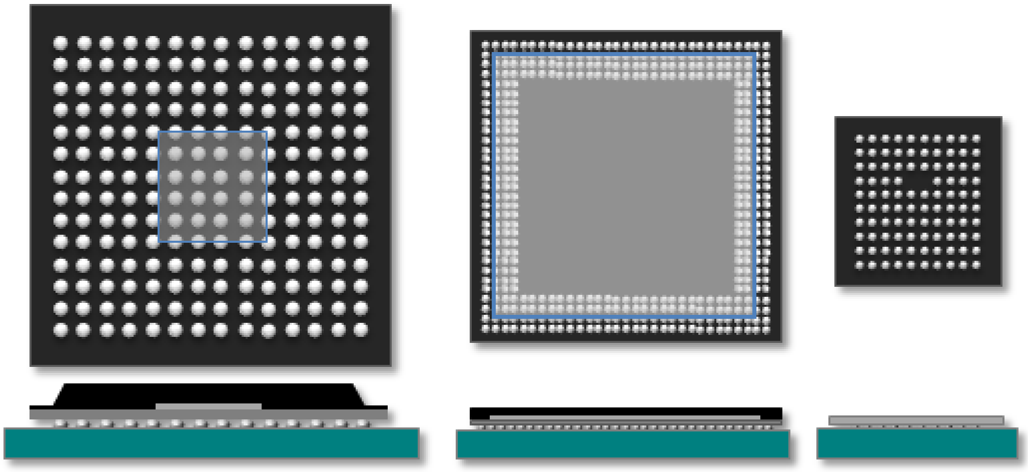

Figure 2.1 Schematic showing the plan-view and the cross-section of three package designs from left to right: PBGA, fine-pitch BGA (large-die), and WLCSP; embedded Si chip is shown both in the plan-view (as a grey shaded box) and in the cross-section.

Lead-free solder samples were prepared following the standard metallurgical procedure. An array of solder joints were cold-mounted in epoxy and cut for plan-view or cross-section assessments. The mounted sample was ground and polished from the PWB side to the solder joint for the plan-view assessment, until about 50% of the height of solder ball was removed. A different approach was to cut a row of solder balls from the solder array to examine the joints in cross-section. A set of samples from the WLCSP design were pre-cross sectioned without the epoxy mount, and the same solder joint was assessed at the different stage of deformation. In both methods, a final polish with colloidal silica suspension (with particle size ~0.06μm) was done to ensure a flat and damage-free sample surface for the EBSD characterization. Etching was not needed as the electrochemical reaction between the colloidal silica suspension and the sample is able to make a smooth surface. In some cases, in order to remove the oxide from a previously polished surface that had been exposed to air for several months to regain a good surface, a light etching was applied. The etchant solution containing 5% HNO_3 (vol. %) in C_2H_5OH or CH_3OH was applied to the sample surface for a few seconds with a cotton applicator. The sample was then rinsed with water and alcohols to remove the residual etchant.

Two thermal cycling profiles were used in this work. For most of the experiments, the accelerated thermal cycling schedule was 0 ℃ -100 ℃ with 10min dwell time at both extreme temperatures and 10min ramp time, yielding a 40 min cycle. A different profile used solely for the *in-situ* thermal cycling at the synchrotron beamline has a longer dwell time (18min and 19min at the high and low temperature extremes) and a decelerating ramp-rate, and one full cycle of this profile was about 67 min.

2.2 EBSD assessments

Two methods were used to reduce the charging effects inside the scanning electron microscope (SEM) from the non-conductive epoxy mount of the solder specimens. In most of the cases, the sample was covered mostly by the Cu cape, and the areas surrounding the solder balls were carefully covered with the conductive carbon paint. In other cases, when painting was challenging due to a small ball pitch size, a 0.2-0.3nm gold coating was applied to the sample surface using a Leica EM MED020 high vacuum coating system. A relatively thin layer of gold is effective in reducing charging without losing too much of the EBSD pattern intensity from the sample itself.

Two SEMs equipped with EBSD analysis systems were used. Most of the microscopy work in this study was done using a CamScan FE field emission SEM (Cambridge, UK) in the department of Chemical Engineering and Materials Science, Michigan State University. This microscope has both secondary and backscatter electron imaging capabilities with a digital resolution of 640×480 pixel size in its output images. The accelerating voltage was set to be 20kV or 25kV, and the working distance was 33mm for EBSD. Automatic EBSD pattern acquisition and indexation was achieved using the TSL EDAX system (OIM Data Collection version 4.5) with a DigiView EBSD detector. A 2×2 binning setting enabled an acquisition speed of about 15-20 points per second. More recent work was accomplished on a Tescan Mira 3 field emission SEM in the Composite Materials & Structures Center, Michigan State University. With the latest TSL EDAX system, an average speed of 30 points per second was achieved by a faster camera and a newer acquisition software (OIM Data Collection version 6.1.3).

To enhance the contrast of the EBSD Kikuchi pattern, a background subtraction was applied to the pattern using the acquisition software. This is normally done using the average pattern intensity from a polycrystalline sample containing various crystal orientations. However, due to the limited number of Sn grains in lead-free solder joints, a Kikuchi pattern from a near-single crystalline area does not serve well as a background. Instead, the background intensity was collected from a small area on the Cu tape (which is polycrystalline) under the similar magnification. The background image was then further processed using a smooth filter when the "dynamic background subtraction" was selected during the scan, and better image contrast was obtained after subtracting the background image from the original pattern.

The scanning step size and the sample orientation (with respect to the beam) vary with the solder ball size and the analytical needs. For a coarse scan to obtain the overall Sn crystal orientation on the whole joint surface, a step size of 3-10μm was often used. For a detailed study of local orientation gradients and grain boundary distributions, typically near the chip-side interface, a 0.25-1μm step size was used. In this case, to reduce the shadowing effects from a high angle tilt condition required by the EBSD, the sample was rotated 90 °, so that the interfacial area was aligned with the vertical direction (normal to the tilt axis). Scanning in this region was thus not affected by the tilt angle. Only the β-Sn phase was scanned, and the IMC particles were often neglected due to their small size, which requires a larger magnification and a smaller step size for pattern detection and indexation.

During the post-processing of the EBSD raw data using the EDAX OIM Data Analysis software (version 5.1), a user-defined orientation map "*c*-axis orientation map" (that is not pre-included in the embedded map template) was introduced in this study. The *c*-axis orientation map illustrates the Sn crystal orientations by highlighting the orientation of the Sn [001] direction (*c*-axis) with respect to solder/chip interface. To plot a *c*-axis orientation map, one first plots the [001] direction in a "crystal direction" map. Then, instead of using the default setting of the tolerance angle and color scheme, "90°" and 5-color code (purple-blue-green-yellow-red) are used for this particular type of orientation map. These settings enable the user to plot the crystal orientation using a different color code than the inverse pole figure color triangle. When the Sn [001] direction (*c*-axis) is aligned with the solder/chip interface plane, the orientation is shown as "red"; when *c*-axis is normal to the solder/chip interface, the orientation is "purple". Other colors will fill in the rest of the orientation space. Therefore, the "red" and "purple" orientations will be referred hereafter as two extreme cases in the *c*-axis orientation map, as defined here.

In addition, *z*-axis (the direction normal to the chip/solder/board interface) average CTE maps were also computed in the present work to illustrate the effect of the CTE anisotropy in Sn in a statistical sense. This type of map was generated from a plan-view representation of a solder joint array. For many packages with different designs and thermal histories, every solder joint was examined individually by EBSD. The average CTE value normal to the sample surface (*z*-axis) is calculated by knowing the Sn grain orientation and the area fraction of each "grain" in the scanned area. For a particular Sn crystal orientation, the equivalent CTE value normal to the scanned sample surface is computed from the CTE values of the three principle directions. Contribution from different crystal orientations within a multi-grain structure is weighted by their area fraction. A *z*-axis average CTE map was drawn as an array of pixels corresponding to each solder joint. The minimum and maximum values of CTE in Sn are 15.4×10^{-6}/ ℃ and 30.5×10^{-6}/ ℃, and are correlated with the red and purple colors, respectively. More specifically, in this continuous 5-color spectrum, "red" covers the CTE values within the range 15.4-

18.42×10^{-6}/ ℃; "yellow" for $18.42\text{-}21.4\times10^{-6}$/ ℃; "green" for $21.44\text{-}24.4\times10^{-6}$/ ℃; "blue" for $24.46\text{-}27.4\times10^{-6}$/ ℃; and "purple" for $27.48\text{-}30.5\times10^{-6}$/ ℃. This setting enables labeling a crystal orientation as "red" when the Sn [001] direction (*c*-axis) is nearly lying on the solder/chip interface plane; and "purple" when *c*-axis is nearly perpendicular to the interface plane. This choice of color code is similar to the representations in the *c*-axis orientation map, and can be easily related one to the other, but the relationship is not linear.

An important step in the post-processing is "clean-up", which removes erroneous or minority data points coming from the un-indexed or wrongly indexed patterns. Two clean-up algorithms were used in this study: "Grain dilation" and "Neighbor CI Correlation". "Grain dilation" is iterative methods which finds a point that does not have the same orientation of any surrounding pixel, and assign to it the neighboring grain orientation that most of the surrounding pixels belong to. This clean-up method requires a user input parameter "Minimum Grain Size" (in terms of pixels) to select the size of features to be re-assigned. Depending on the step size and the knowledge of the minimum Sn grain size, the cleanup parameter can be properly chosen, usually ranges between 2 to 5. This process can be done more than one round, but in the present study, only one round was used to prevent an excessive "data creation". The other method that was often used in this study is "Neighbor CI Correlation". This works by replacing a datum point having a low confidence index (lower than a user defined value, usually between 0.05-0.1) with the neighboring point that has the highest confidence index, and the crystal orientation is re-assigned at the same time.

Highlights were used for a better visualization of the EBSD results. For instance, the Sn unit cells were overlaid on the EBSD orientation maps to show the crystal orientations. In some cases, grain boundaries are highlighted using different colors for different ranges of misorientation angles. The results from the misorientation angle distribution and local average misorientation histograms were exported as plain text, re-plotted, and further analyzed in the Excel Spreadsheets. Pole figures were plotted using different colors and overlaid for a direct comparison of different peaks.

2.3 Synchrotron X-ray diffraction assessments

In-situ characterization of the Sn crystal orientation and strain evolution using a high energy monochromatic X-ray beam was accomplished at beamline 6-ID-D at the Advanced Photon Source (APS) at Argonne National Laboratory. The experimental set-up for the *in-situ* assessment of thermal cycling is shown in Figure 2.2. The sample used for this test is a full WLCSP package with an array of lead-free solder balls attached to a silicon chip and the PWB. The slits were set to be the same or slightly larger than the joint size, and only the corner joints in each package were examined. To avoid diffraction peaks from the neighboring balls, the surrounding solder joints were removed prior to fabrication. The sample was placed with the Si chip side down on a piece of copper block containing a cartridge heater capable of heating up the sample at rates similar to industrial practice. A thin layer of thermal grease was applied on the contacting surface between the Si chip and the copper to ensure good heat conduction. The copper block was fixed on a Peltier stage equipped with a cooling fan.   A thermocouple was placed between the heater and the copper beneath the sample, and the readout temperature was used as a feedback control for the heating and cooling profiles. A similar configuration was adopted for the *in-situ* reflow experiment, where the Peltier stage was replaced with a similarly shaped stainless steel [Zhou et al. (2012)]. By using both set-ups subsequently, the full history of a solder joint was monitored from the reflow to the subsequent thermal cycling in a complete WLCSP package (with silicon chip, solder joint, and PWB).

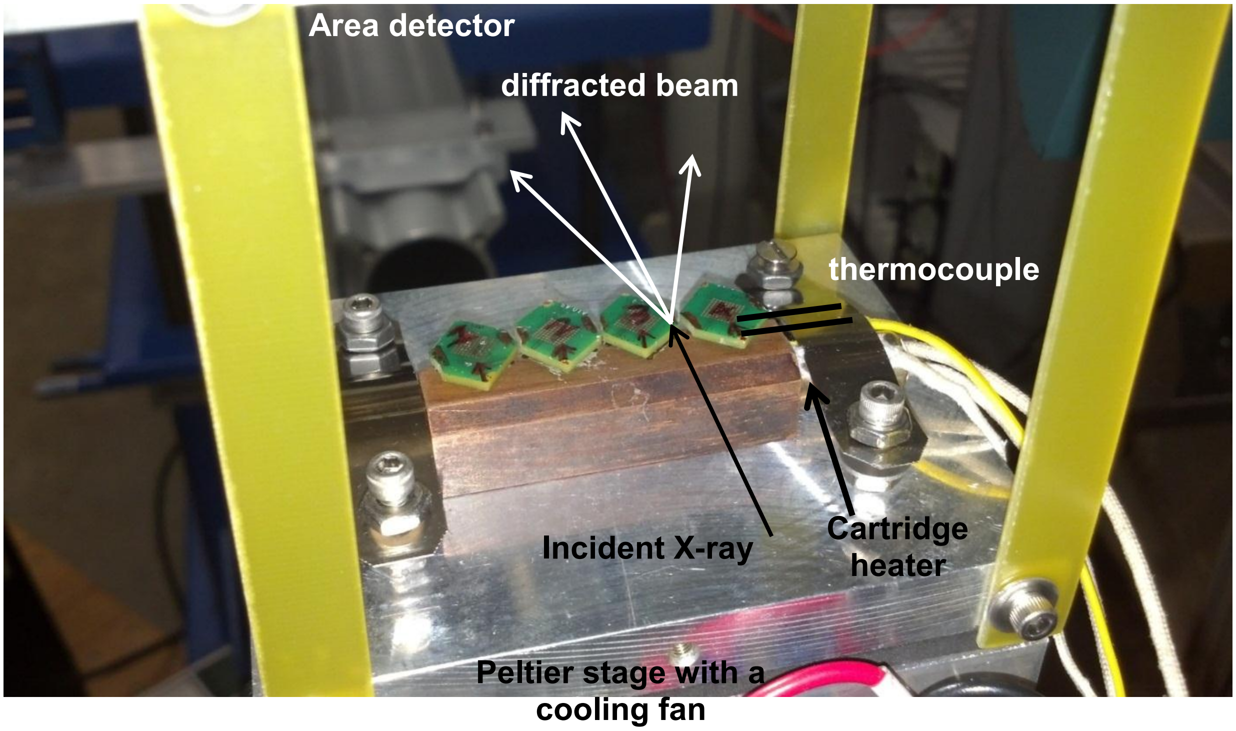

Figure 2.2 Experimental set-up at synchrotron beamline 6-ID-D for *in-situ* characterization of thermal cycling; SAC 305 solder balls in a full WLCSP package was heated using a cartridge heater embedded in a copper block; temperature was read by a thermocouple; only the corner balls in each specimen were examined, and the diffraction patterns were collected by an area detector.

Post-processing of the raw data collected in the experiment was accomplished using free software Fit2D. As described earlier, the diffraction patterns were recorded by an area detector, and the 2-D diffraction patterns need to be converted into a 1-D two-theta (or d-spacing) vs intensity plot for the strain analysis. Translation of the raw data requires the precise values of the wavelength of the X-ray, the beam center position, and the sample-to-detector distance. The high-energy monochromatic X-ray beam has an intensity of about 100keV (and a wavelength of approximately 0.12Å). The precise value of the wavelength can be acquired onsite by typing the command "getE" in the command line at the station control computer. The beam center position and the sample-to-detector distance were determined by a calibration process described next.

The calibration process requires a 2-D diffraction ring pattern from an un-strained standard material, from which the precise beam center position and the sample-to-detector distance can be obtained. A NIST 640c Si powder sample was used as a standard reference material, which was placed at the same location as the specimen on the stage. The diffraction ring pattern from this material was captured using the same experimental set-up. In order to acquire a smooth ring pattern, the sample was rotated during a 5s exposure time, and the summation of several frames from different diffraction volumes effectively reduced the grainy features in the ring pattern. A background frame was also captured without the incident beam. Calibration in Fit2D requires manually inputting the wavelength (precise value obtained from the "getE" command), an estimated sample-to-detector distance (1m), and the size of horizontal and vertical pixels (200μm). Next, the "refine X/Y beam center" was checked and "refine wavelength" was not selected. Then, the location of the innermost Si ring was accurately marked by manually selecting 6-10 points on the ring. The software then automatically marked the rest of the rings and output the calibration parameters.

With the beam center and the sample-to-detector distance known, a complete 2-D diffraction pattern from the solder sample can be converted into a typical 1-D two theta (or d-spacing) vs intensity plot using the “Integrate” function in the Fit2D. Alternatively, instead of full-circle integration, a single 2-D diffraction pattern can be sliced around the azimuth angle using the “Cake” function in Fit2D and a macro “Fit2d2maud”, and the algorithm was described in Chapter 1. For any chosen 5 °azimuth angle range, the two-theta vs intensity plot can be generated, and the evolution of the lattice strain on the corresponding diffraction planes was studied by analyzing the peak shifts from the un-strained d-spacing (derived from two-theta). A detailed procedure can be found in the instruction manual prepared by S. Merkel [Fit2d2maud].

Synchrotron X-ray microdiffraction experiments were conducted at the beamline 34-ID-E at APS. The experimental set-up is illustrated in Figure 1.6 in Chapter 1, and the data processing procedure is described in the same section. In contrast to the high-energy X-ray application, a white beam was used in the microdiffraction experiment with a beam size of approximately 0.5μm×0.5μm. The scanning step-size was set to be 1μm or 2μm in a surface line-scan (in the horizontal X direction). For each step along the line, about a hundred microns in depth in the incident beam direction was sampled. One solder joint in a medium-strain fine-pitch BGA package was pre-aged at 100 ℃ for 500 hours prior to thermal cycling to failure. The sample was mounted in epoxy, cross-sectioned, polished, and stored for about a year in the ambient temperature before it was re-examined using a fine step EBSD scan about a week before the synchrotron X-ray assessments. The use of EBSD provided a way to identify an interesting place for the 3-D XRD analysis. The thermal history and experimental conditions associated with the sample in this dissertation will be further described in the results and discussion.

2.4 Slip-trace analysis and Schmid factor calculation

In order to correlate the microstructure evolution with slip activities, slip trace analysis was performed and Schmid factors were calculated for different slip systems. Slip trace analysis is based on known crystal orientations.

In EBSD, the crystal orientation is expressed in terms of three (Bunge) Euler Angles φ_1, Φ, and φ_2. The orientation matrix (or rotation matrix) $\boldsymbol{R}$ which relates the crystal coordinate system to the global lab coordinate system is constructed from these three values, as shown in equation (2.1).

$$\boldsymbol{R} = \boldsymbol{R}_{\varphi 1}\, \boldsymbol{R}_{\Phi}\, \boldsymbol{R}_{\varphi 2} = \begin{bmatrix} \cos\varphi_1 & -\sin\varphi_1 & 0 \\ \sin\varphi_1 & \cos\varphi_1 & 0 \\ 0 & 0 & 1 \end{bmatrix} \begin{bmatrix} 1 & 0 & 0 \\ 0 & \cos\Phi & -\sin\Phi \\ 0 & \sin\Phi & \cos\Phi \end{bmatrix} \begin{bmatrix} \cos\varphi_2 & -\sin\varphi_2 & 0 \\ \sin\varphi_2 & \cos\varphi_2 & 0 \\ 0 & 0 & 1 \end{bmatrix} \quad (2.1)$$

The representation of each slip system in the slip trace analysis and the Schmid factor calculation is as follows. The slip direction and slip plane normal of a given slip system (*h k l*) [*u v w*] are expressed by Miller indices, and can be further represented by two column vectors $\boldsymbol{n}$ (plane normal) and $\boldsymbol{b}$ (slip direction). These two vectors are converted into orthogonal coordinate system and normalized as $\hat{\boldsymbol{n}} = \frac{\boldsymbol{n}}{|\boldsymbol{n}|}$ and $\hat{\boldsymbol{b}} = \frac{\boldsymbol{b}}{|\boldsymbol{b}|}$. Up until this step, the plane normal direction is still expressed in the crystal coordinate system. For the slip trace analysis, slip plane normal needs to be represented in the global lab coordinate system as $\boldsymbol{n}'$ via the rotation matrix $\boldsymbol{R}$.

$$\boldsymbol{n}' = \boldsymbol{R} \cdot \hat{\boldsymbol{n}} \qquad (2.2)$$

The vector for the slip trace associated with this given slip system $\boldsymbol{n}''$ is calculated by equation (2.3), which is the cross product of $\boldsymbol{n}'$ and the sample surface normal direction ([0 0 1]) in the global lab coordinate system**.** Then, a comparison is made between the calculated plane traces and the slip traces revealed on the optical or SEM micrographs.

$$\boldsymbol{n}'' = \boldsymbol{n}' \times \begin{bmatrix} 0 \\ 0 \\ 1 \end{bmatrix} \qquad (2.3)$$

To calculate the Schmid factor associated with each Sn slip system, a stress tensor $\boldsymbol{\sigma}$ needs to be obtained first. As discussed earlier in this dissertation, during thermal cycling, shear stress due to CTE mismatches is often the dominant effect. The varying locations of different solder joints in an array lead to different directions and values of the distance to the neutral point (DNP). The sense of shear parallel to the solder/chip interface can be represented by a vector pointing from the solder ball to the geometric center of the package, and the magnitude of this vector is equivalent to DNP. Consequently, each solder ball has a unique expression of the CTE imposed stress tensor, named as $\boldsymbol{\sigma}'$. For a solder joint on the cross-sectioned view of the outer row, the sample surface normal is defined as the "*3*" direction, and the "*1*" and "*2*" directions are on the examined surface parallel and normal to the solder/chip interface, respectively. By applying this definition, shear stress components *12* and *21* have non-zero values, as in equation (2.4). This stress tensor is also illustrated in Figure 2.3(a).

$$\boldsymbol{\sigma} = \begin{bmatrix} 0 & 1 & 0 \\ 1 & 0 & 0 \\ 0 & 0 & 0 \end{bmatrix} \qquad (2.4)$$

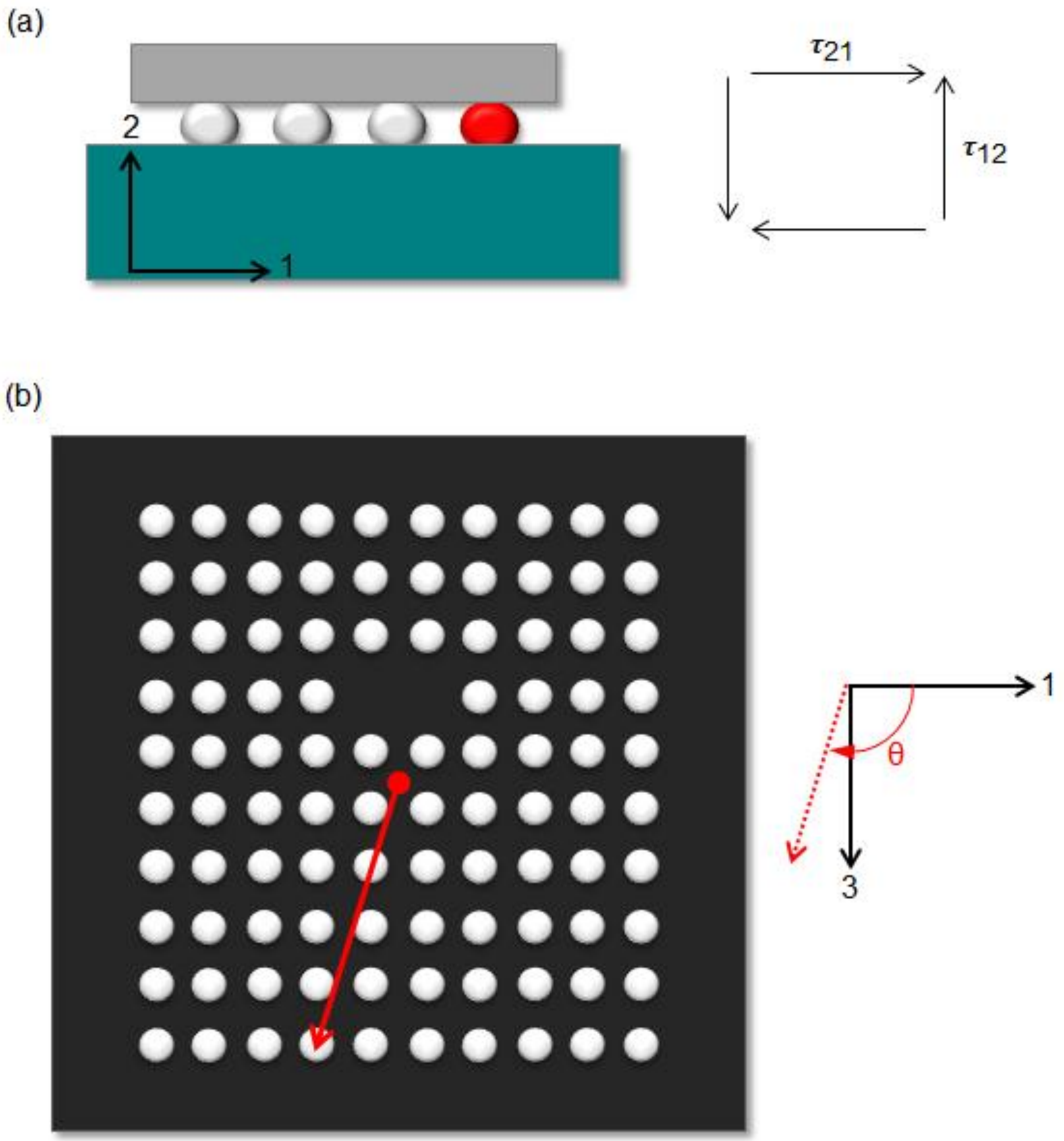

Figure 2.3 Schematic drawing showing an addition rotation of shear stress tensor about the global “2” direction for a particular solder ball; (a) a cross-section view of the sample, e.g. an isolated single row of joints with one ball highlighted in red, and the representation of shear stress in the global coordinate system (b) a plan-view illustrating the sense of rotation to line up shear component to the direction marked by the red arrow.

For each solder joint on the cross-sectioned view of the outer row, one additional rotation about the global "*2*" direction is needed. The stress tensors $\boldsymbol{\sigma}$ and $\boldsymbol{\sigma'}$ for any solder ball are related via equation (2.5) where the rotation matrix $\boldsymbol{g}$ contains the one additional rotation.

$$\boldsymbol{\sigma'} = \boldsymbol{g}\,\boldsymbol{\sigma}\,\boldsymbol{g^T} = \begin{bmatrix} \cos(-\theta) & 0 & -\sin(-\theta) \\ 0 & 1 & 0 \\ \sin(-\theta) & 0 & \cos(-\theta) \end{bmatrix} \begin{bmatrix} 0 & 1 & 0 \\ 1 & 0 & 0 \\ 0 & 0 & 0 \end{bmatrix} \begin{bmatrix} \cos(-\theta) & 0 & \sin(-\theta) \\ 0 & 1 & 0 \\ -\sin(-\theta) & 0 & \cos(-\theta) \end{bmatrix} \quad (2.5)$$

The rotation angle θ is directly determined by the location of the joint in the array, as shown in Figure 2.3 (b). In the plan-view (looking through the silicon chip to the solder joints), considering a solder ball in the outermost row in a WLCSP package, the imposed shear stress has a component aligned along the direction marked by the red arrow. As given in equation (2.4), $\boldsymbol{\tau}_{21}$ is in the "*1*" direction in Figure 2.3 (a), and thus a rotation angle of θ about the global "*2*" direction will impose the shear stress lined up with the red arrow. The negative sign of the rotation angle in equation (2.5) indicates the rotation is clockwise. Therefore, when observing a cross-section view of the outer row on the periphery, the equivalent shear stress on each solder joint has a component going in or out of page, instead of horizontal. After normalizing $\boldsymbol{\sigma'}$, the resultant stress tensor $\widehat{\boldsymbol{\sigma}}'$ now represents a unit shear stress imposed on a given solder joint, expressed in the global coordinate system.

To calculate the Schmid factor (*m*) for a given slip system (*h k l*) [*u v w*] (represented by vectors ***n*** and ***b***), the rotated stress tensor needs to be represented in the crystal coordinate system, and this transformation is based on the transpose of the rotation matrix ***R*** (derived from three Euler angles) as defined earlier. Consequently, a generalized Schmid factor *m* for each given slip system is calculated using equation (2.6), in which $\widehat{\boldsymbol{n}}$ and $\widehat{\boldsymbol{b}}$ are the unit vectors of ***n*** and ***b***.

$$m = \hat{\boldsymbol{n}}\, \boldsymbol{R}^{T}\, \widehat{\boldsymbol{\sigma}}'\, \boldsymbol{R}\, \hat{\boldsymbol{b}} \qquad (2.6)$$

Based on the equation (2.6), all possible Sn slip systems can be sorted by their *m* values. Slip systems that have high Schmid factors may be considered as active. Further assessment of activated slip systems is accomplished by slip trace analysis as discussed earlier in this section.

Chapter 3

Effect of Sn crystal orientation on cracking in low-strain PBGA packages

3.1 Statistical assessments of Sn crystal orientation evolution in plan-view solder ball arrays

In order to understand the effect of pre-aging and thermal cycling on the crystal orientation evolution in the low-strain PBGA package design, nine packages (of eight different thermal histories) of this design were prepared. The solder joints in these samples were first examined individually using EBSD, and then summarized according to their locations in the solder array. The average *z*-axis (normal to the solder/chip interface) CTE maps are shown in Figure 3.1 in order of increasing pre-aging temperature, time, and thermal strain. Prior work by Bieler et al. (2008) discovered that, in a PBGA package subjected to thermal cycling, cracks were only found in red orientation joints (with the Sn [001] direction nearly aligned with the solder/chip interface), but not in purple orientations (with the [001] direction nearly normal to the interface) or in joints with a multi-grain structure. This finding ***provides a basis for differentiating vulnerable solder joints from those that are more resistant to failure***. With this in mind, it would be interesting to know if the distribution of Sn crystal orientations changes with varying pre-aging conditions, and whether larger cumulative strains with more thermal cycles alters the distribution. A statistical study of the effect of thermal histories on the distribution and evolution of Sn crystal orientations was therefore carried out.

Two packages in the as-fabricated condition shown in Figure 3.1 indicate a random distribution of Sn grain orientations before any deformation. Both red and purple orientations are present, and some clusters of similar orientations are observed for both orientation extremes. In this package design, maximum shear stress due to the CTE mismatch is found near the Si die edge (black boxes in Figure 3.1), whereas the shear stress level outside die area is smaller. Nevertheless, the randomness does not seem to change in the higher strain regions (such as near the Si die edge). It is yet unknown whether strain plays a role in determining the final orientation(s) after the reflow process. Recent work [Bieler et al. (2012)] on a higher strain package design suggested that during the cooling stage of the reflow process, no dramatic change of Sn grain orientation was observed once the solder ball was solidified. This indicates that the Sn grain orientations are not likely to change quickly from a change in temperature, even when the imposed strain on the solder joint is high during cooling. The second package in the as-fabricated condition shows more (damage-resistant) purple and blue orientations outside the die area.

The pre-aging alone does not alter the orientation distribution, but it does seem to affect the distribution of purple/blue orientations after the subsequent thermal cycling. For instance, there is no apparent change in the orientation distribution after isothermal aging at 150 ℃ for 1000 hours. In contrast, after pre-aging at 100 ℃ for 500 hours followed by 1400 thermal cycles (TC), more purple/blue joints are clustered, indicating a radial pattern with respect to the center of the package. This pattern is also visible in the sample after pre-aging and 2500 TC. In contrast, there are significantly fewer purple/blue joints under the Si die in the 2500TC package with no pre-aging. The majority of purple/blue orientation joints are located outside the periphery of the Si die area, with no radial distribution. It is clear that the shear strain imposed on the solder joint due to CTE mismatch is location-dependent, and the sense of shear is aligned from the solder ball to the geometric center of the package. Therefore, in the pre-aged and thermally cycled samples, a heterogeneous strain distribution during thermal cycling may be correlated with a radial distribution of purple/blue orientations that are more resistant to deformation (based on the findings reported in the literature).

The observations above may be explained by an increase of grain boundary mobility which facilitated grain boundary migration and recrystallization during thermal cycling because of the coarsening of IMC particles during the pre-aging process [Lee et al. (2009), Qasaimeh et al. (2011)]. It is not clear whether these purple/blue orientations aligned along the sense of shear are the products of recrystallization in the low to medium strain regime (up to 2500 TC). Nevertheless, isothermal aging does seem to affect the distribution of purple/blue crystal orientations after the subsequent thermal cycling. This mechanism is subject to further investigation. In the high cumulative strain regime (6400 TC), however, the radical distribution (with respect to the package center) of purple/blue orientations is not observed in Figure 3.1.

After 6400 TC, the change of grain orientation distribution is apparent, particularly in the pre-aged samples where more red/orange orientations developed after thermal cycling. In the unaged specimen, there are more purple/blue orientation joints, whereas in the 100 ℃ 500 hours aged sample, many more red joints are observed. The mechanism of the formation of red orientation joints after pre-aging and more thermal cycles is discussed later.

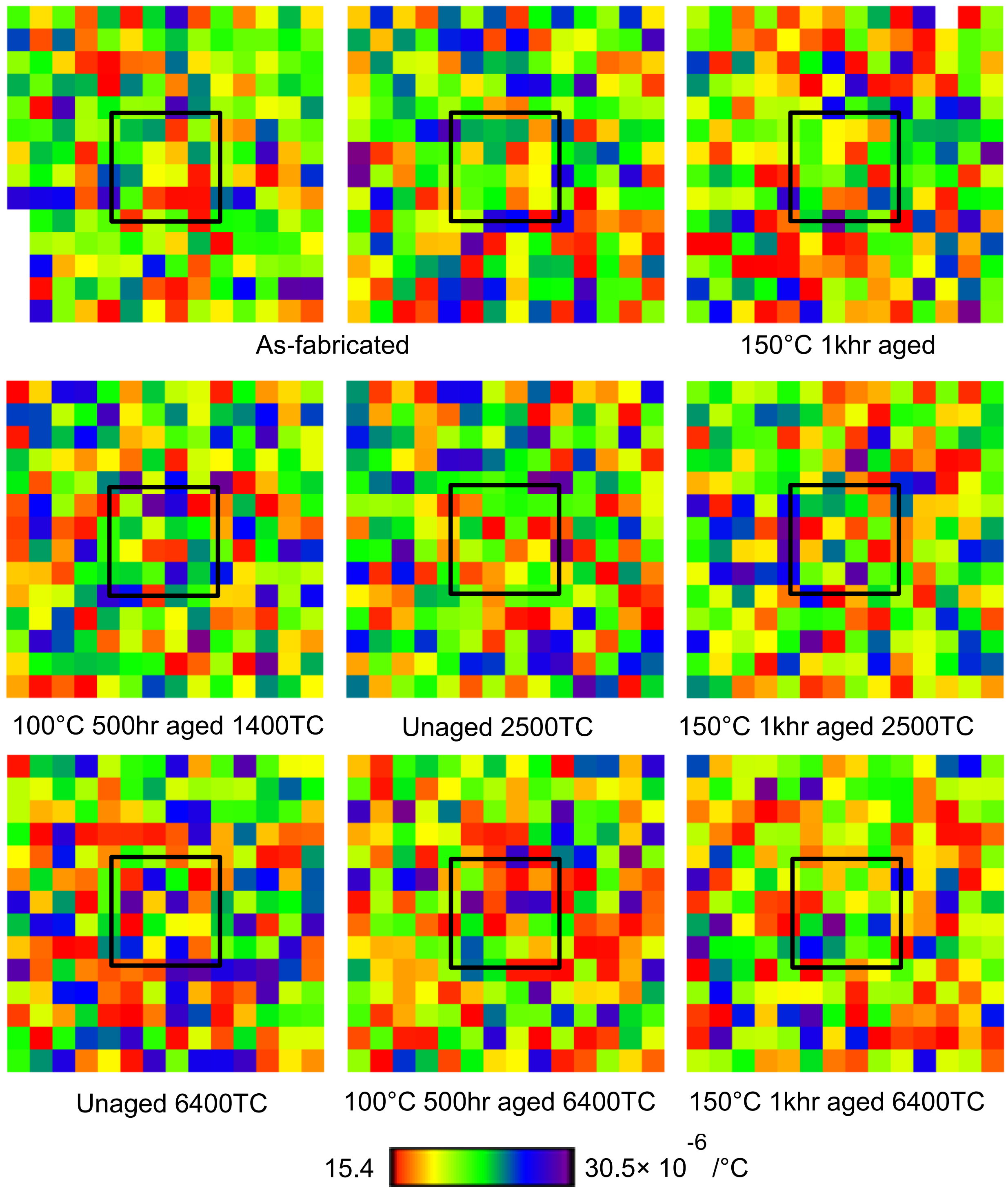

As-fabricated

150°C 1khr aged

100°C 500hr aged 1400TC

Unaged 2500TC

150°C 1khr aged 2500TC

Unaged 6400TC

100°C 500hr aged 6400TC

150°C 1khr aged 6400TC

Figure 3.1 Average *z*-axis CTE maps of packages with different processing histories; color code is shown in the inset; the solid line indicates the edge of the Si die. White pixels in the array come from solder joints that could not be indexed in EBSD [adapted from Bieler et al. (2012)].

Histograms showing the number fraction of different orientation colors are summarized in Figure 3.2, which are presented in the same order as Figure 3.1. Instead of using a continuous color spectrum in Figure 3.1, a five-color discrete color code was used to display different ranges of Sn crystal orientations. As described earlier, each of the five colors in the color spectrum represents a range of CTE values that are equally divided between $15.4\times10^{-6}/℃$ and $30.5\times10^{-6}/℃$. This allows a direct comparison of the distributions of different grain orientations in samples with various thermal histories with the same package design.

It is apparent that, in the as-fabricated condition, even two packages with the same design, alloy composition, and well-controlled reflow profile yield a different Sn grain orientation distribution in a solder array. Moreover, the significantly lower population of purple/blue orientation joints, as appear in all samples and conditions, suggests that these orientations are in a minority in a solder array upon solidification. Since purple/blue orientation are more resistant to deformation and fracture during thermal cycling, lack of these orientations in the as-fabricated condition may make the solder joints more vulnerable to cracking upon thermal loading. It is yet unclear how to effectively control the Sn crystal orientation in solder joints under the industrial reflow process. Consequently, in this context, each solder joint in a different package is a special case.

After isothermal aging alone, the number fraction of different orientations remains similar compared to the as-fabricated samples. This is no surprise as reviewed earlier that a dramatic change of microstructure and crystal orientation occurs during recrystallization, which is triggered by the cyclic straining during thermal cycling. Nevertheless, the annealing process during isothermal aging does alter the subgrain boundary characteristics and the morphology of IMCs, which play important roles during the subsequent thermal cycling.

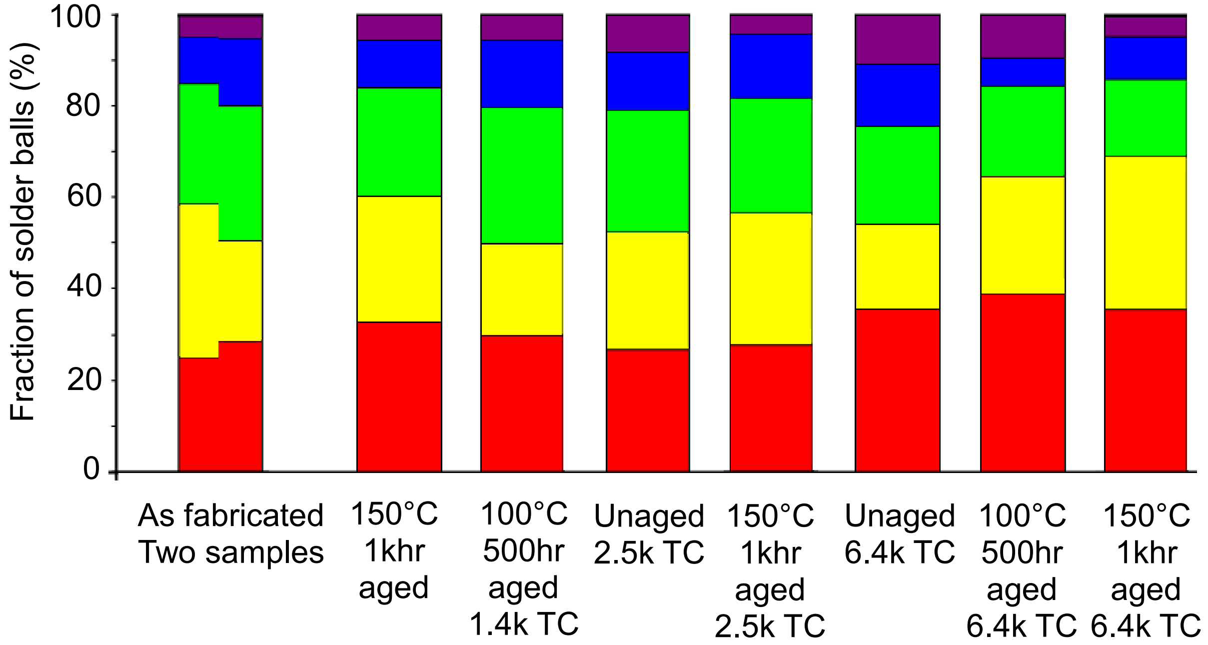

Figure 3.2 Number fraction of the average *z*-axis (normal to the chip/solder interface) CTE values of solder balls in PBGA packages with different thermal histories.

In the lower cumulative strain regime (100 ℃ aged+1400TC, unaged+2500TC, and 150 ℃ aged+2500TC), the number of purple/blue orientation joints as well as the red orientations remains nearly constant in these three samples, whereas a balanced monotonic change of the green to yellow orientations with increasing pre-aging conditions is observed. The same change is also apparent with the larger cumulative strain after 6400TC, as shown in Figure 3.2. This change of orientation distribution could be attributed to continuous recrystallization, where a gradual lattice rotation during thermal straining from a green to a yellow orientation may be correlated with the grain boundary migration. The enhancement of boundary mobility is a likely result of fewer and larger IMCs that develop from the isothermal aging conditions. As purple and red orientations are the two extreme cases, green represent median orientations that have the least thermal stress in the direction normal to the chip/solder interface. It is thus possible that the green orientations are able to activate some facile slip systems, and the greater ease of transition to the yellow orientations could be a result of dislocation slip activities. There is also an overall increase in the red orientations in the three samples after 6400TC, which is discussed as follows.

In the high cumulative strain regime, after 6400 TC, the large amount of red orientation joints suggests that recrystallization may be able to develop red orientations preferentially when the strain is higher. It is also noted that samples after 6400 TC have less green orientations than other conditions. It is thus speculated that more vulnerable red orientation joints may be the product of a stochastic gradual recrystallization process from the green orientations (by stochastic, it is more likely that green orientations may transform to yellow, that yellow may transform to red, etc.). The decrease in purple/blue orientations in the samples with high pre-aging temperature and more cumulative strain indicates that orientations that are more resistant to deformation may also evolve toward more vulnerable orientations when the thermal strain is high (6400TC). Grain boundary migration responsible for this transition is facilitated by the pre-aging process, as described earlier.

In the plan-view assessments, the crystal orientations revealed by this method only reflect the bulk orientation in the solder joints, whereas the cracked regions (and nearly half of the joint) were removed. Consequently, this provides little information about the contribution of different Sn crystal orientations on cracking. In order to characterize the microstructure and crystal orientation in solder balls in the vicinity of the cracks, three packages after 6400TC with different pre-aging conditions (un-aged, 100 ℃ 500 hours aged, and 150 ℃ 1000 hours aged) were prepared. For each package, two rows of solder joints in the middle of the PBGA package were cross-sectioned, polished, and examined using the optical microscope and EBSD. Correlation between the Sn crystal orientation and cracking is discussed in the following sections.

3.2 Cross-section analysis of the correlation between Sn crystal orientation and cracking

The correlation between the Sn crystal orientation and cracking was assessed on cross-sectioned samples with three different thermal histories. The locations and the lengths of cracks after thermal cycling were determined from the PLM micrographs, as shown in Figure 3.3. The samples were also characterized by EBSD, and the *c*-axis orientation maps are displayed. Different Sn crystal orientations and high angle grain boundaries can be visualized from both the PLM micrographs and the EBSD maps. For each solder ball, the observed cracks are indicated by gold boxes above its optical micrograph, and the blue box represents the intact fraction of the joint.

Cracking was studied only in the samples after 6400TC since in rare cases were cracks observed in the samples after 2500TC. After 6400TC, all cracks occurred near the chip-side interface of the solder balls, and no board-side fracture was observed. In contrast to the work by Bieler et al. (2008), cracks in this PBGA package were found in a variety of Sn crystal orientations. No only red orientations, but yellow and green orientations also contributed to cracking. Moreover, cracks were also found in solder balls with a multi-grain structure. In all six samples with three different pre-aging conditions, no cracks occurred in purple/blue orientation joints, which agrees with prior work. There is only one case where the solder ball has a dominant blue orientation and partially cracked (Ball 11 in the first row of unaged+6400TC sample). Nevertheless, the crack propagated only in the upper right corner of the joint where an orange orientation is present, indicating that the orange orientation is responsible for cracking rather than the dominant blue orientation. Therefore, it is reasonable to state that no blue orientation joints were correlated with cracking.

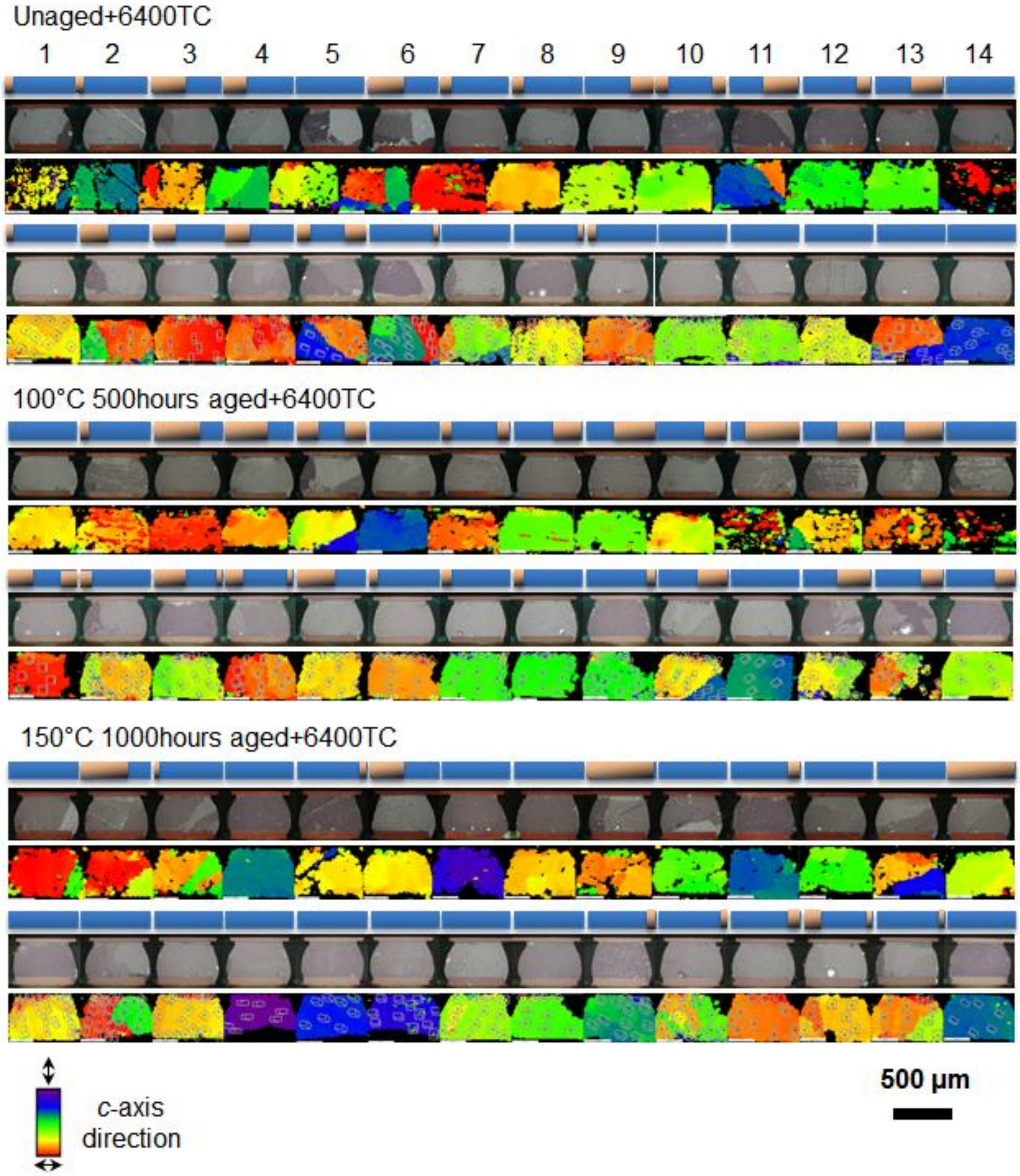

Figure 3.3 The PLM micrographs and the corresponding *c*-axis EBSD maps of the specimens with different pre-aging conditions. The gold box above the joint indicates the position and the length of the observed cracks, and the blue box indicates the intact part of the ball.

To further expand the observations, in solder joints with a multi-grain structure, one crystal orientation may be more prone to fracture than the other orientations. For instance, Ball 6 in the first row of the unaged samples has three crystal orientations. A partial crack propagated nearly halfway along the upper left corner of the joint, whereas the upper right portion of the ball remained intact. It is apparent that the red orientation on the left is directly correlated with cracking in this joint, and the dark green orientation may be more resistant to deformation where no crack developed. Similar phenomena are evident in Ball 6 of the second row in the unaged group. A crack is found only at the upper right corner where a red orientation grain is present, and there is no fracture in the green/dark green region near the left corner of this ball.

In rare cases for this package, the red orientation did not crack during thermal cycling. In these cases, the response of a solder joint with a multi-grain structure to the thermal strain may also depend on the relative ease for slip in the minority orientation. For instance, as shown in Figure 3.4, both Ball 1 and Ball 2 in the first row of the 150 ℃ aged specimen have a majority red orientation and a minority twin-related green orientation in the lower right part of the joint. No cracks developed in Ball 1, but Ball 2 cracked halfway near the upper left chip-side interface. The different deformation behaviors shown here may be first attributed to the dominant red orientation. It is apparent that the *c*-axes of these two red orientations are nearly perpendicular to each other, which may activate different slip systems under a global shear stress. It is also noted that the minority green orientations in the two joints are different, and the plastic responses of the minority orientations may influence the deformation behavior of the whole joint. In order to understand the correlation between the Sn grain orientation and fracture in these two multi-crystal joints, active slip systems from the dominant and the minority grain orientations are estimated based upon the computed Schmid factors, assuming a global shear stress (Table 3.1).

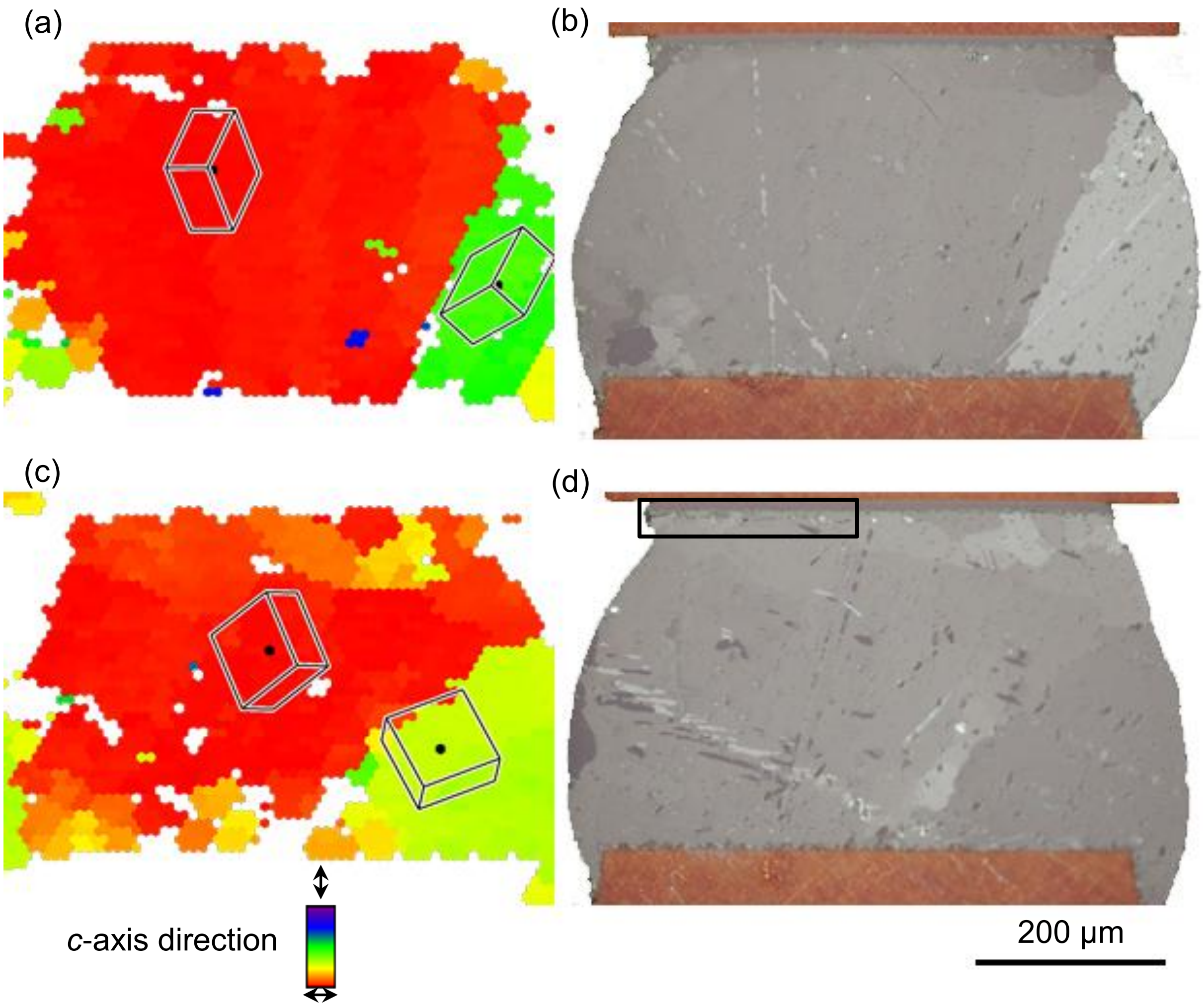

Figure 3.4 Two neighboring solder joints (with a similar multi-grain twinned structure) in a 150 ℃ 1000 hours aged+6400TC sample; (a) *c*-axis EBSD map of Ball 1 with a dominant red and a minority green orientation; (b) corresponding PLM micrograph of Ball 1 with some recrystallization but no crack; (c) *c*-axis EBSD map of Ball 2 with a different red orientation and a light green grain; (d) corresponding PLM micrograph of Ball 2 with a black box showing the location of a transgranular crack.

Considering the contribution to deformation from the major orientation, the dominant red orientation in both joints favors some facile slip systems (slip system #2, #4, and #1 for Ball 1; #4 and #2 for Ball 2) with high Schmid factors. Direct comparison of slip systems with high Schmid factors does not reveal a significant difference in the likelihood of slip in Ball 1 and Ball 2. In other words, both joint may be able to deform by dislocation glide on facile slip systems. If an easy slip in the dominant grain orientation does not facilitate cracking, other factors may have contributed. Since both joints have a multi-grain structure, a similar analysis of active slip systems was carried out based upon the minority orientation.

The minority green orientation in Ball 2 may have activated more facile slip systems with high Schmid factors during thermal straining, which contributed to fracture. For Ball 1, the green orientation in the lower right part of the solder ball exhibited more resistance to slip. The top five slip systems (slip system #10, #9, and #6) with high Schmid factors are all non-facile slip systems, indicating that this is probably a hard orientation. In contrast, the counterpart in Ball 2 (a light green orientation in a similar location) has facile slip system #4 with high Schmid factors, suggesting a high probability to slip under a global shear stress. Consequently, the crack development in the solder joint may be correlated with the interplay of different orientations present in the joint, and their relative ease to strain. In Ball 2, for instance, both the dominant red and the minority green orientation are able to deform on facile slip systems. With the same thermal history and a similar stress level, however, slip in Ball 1 experienced greater resistance from the minority green orientation, which may have retarded the overall deformation in this solder joint, suppressing the crack development. Cracking in Ball 2 may also be correlated with an apparent recrystallization event near the chip-side interface. The contribution from recrystallization to cracking is discussed in detail later.

Table 3.1 Slip system families (Table 1.2) with the highest Schmid factors for different grain orientations.

	Slip systems families				
Ball 1 (red)	# 2	# 8	#4	#1	#7
Schmid factor	0.631	0.631	0.525	0.452	0.452
Ball 1 (green)	#10	#10	#9	#9	#6
Schmid factor	0.638	0.614	0.522	0.442	0.427
Ball 2 (red)	#4	#10	#6	#4	#2
Schmid factor	0.558	0.506	0.469	0.461	0.437
Ball 2 (green)	#6	#10	#4	#10	#4
Schmid factor	0.538	0.52	0.511	0.507	0.478

Although recrystallization occurred in both Ball 1 and Ball 2, it appears that the transgranular crack shown in Ball 2 is not directly related to recrystallization. Near the upper right corner of Ball 2 where recrystallized grains were observed, no crack developed. The grain orientation evolution is visible in both the PLM micrographs and the EBSD orientation maps in Ball 1 near the upper right and lower left corners, but no crack is apparent in either of these areas. This suggests that the deformation behavior of the bulk red orientations may have had a greater impact on crack development than the intergranular cracking assisted by recrystallization. As the dominant red orientation has facile slip systems activated, a crack may develop more easily in some red orientations that may not require the vulnerable grain boundaries provided by the recrystallization.

In order to gain a statistical sense of the correlation between fracture and the dominant Sn crystal orientation, the cumulative lengths of the cracked and the intact parts of each joint were measured from the optical micrographs. To better represent the statistics, Sn crystal orientations are categorized into five different color groups based on the angles between the *c*-axes of the dominant orientations and the interface plane normal direction. The minimum and maximum angles are 0 ° and 90 °, and are correlated with the purple and red colors, respectively. More specifically, the orientation is shown as “red” when this angle is within the range 72 °-90 °, “yellow” for 54°-72°, “green” for 36°-54°, “blue” for 18°-36°, and “purple” for “0°-18 °. For each pre-aging condition, the cumulative lengths were measured individually for the two adjacent rows of solder balls displayed in Figure 3.3. The measurements of the cumulative lengths of all joints with different thermal histories were assessed using the same color code in the right most bars in Figure 3.5. For the cracked population, the number fractions of the red, yellow, and green orientations in each pre-aging conditions are noted. For the intact population, similar statistics are shown for the same orientation colors. It is apparent in Figure 3.5 that the cumulative lengths of the intact and the cracked parts of the joints differ by a factor of three, and the intact length is significantly longer than the cracked length. This indicates that in the low-strain PBGA packages, crack development was not dramatic, even after 6400TC.

It is noted in Figure 3.5 that a variety of grain orientations are correlated with cracking and approximately 50% the cumulative crack length is correlated with the red orientations. Other major contributors to cracking are the yellow and green orientations, which are responsible for the other half of the cumulative crack length in the “Average” column. No cracks were found in the purple/blue orientation joints. A large fraction of the yellow and green orientations that are correlated with cracking apparently contradicts prior work [Bieler et al. (2008)]. Nevertheless, the larger fraction of green and yellow orientations in the cracked population may be attributed to sampling more joints with these two orientations.

The cumulative lengths of the intact regions in the same samples were also measured and correlated with the dominant Sn grain orientations. The statistics from the intact population are shown in the lower part of Figure 3.5. In the “Average” column, it is apparent that the green and yellow orientations have similar number fractions as the statistics in the cracked population, suggesting that a strong correlation between the dominant green and yellow orientations and cracking is not convincing, in fact there are slightly more yellow orientations in the intact colony. Also the green orientations have similar number fractions in the cracked and intact populations. However, the number fraction of red orientations is significantly lower in the intact population than in the cracked population, clearly indicating that these orientations are more prone to cracking. Since no solder joints with dominant purple/blue orientations cracked, statistics from these two orientations only appear in the intact colony.

The pre-aging condition has a significant impact on the responses of red and yellow crystal orientations on crack development. With no pre-aging, after 6400 TC, the red orientation joints contribute about 62% of the cumulative crack lengths. When aging temperature and time are increased, the contribution from the red orientations to cracking decreases. As reviewed earlier, isothermal aging prior to thermal cycling may facilitate the grain boundary migration required for recrystallization and the subsequent intergranular fracture. If a solder joint with a red orientation is able to develop recrystallized regions that gradually evolve into a new orientation that is less likely to deform, the solder joint may be able to have a longer life time. On the other hand, the number fraction of the cumulative crack length in yellow orientation joints increases monotonically from 19% to 32% and to 47% with higher aging temperature and longer aging time. This indicates that the contribution to cracking from the yellow orientations increases with the pre-aging condition, which may result from the evolution of the yellow orientations toward the more vulnerable red orientations by recrystallization.

The lower number fraction of green orientations in the cracked population is observed in the 150 °aged condition. This suggests that fewer cracks were observed in green orientation joints with higher pre-aging temperature and longer pre-aging time. Grain orientation evolution towards the yellow orientation may have occurred in green orientation joints via recrystallization, which is facilitated by this pre-aging condition. This has also been discussed earlier in the plan-view assessments.

Overall, considering all solder joints examined, the red orientations (with the *c*-axis nearly aligned with the interface) contributed to nearly half of the cumulative crack length. The next greatest contributor is the yellow orientations. Figure 3.5 suggests no dominant blue orientation is correlated with cracking. There is a discrepancy between the present work and the prior study [Bieler et al. (2008)] regarding the green/yellow orientations and their susceptibility for crack development. Specifically, no green/yellow orientation joints cracked in the prior work. In the present study, however, cracks were also observed in solder joints with dominant green/yellow color orientations. The statistics in Figure 3.5 indicates similar number fractions of green/yellow orientations in both the cracked and intact population, suggesting that these two orientation colors are not strongly correlated with cracking. Nevertheless, based upon the bulk orientation, it appears that a variety of crystal orientations are correlated with cracking. Because cracks formed in the region near the chip-side interface, a detailed assessment of the grain orientations near the crack needs to be discussed as well.

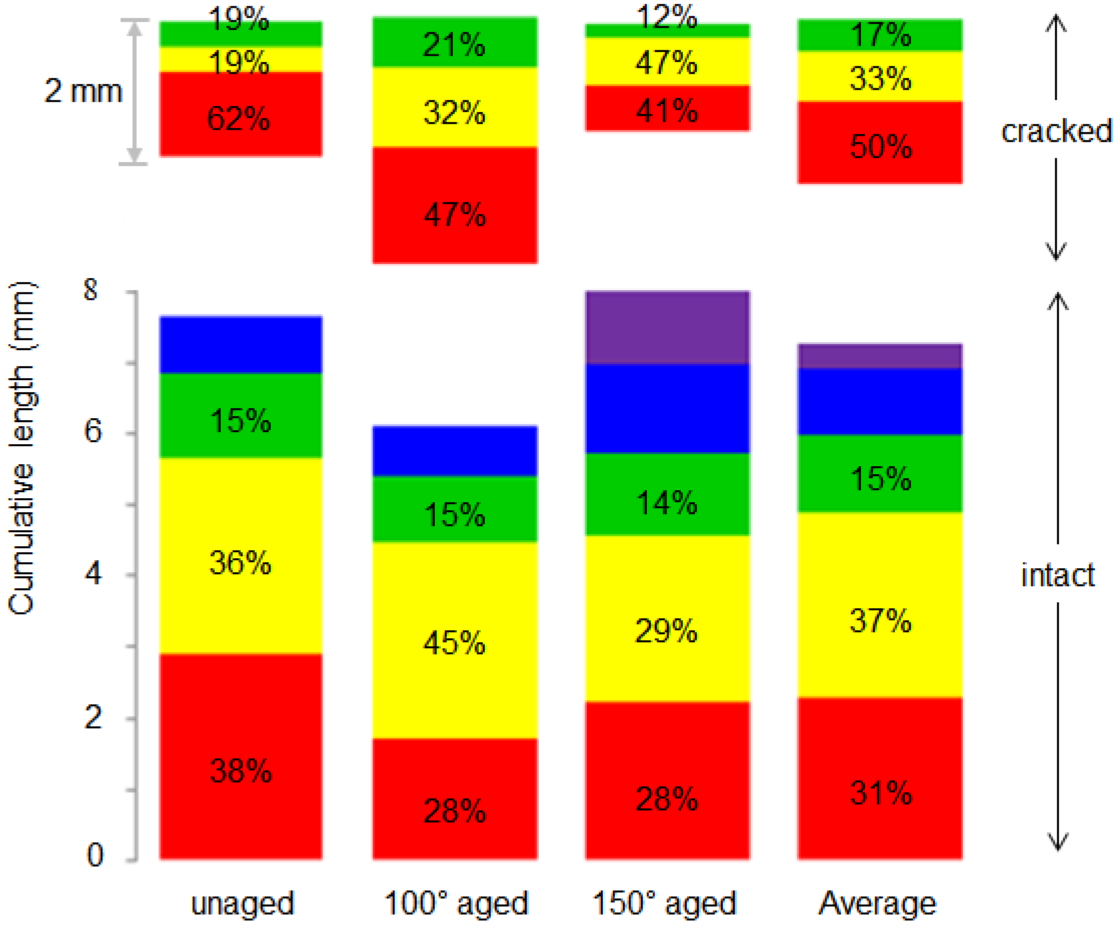

Figure 3.5 The cumulative lengths of the cracked and the intact parts of the solder joints after 6400TC are correlated with the dominant Sn crystal orientations; the number fractions of different orientation colors are based on either the cracked or intact populations indicated for each of the different pre-aging conditions; the "Average" column is the average of the three conditions on the left.

3.3 Recrystallization and its role in crack propagation

A particular case illustrating how green orientations may be correlated with cracking through recrystallization in a solder joint is shown in Figure 3.6. Ball 8 in the first row of a 100 ℃ 500hours aged and 6400 TC sample is a green orientation joint that exhibited a crack near the upper right corner of the ball. Based on the prior statistical analysis, a sizeable fraction of the total crack length occurred in joints with a green orientation, such as this one. However, a closer examination using a finer-step EBSD scan in the area adjacent to the crack reveals recrystallization and significant Sn lattice rotations. Figure 3.6 (a) suggests that instead of the bulk green orientation, the newly developed red orientation just above the crack is more likely to be responsible for the fracture. The EBSD clean-up process has filled in some cracked areas at the upper right corner of the joint. Nevertheless, a comparison between Figure 3.6 (a) and (c) clearly displays the crack location.

Microstructure evolution and recrystallization preceding crack propagation is apparent in Figure 3.6. Recrystallization also occurred near the chip-side interface beyond the crack tip, further to left, shown as an orange/yellow orientation in Figure 3.6 (a) and (b). Closer inspection reveals that these orientations also developed by gradual lattice rotations about a Sn [100] axis from the yellow-green orientation, as discussed earlier. In contrast, the recrystallized orientation on the upper right corner of the joint is more complex than a simple lattice rotation. These contrasting regions suggest that two types of recrystallization took place: one with gradual rotations from the parent orientation, and the other with significantly different orientations that appear more random. It is possible that the recrystallized red grain orientation could have developed by a multi-step lattice rotation, and this possibility will be discussed later in this section.

The crack propagation depends on the microstructure. The recrystallized fine grains are more prone to cracking, whereas the grain orientation similar to the parent grain impeded crack development. As shown in Figure 3.6 (a), the crack didn't propagate beyond the recrystallized region, and it stopped before it reached the yellow-green orientation on the left side of the ball. From the Sn unit cells on the fine-step EBSD map, this yellow-green orientation which may have had impeded crack propagation has a small misorientation with the dominant green orientation. The unit cells clearly indicate a lattice rotation about the Sn [100] direction between the yellow-green orientation and the bulk green orientation. It is likely that this rotation developed prior to recrystallization through gradual lattice rotation. This similarity in grain orientations suggests that this yellow-green orientation at the crack tip may have a similar resistance to cracking as the bulk orientation. If so, the crack propagation is instead facilitated by the recrystallization through which high angle grain boundaries have formed. As discussed earlier, a red orientation may deform preferentially when subject to thermal strain. The red orientation developed by recrystallization has a significantly different CTE with the bulk green orientation. Therefore intrinsically, the CTE mismatch between the green and red orientations becomes a driving force for the intergranular crack propagation. Once the crack tip reached the yellow-green orientation region, as this orientation itself is not as favored for plastic deformation as the red orientation, lack of the recrystallized microstructure suppresses further development of the crack.

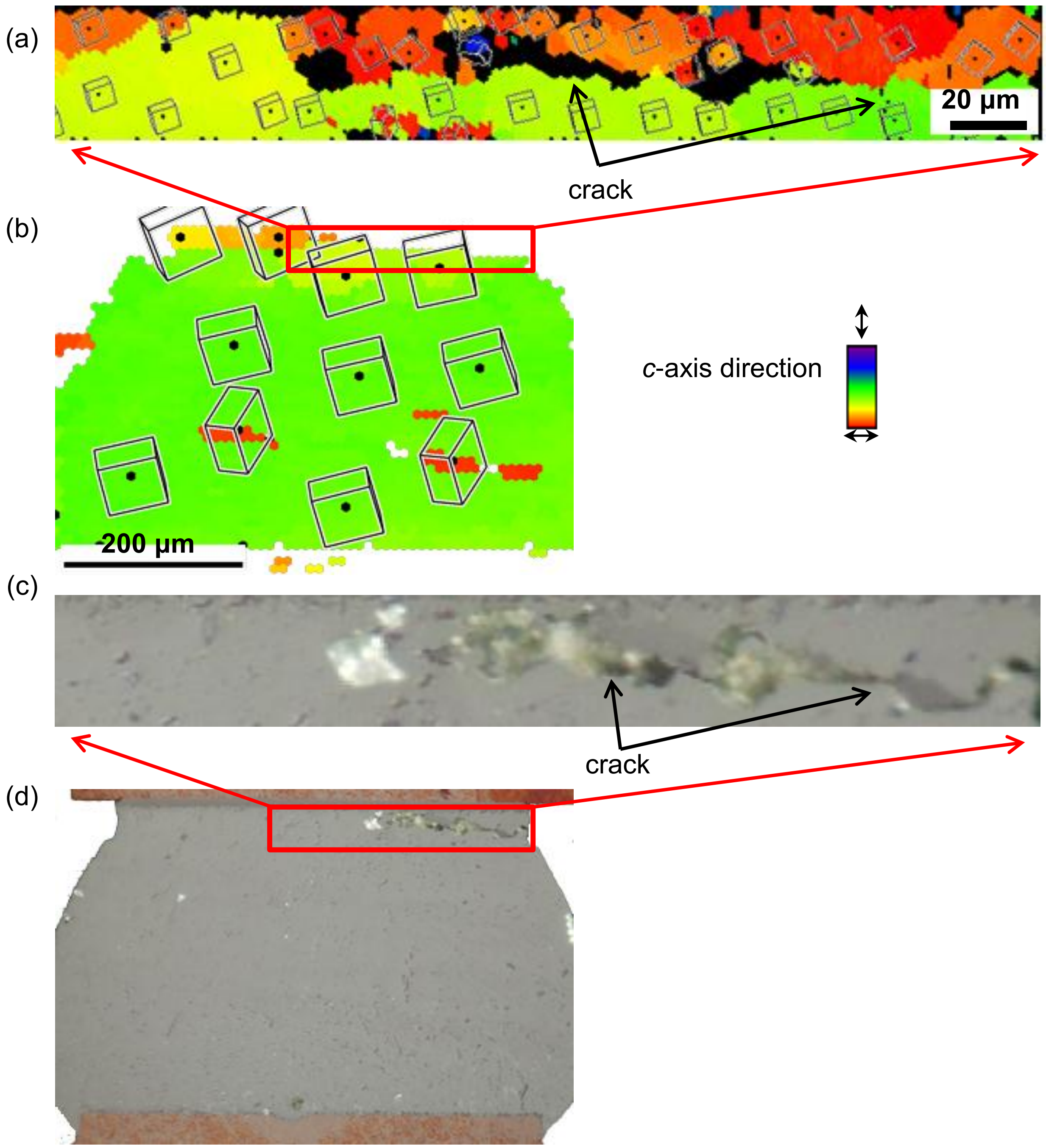

Figure 3.6 Ball 8 in the 100 ℃/500hour aged+6400TC sample: (a) and (c) fine step *c*-axis EBSD map and the PLM micrograph in the interface region near the observed crack; (b) *c*-axis EBSD map and (d) the PLM micrograph illustrating the dominant orientation and the crack near the upper right corner, as in (a).

The observation of recrystallization and the effect of red orientations on crack development in a solder ball with a dominant green orientation suggest that a re-assessment of the correlation between the Sn grain orientation and cracking is needed. Inspection of the recrystallized region using a fine-step EBSD scan reveals the correlations between crystal orientations and cracking. In the statistical analysis of the relationship between the bulk orientations and the cumulative crack lengths in Figure 3.5, recrystallization was not considered. In this context, as shown in Figure 3.5, red orientations contribute to about half of the cumulative crack length. This number thus represents a lower bound on the likelihood of red orientations causing cracking. When recrystallization is included in the discussion, however, the contribution from green and yellow orientations on cracking can be re-examined with an alternative approach that includes the recrystallized grain orientations.

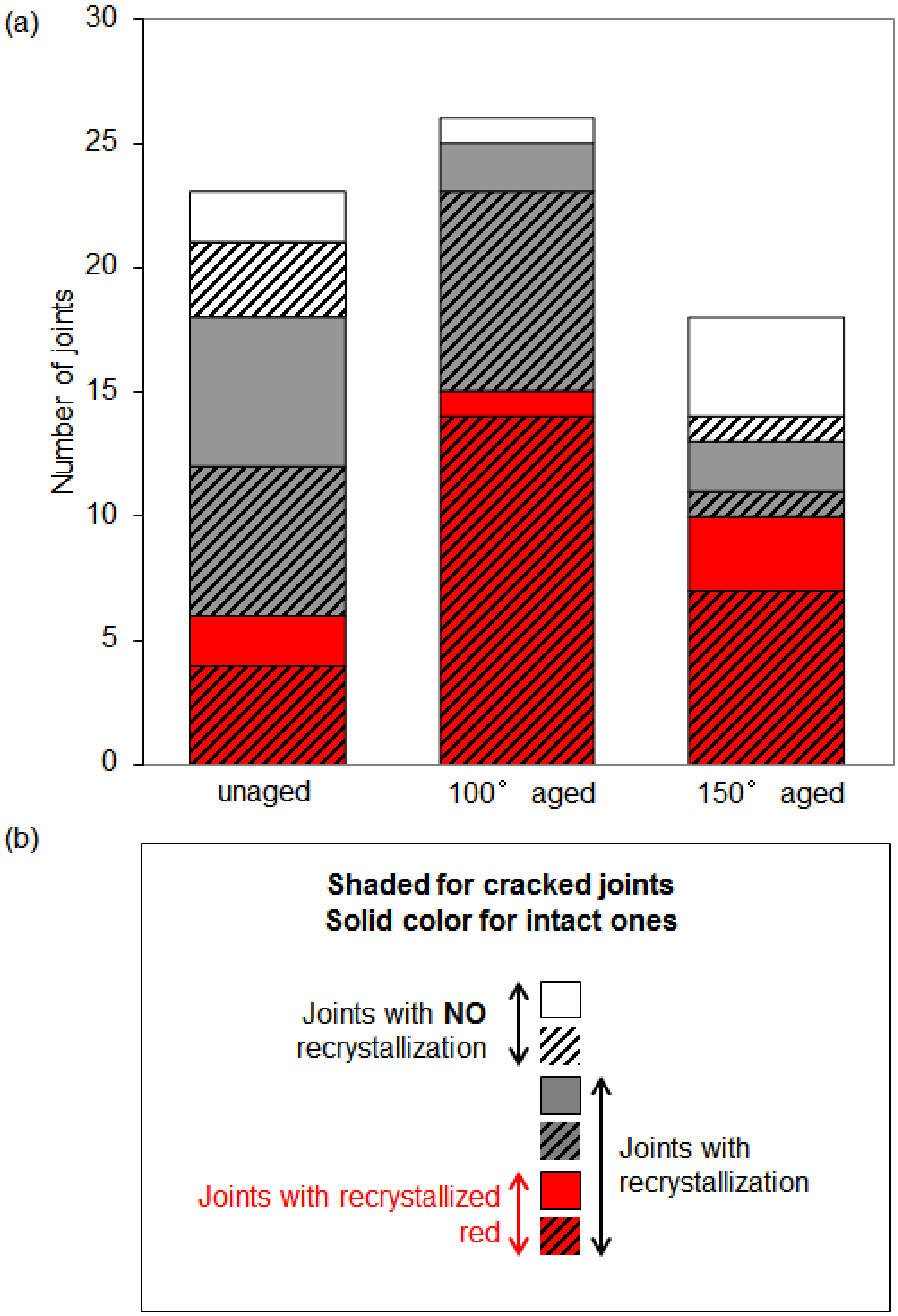

Figure 3.7 (a) Histogram showing the correlation between recrystallization and cracking from the same population of solder balls as Figure 3.5; (b) explanation of the color and pattern fill.

From the finer-step EBSD scans, Sn grain orientations adjacent to the cracks are revealed, and a strong correlation between recrystallization and cracking is observed. Among all the solder balls listed in Figure 3.3, 67 of them were examined, and 56 out of 67 joints exhibited apparent recrystallization. There are 44 out of 67 joints cracked, and within the 44 cracked joints, recrystallization was observed in 40 balls. This agrees with prior analysis that there is a strong correlation between recrystallization and cracking [Sundelin et al. (2008), Henderson et al. (2004), Yin et al. (2012), and Bieler et al. (2008)]. In addition, for the 16 joints that showed recrystallization but did not crack, 8 of them have dominant green orientations, 4 of them yellow, and the rest 4 joints have dominant red orientations. This phenomenon occurred most frequently in the unaged and thermally cycled samples. This suggests that for a solder joint with a dominant green orientation, recrystallized orientations can either facilitate or resist crack development, and the lack of grain boundary mobility in the unaged condition minimize the tendency to form a preferred soft orientation during recrystallization.

A detailed assessment between recrystallized grain orientations and cracking is accomplished by putting all 67 solder joints into six categories. For instance, as shown in Figure 3.7 (b), shaded blocks represent cracked joints, whereas a solid color indicates the intact joints. Solder joints exhibiting no apparent recrystallization are white. Grey and red colors display solder balls with obvious recrystallization. Specifically, the red color represents the population with the presence of red grain orientations developed by recrystallization (annotated “recrystallized red orientation”).

The effect of recrystallized red orientations on cracking is quantified by the shaded red blocks, and is strongly correlated with the pre-aging condition in Figure 3.7 (a). This type of red grain orientation is correlated with about 62.5% of all 40 cracked joints with apparent recrystallization. The contribution of the recrystallized red orientation to cracking dramatically increases with increasing pre-aging temperature and time. For the unaged recrystallized fractured populations, the contribution from recrystallized red orientation is less than other recrystallized orientations. However, after 100 ℃ aging and thermal cycling, there are nearly twice as many fractured joints with recrystallized red orientations than the recrystallized non-red orientations. This ratio jumps to 7 in the 150 ℃ aged and thermally cycled condition. A growing correlation between the recrystallized red orientation and cracking after pre-aging suggests that aging causes red orientations to be more easily developed during thermal cycling under this condition. Once the red orientations emerge during recrystallization, the effect of a larger CTE mismatch and the ease of slip make the grain boundary between this orientation and the parent grain vulnerable, and thus it provides an easier path for the crack propagation. Based on the discussion above, it is concluded that during thermal cycling, cracking of solder joints in the PBGA package design is highly correlated with the red color grain orientations either initially present or developed during deformation by recrystallization.

3.4 Continuous recrystallization and evolution of grain boundary characteristics

In order to understand how continuous recrystallization occurs in a green orientation, and to identify how grain boundary evolution occurs during thermal cycling, one solder joint from each of the two conditions, unaged and 100 ℃ aged were selected from the data sets after 2500 and 6400TC. The grain boundary misorientation distribution, the PLM micrographs, and the fine-step EBSD orientation and boundary maps are shown in Figures 3.8-3.9. The unit cells showing both orientations are listed in the inset of Figures 3.8 (d) and 3.9 (d).

Development of new grain orientations during the continuous recrystallization process is accomplished by gradual lattice rotations, as shown in Figure 3.8 (a) and (b). The recrystallized blue orientation grains surrounded by high angle grain boundaries (blue lines) appear to have developed from low angle boundaries (white lines). The sense of increasing grain boundary misorientations is obvious towards the left part of the joint in Figure 3.8 (b). The lattice rotation about approximate Sn [100] and [110] axes led to formation of the blue and dark green color orientations. Selected grain boundary misorientation angles are displayed at the boundaries in Figure 3.8 (a). It is noted that the misorientation between the light blue grain at the crack tip and the parent green orientation is 42°. The large misorientation angle suggests that development of this recrystallized grain *directly* from the bulk orientation may be less likely than the continuous recrystallization where subgrain boundaries gradually increase their boundary misorientations. A path across low angle boundaries can be found starting from the parent green orientation at the upper right, through the 9°, 10°, and 11° boundaries going to the left in Figure 3.8 (a). In addition, there is a path from the lower left green orientation to the right through the 9°, 12°, and 11° boundaries. In contrast, going vertically from the green orientation directly into the recrystallized blue grain, there is a 42° misorientation.

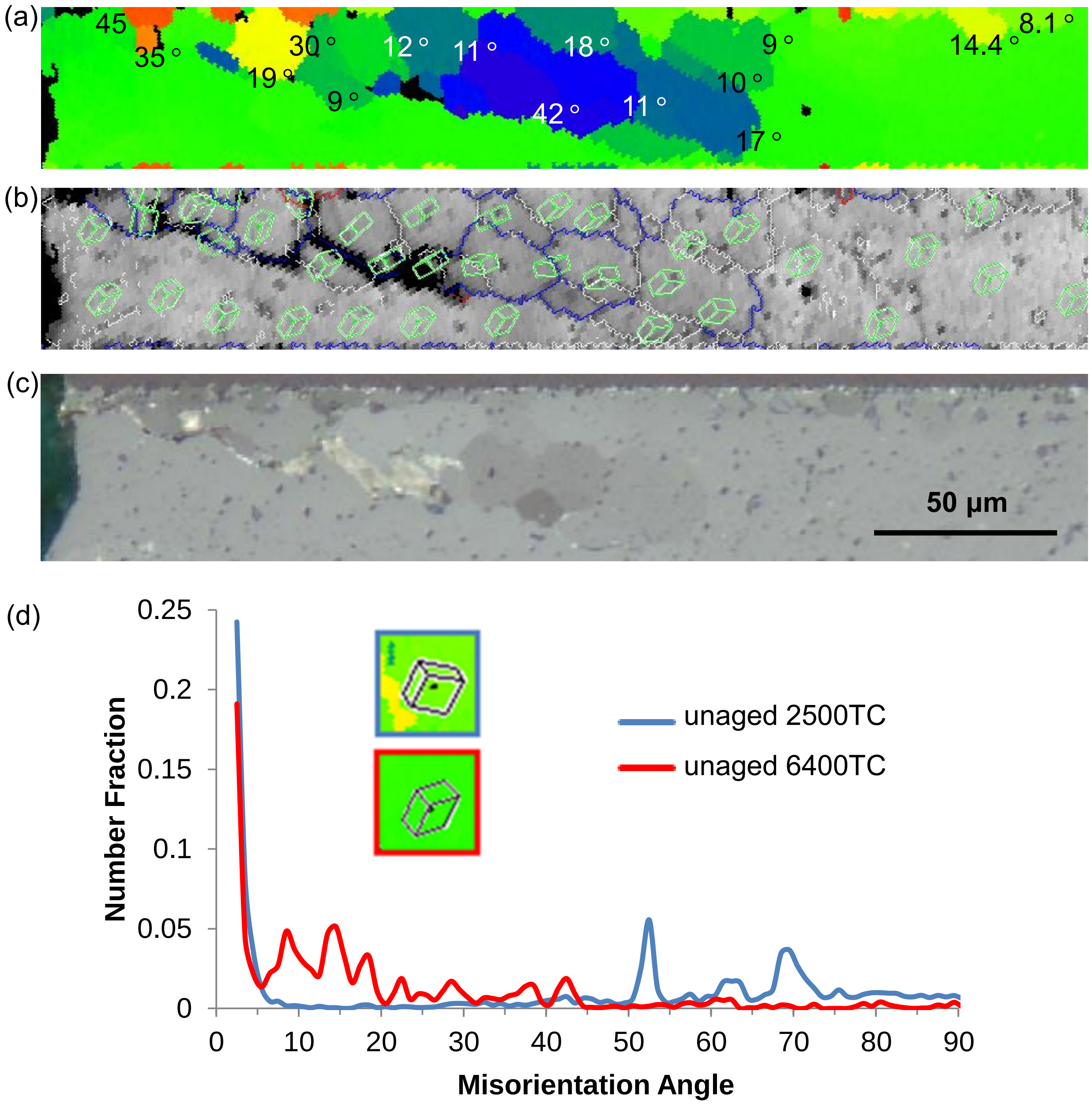

Figure 3.8 Ball 4 in the unaged+6400TC sample: (a) the fine step *c*-axis EBSD map shows recrystallization and selected boundary misorientation angles; (b) image quality map with grain boundaries highlighted: white are low angle (<15 °), blue are high angle, and red are near-twin (55-65 °) boundaries, and (c) PLM micrograph, where cracked regions appear light; (d) comparison of the misorientation angle distribution with a 2500TC sample with a similar *c*-axis orientation.

In addition to the blue and dark green color orientations developed by continuous recrystallization, discontinuous recrystallized yellow and orange grains are also observed. The yellow grain, for instance, resides in the vicinity of the crack. It has a 19 ° misorientation with the bulk grain orientation on the opposite side of the crack. Closer inspection of the unit cell reveals that development of this grain may be accomplished by lattice rotations around Sn [100] and [001] axes, which could be accomplished by the edge dislocation slip on slip systems #1, #7, and #9, and slip systems #3 and #5 (Table 1.2), respectively. Given the large misorientatation angle, multiple-step of lattice rotations may have occurred during recrystallization. The orange orientations just above and near the yellow grain, however, have 35 °-45 ° misorientations with the dominant green orientation. This suggests operation of a discontinuous recrystallization mechanism. Also, the orange orientation has a ~60 ° twinning relation with the yellow grain, as shown in Figure 3.8 (b) by red lines near the top left edge of the micrograph. It is possible that formation of the yellow grain preceded the orange orientation, and the high strain concentration near the interface may have stimulated a mechanical twin. As noted earlier, the yellow orientation may be developed through a continuous recrystallization mechanism by gradual lattice rotations. Since both lower angle boundaries and special boundaries are involved in this type of transition, less energy may be needed in comparison to the processes that lead to discontinuous mechanism to recrystallize directly from the parent orientation.

The grain boundary misorientation distribution of this joint was compared with another unaged solder joint (with a similar *c*-axis orientation) after 2500TC. Figure 3.8 (d) reveals a large fraction of low angle grain boundaries in the 2500TC sample, and there are peaks at the ~52 °, ~62 °, and 70 ° misorientations. In comparison, the solder ball after 6400 TC exhibited a dramatic increase in grain boundaries with 10 °-20 ° misorientations, and a decrease in low angle boundaries. An increased presence of low-angle boundaries signals a starting condition for continuous recrystallization. A higher population of the 5 °boundaries at the 2500TC than the 6400TC is observed in Figure 3.8 (d). With more thermal cycles, peaks at values greater than 5 ° at the 6400TC are consistent with the increase of grain boundary misorientation due to the absorption of dislocations into low-angle boundaries.

Continuous recrystallization preceding crack propagation is evident in Figure 3.8 (a)-(c). There is no crack that expanded beyond the recrystallized microstructure, which agrees with the observations reported in the literature, as discussed earlier. In addition, this special case provides additional information which is often lacking in the literature regarding the effect of the Sn crystal orientation on crack propagation. Interestingly, although apparent recrystallization occurred, the crack tip stopped at the blue color orientation. As discussed earlier, the blue orientation is more resistant to plastic deformation during thermal cycling. Thus, the presence of the blue grain apparently retarded further expanding of the crack, even though the recrystallized high angle grain boundaries are still present along the crack propagation path. In this dissertation, the main task is to understand the microstructure and the Sn crystal orientation evolution during the recrystallization process that provides a pre-condition for crack propagation. The effects of different recrystallized grain orientations on crack development are crucial, and will be discussed further.

The contribution to cracking from the recrystallized red orientation has been discussed earlier in Ball 8 of the 100 ℃ pre-aged sample. Development of this recrystallization red orientation is accomplished by continuous recrystallization, during which a gradual lattice rotation is observed. In Figure 3.9 (a), the misorientation angles labeled at the boundaries indicate a gradual lattice rotation from the parent orientation to the recrystallized red orientation via a series of lower angle boundaries (6 °, 16 °, and 21 °). On the left of Figure 3.9 (a), it is apparent that orange orientations developed by lattice rotations through 8 °, 9 °, and 10 ° low angle boundaries. As discussed before, the recrystallization on the left side of the chip-side interface did not introduce a crack. Crack propagation was stopped at an orientation that is less favored to deform.

This continuous evolution of grain boundary misorientations is shown in Figure 3.9 (d) in terms of the misorientation angle distribution. A comparison between two joints with the same pre-aging condition (and similar *c*-axis orientations) shows that after more thermal cycles (6400TC), there is a larger fraction of 5 °-10 ° misorientations, as well as 15 °-20 ° higher angle boundaries, compared to the ball with 2500 TC. In comparing the results in Figures 3.8 and 3.9, the effect of fine precipitates present without aging restricts the formation of 5-10 ° boundary misorientations, possibly due to a more homogeneous pinning effect that retards the coalescence of low angle boundaries into higher angle boundaries. The increase in the higher angle boundary misorientations during thermal cycling suggests that continuous recrystallization developed high angle boundaries from sub-grain boundaries.

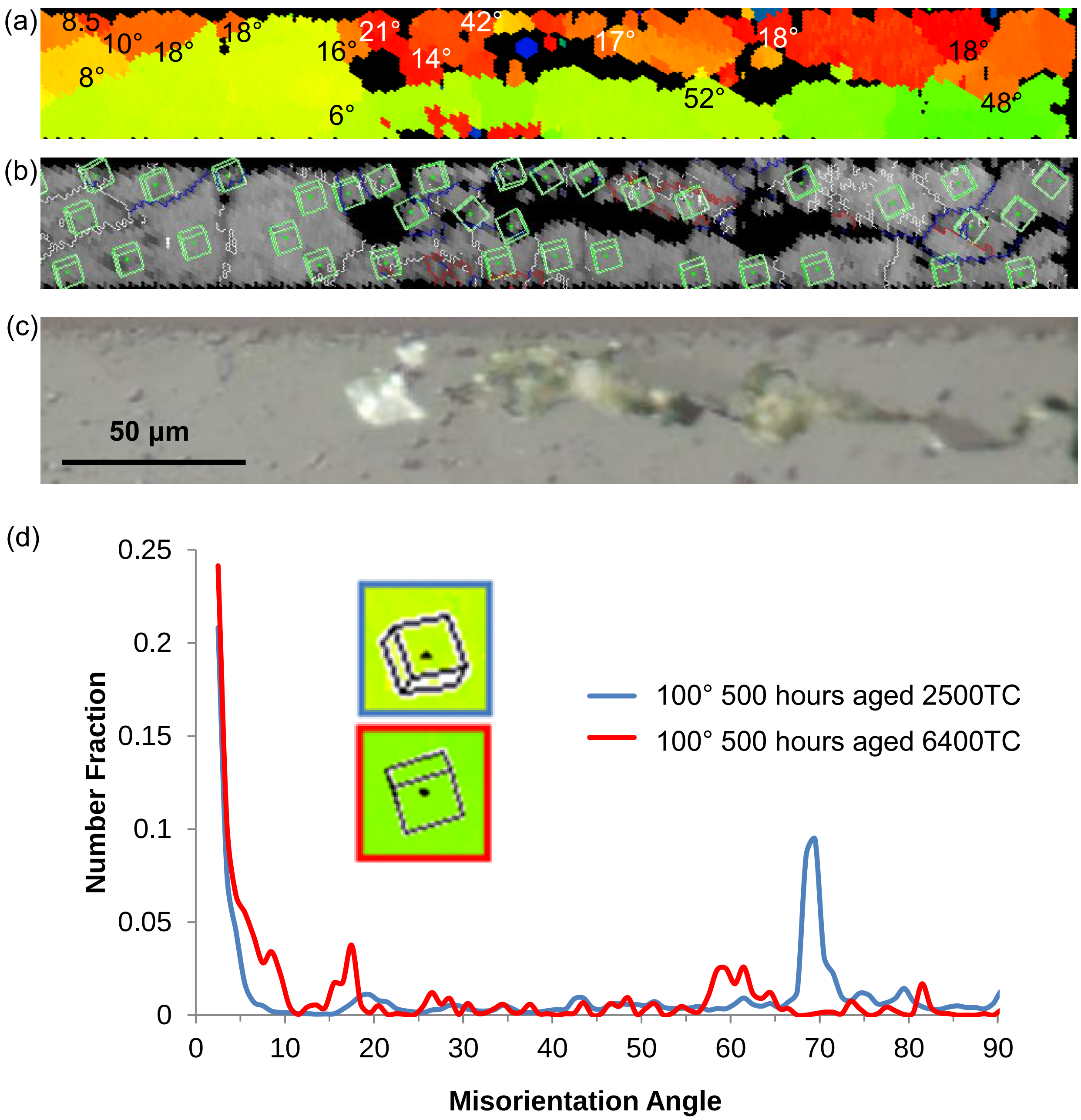

Figure 3.9 Ball 8 in the 100 ℃/500hrs+6400TC sample: (a) fine step *c*-axis EBSD map shows recrystallization and selected grain boundary misorientation angles; (b) image quality map with boundaries highlighted: white are low angle (<15 °), blue are high angle, and red are near-twin (55-65 °), and (c) PLM micrograph, where cracked regions appear light; (d) comparison of the misorientation distribution with a 2500TC sample with a similar *c*-axis orientation.

The continuous recrystallization mechanism is also reflected in a general sense in the evolution of the grain boundary misorientation distributions. The **recrystallized** grain boundary misorientations in the 2500TC (an average of 41 joints) and the 6400TC (an average of 66 joints) samples are plotted in Figure 3.10. In the same plot, the grain boundary misorientation distribution from twelve solder joints in the as-fabricated condition is also shown. In the as-fabricated condition, solder balls contain a large fraction of low angle grain boundaries and a moderate amount of twin-boundaries (55 °-65 ° misorientation). It is observed that with further straining by thermal cycling, the low angle grain boundaries and special twin-related boundaries decrease dramatically, particularly after 6400 TC. At the same time, there is a gradual increase of the higher angle boundary misorientations (between 15 °-45 °) after 2500TC and 6400TC. The statistics shown in Figure 3.10 include the recrystallized grain boundaries in the thermally cycled samples. The trend shown in the histogram thus represents the evolution of the grain boundary characteristics in the highest strained region upon thermal cycling. As described in four particular joints in Figures 3.8 and 3.9, similar phenomena such as the gradual lattice rotation and the development of higher angle misorientations from low angle boundaries during continuous recrystallization are observed. This is further supported by the statistics in Figure 3.10 where all joints with the same thermal cycling history are summarized, regardless of the pre-aging conditions.

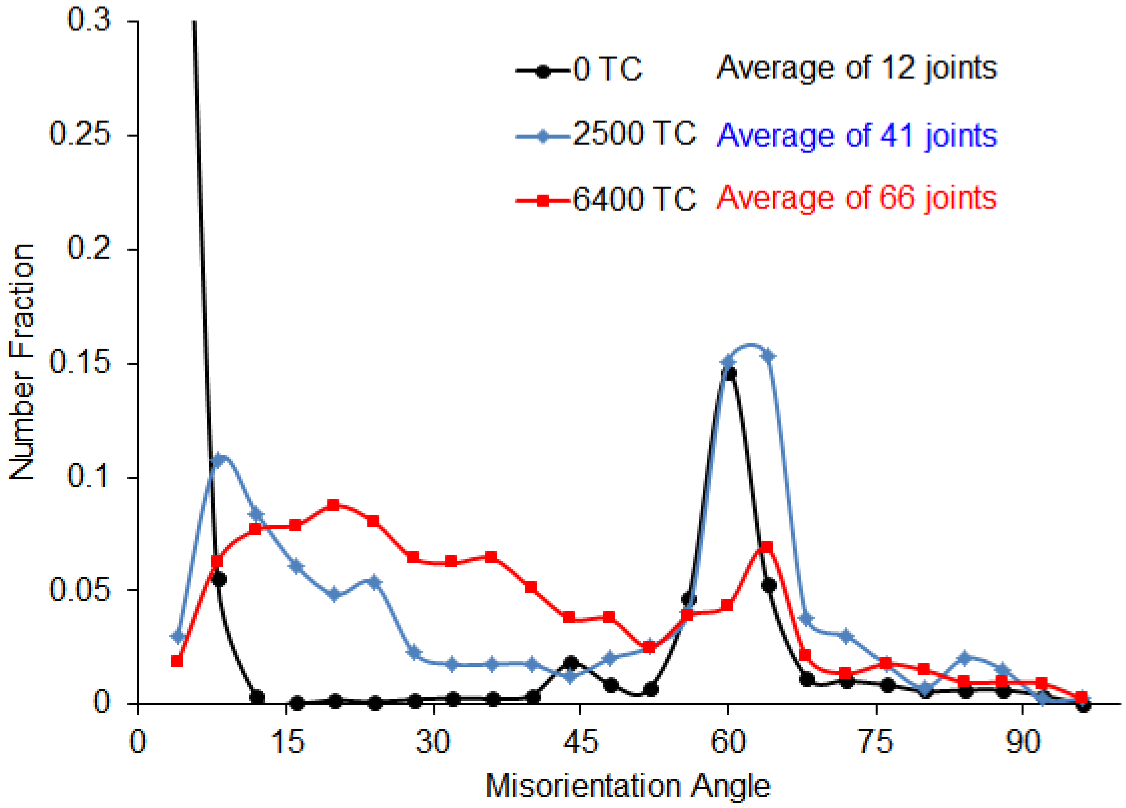

Figure 3.10 Statistics showing the grain boundary misorientation distribution from the as-fabricated condition (black), and thermally cycled samples (blue and red) in the PBGA package design.

3.5 Summary

The correlation between the Sn crystal orientation (evolution) and crack development during thermal cycling in the PBGA package design was examined in three levels. The overall distribution of Sn grain orientations in arrays of solder joints with different thermal histories was studied in plan-view using EBSD. The results suggest a mostly random distribution of dominant Sn crystal orientations in this package design. There is no significant change of the number fraction of different Sn crystal orientations in the low-strain regime (with up to 2500 TC), except for the transition from the green to yellow orientations, particularly with increasing pre-aging temperature and time. Nevertheless, after 6400 TC, a linear decrease of the purple/blue and green orientations and an increase of the yellow orientations with increased aging effects are observed. The apparent evolution of Sn crystal orientations may be a result of recrystallization. Also in the high-strain regime (6400TC), red orientation dominated in all three pre-aging conditions, suggesting that more vulnerable red orientation joints may be the product of a gradual recrystallization process from other grain orientations (e.g. green orientation).

In the second level, the dominant Sn grain orientations are correlated with cracking in the cross-section of solder joints with different pre-aging conditions. A strong correlation between the dominant red orientations and cracking is observed, and about half of the cumulative crack length is related with the dominant red Sn grain orientations. In addition to a high instance of cracking in red orientations, solder joints with dominant green and yellow orientations also cracked. Nevertheless, statistics show that the dominant green orientations are equally correlated with the cumulative length of both the cracked and intact parts of the joints. Consequently, it is fair to say that cracking is not strongly correlated with the dominant green or yellow orientations.

The next level carefully examines the recrystallization using higher spatial resolution EBSD, which indicates that substantial continuous recrystallization and some discontinuous recrystallization phenomena occurred during thermal cycling. Gradual lattice rotation to develop high angle boundaries from low angle boundaries is apparent in the EBSD orientation maps and in the grain boundary misorientation distribution histograms. With more thermal cycling, a dramatic increase of high energy high angle boundaries and a decrease of low energy low angle and twin boundaries were observed. These high angle recrystallized boundaries were effective in assisting crack propagation. It is found that cracks are also highly correlated with the red orientations developed by recrystallization. No solder joints with dominant purple/blue orientations (with Sn [001] normal to the interface) cracked.

Microstructure evolution and recrystallization preceding cracking is apparent. Cracks propagated preferably along high angle boundaries developed from the continuous or discontinuous recrystallization processes. Newly developed grains from recrystallization that are present near the crack tip may retard crack development when the crystal orientation is not favored for easy deformation (purple/blue orientation, for instance) during thermal cycling.

Chapter 4

Recrystallization and microstructure evolution in medium-strain fine-pitch BGA packages

4.1 Phenomenal characterization of microstructure evolution

As the strain per cycle increases in the medium-strain fine-pitch BGA package, the microstructural evolution in solders reflects this increase in strain energy dissipation. More dramatic recrystallization and severe cracking were observed after thermal cycling to failure in this package design. A 20% increase in resistivity was used as the failure criterion. As shown in Figure 4.1, samples from the as-fabricated, unaged+TC, and 150 ℃/500hr aged+TC conditions were examined using the PLM and EBSD. It is apparent that in the as-fabricated condition, SAC 305 lead-free solder joints tend to be either near-single crystal or tri-crystals with twinning relationships. After thermal cycling between 0 ℃ and 100 ℃ to failure, the microstructure evolution and recrystallization are readily revealed by EBSD, particularly near the chip-side interfaces. A variety of Sn grain orientations are correlated with cracking in this package. Unlike the low-strain PBGA package, even solder balls with dominant purple/blue orientations cracked after thermal cycling (Figure 4.1) in this package design, particularly after pre-aging.

Pre-aging apparently accelerated the microstructure evolution, and more dramatic recrystallization and cracking are observed after isothermal aging and thermal cycling to failure. As shown in Figure 4.1, in the unaged+TC condition, the recrystallized fine grains in solder joint are mostly observed near the chip or PWB side interface (e.g. Ball 1, 3, 4 and 5) where the CTE mismatch induced strain level is high. After pre-aging and thermal cycling, significant grain rotation and recrystallization occurred in almost all joints, along with severe cracking.

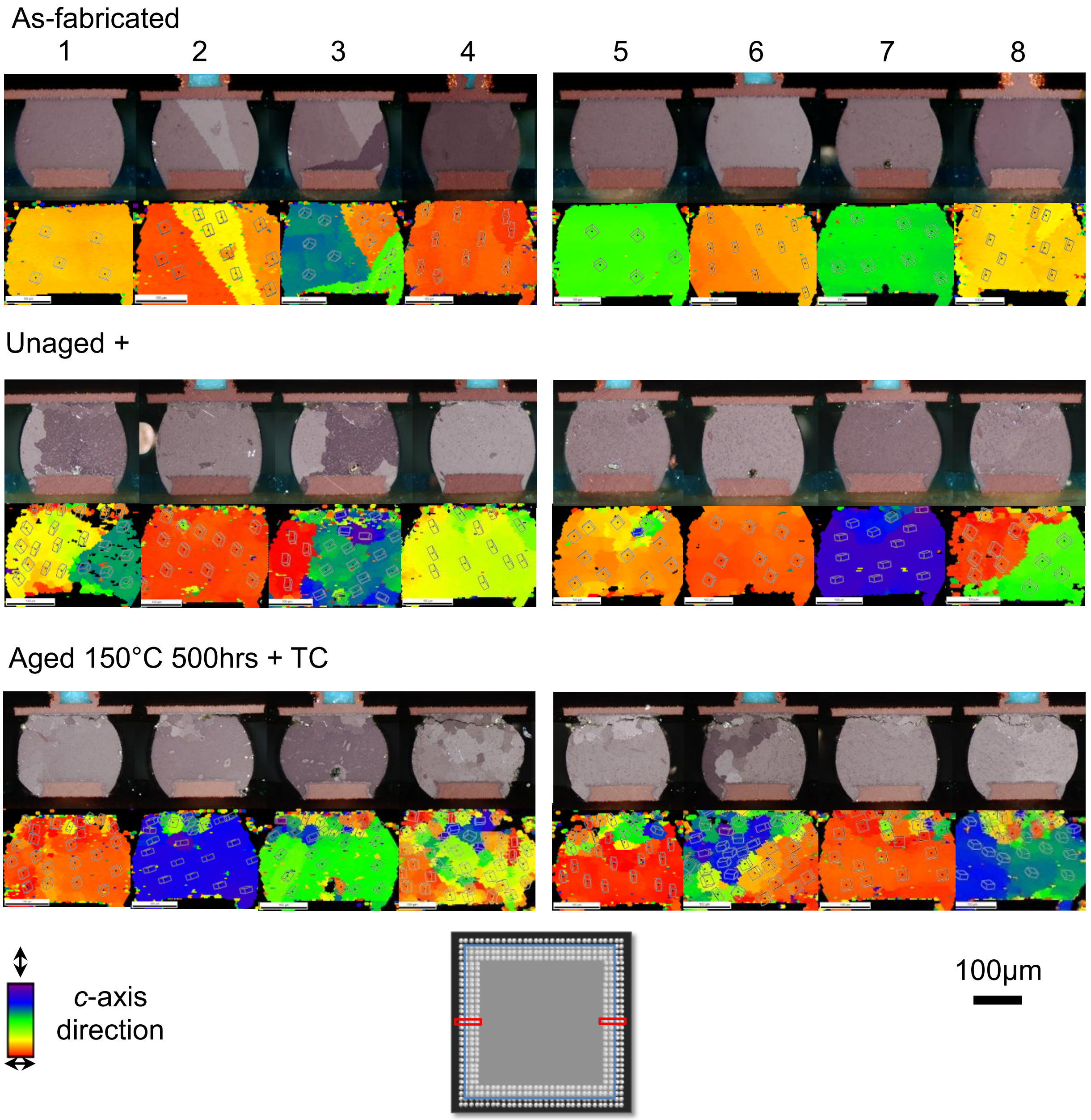

Figure 4.1 PLM micrographs (upper row) and *c*-axis EBSD maps of a row of solder joints cross-sectioned from the center of the fine-pitch BGA package in the as-fabricated, unaged+TC, and pre-aged+TC conditions; the location of the joints in the solder array is illustrated by red boxes in the inset.

In the following paragraphs, as specific case studies, microstructure evolution and its impact on the grain boundary damage and crack propagation are discussed, first in blue orientation joints. Later, a detailed characterization on the recrystallization mechanisms is examined in a particular solder ball using EBSD and DAXM (3D-XRD).

4.2 Case Study 1: Continuous recrystallization leading to grain boundary cracking

Formation of grain boundary ledges in a blue orientation joint is attributed to the continuous recrystallization process. Continuous recrystallization was accomplished by gradual lattice rotation about a Sn [110] axis. Ball 7 (Figure 4.1) of the unaged sample is shown in Figure 4.2. This solder ball has a dominant purple orientation (with Sn *c*-axis normal to the interface). A large number of low angle boundaries (black lines) are present in the bulk grain (Figure 4.2 (b)). A gradual lattice rotation evident in Figure 4.2(c) developed into high angle grain boundaries from low angle boundaries during thermal cycling. High angle grain boundaries are observed mostly near the chip side interface. After thermal cycling, blue and dark green color orientations developed at the upper right corner of the joint (Figure 4.2 (c)). Gradual lattice rotation occurred in the transition from the parent purple orientation to the blue and to the dark green orientations.

A grain boundary ledge formed along a high angle grain boundary developed during the continuous recrystallization process. Along the gradual lattice rotation, an increase of the grain boundary misorientations led to a high angle boundary near the upper right corner (blue line in Figure 4.2 (b)) where a grain boundary ledge is observed in Figure 4.2 (a). Another grain boundary ledge was formed on a low angle boundary just to the left of this. The two constitute a "U" shape grain structure which has a dark blue/green color orientation in Figure 4.2 (c). Careful examination of the optical micrograph suggests that this "U" shape ledge feature is isolated and did not cause any crack near the interface. Further development of the ledge is accomplished along a low angle boundary between the bulk purple orientation and the recrystallized blue orientation.

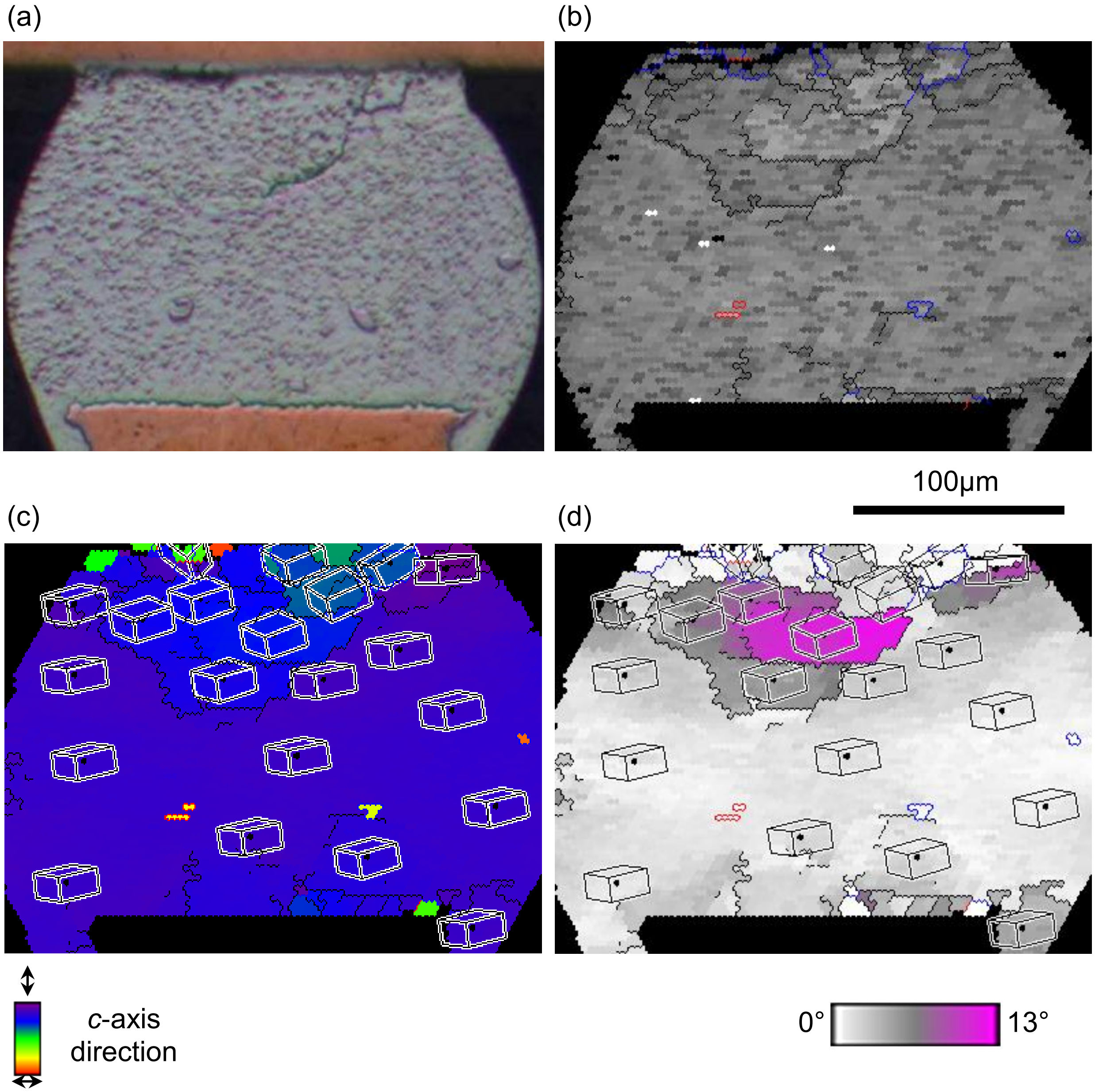

Figure 4.2 Ball #7 (in Figure 4.1) from the center row of a fine-pitch BGA package thermally cycled to failure with no pre-aging; (a) optical micrograph; (b) image quality map; (c) *c*-axis orientation map; (d) grain reference orientation deviation map (GROD) with up to 13 ° misorientation; in (b)-(d), low angle boundaries are black lines, high angle boundaries are blue lines, and twin boundaries are red lines.

Development of this grain boundary ledge was assisted by the development of local orientation gradients during continuous recrystallization. Figure 4.2 (d) shows the grain reference orientation deviation (GROD) from the average orientation. Continuous recrystallization led to a heterogeneous distribution of orientation gradients in the solder joint. For instance in Figure 4.2 (d), an orientation gradient of more than 6 ° is observed in the upper middle part of the ball where several subgrains with similar blue orientations are clustered (Figure 4.2 (c)). Among them, one large sub-grain (magenta color) exhibits the largest orientation gradient of about 13 ° from the average orientation in Figure 4.2 (d). In contrast, only a small orientation gradient (less than 2 °) is present in the bulk orientation to the right side of this sub-grain. A sharp boundary (coinciding with a sub-grain boundary) is evident between this sub-grain and its neighboring orientation. On the opposite side of this sub-grain, the orientation gradient gradually decreases towards the left side of the joint. The transition from magenta to dark grey and to light grey is smooth, which contrasts with the sharp boundary on the right side.

Heterogeneous distribution of local orientation gradients assisted the ledge development along a low angle boundary. The crystal orientation gradients reflect the extent of deformation and the presence of geometrically necessary dislocations (GNDs). It is thus likely that thermal cycling induced dislocation movement from the left toward right occurred during continuous recrystallization. A dislocation pile-up may have developed at the subgrain boundary between the magenta sub-grain and its neighboring bulk orientation, and was later absorbed into the sub-grain boundary to generate the large misorientation. Damage nucleation (in this case, development of a ledge) may thus be correlated with the difference in GND contents on two sides of the boundary. Moreover, a localized stress concentration arisen from the CTE mismatch could also accelerate the development of dislocations that further get absorbed into the sub-grain boundary and lead to a grain boundary damage site.

In addition to continuous recrystallization, features of discontinuous recrystallization are also observed near the interfaces. The discontinuous recrystallized grains are correlated with a partial crack near the upper left interface. These newly developed fine grains are highly misoriented from the bulk orientation (light green in the *c*-axis orientation map in Figure 4.2 (c)). A closer inspection of the grain boundary misorientations near these fine grains reveals that the light green orientation may be developed from continuously recrystallized purple grains by twinning. Red lines in Figure 4.2 (b) and (c) indicate boundary misorientations between 55°-65° near the upper left corner in the recrystallized region. However, this boundary has a misorientation of 64.8° about $[\bar{6}\bar{1}\bar{9}]$ (not a [100] axis), and this is not a twin boundary. The grain reference orientation deviation map suggests very low orientation gradients present in these grains, which are white in Figure 4.2 (d). The lack of orientation gradients in these recrystallized grains indicates low GND content, and they were probably formed by a primary recrystallization mechanism.

In contrast to the low-strain PBGA package, lead-free solder joints with a dominant purple/blue orientation in the medium-strain fine-pitch BGA package design cracked due to a higher effective strain per cycle. The continuous and discontinuous recrystallization processes clearly facilitated the development of grain boundary ledges and partial cracks. During thermal cycling, a large amount of sub-grain boundaries developed in the parent grain. Continuous recrystallization drives an increase of boundary misorientations to develop high angle grain boundaries from sub-grain boundaries. Grain boundary ledges are found preferentially near high angle boundaries and some sub-grain boundaries of a heavily deformed sub-grain.

In this particular solder joint, no pre-aging was applied, and the recrystallization is only observed near the chip-side interface in the vicinity of cracks and grain boundary ledges. In the bulk orientation, no dramatic recrystallization occurred. However, subgrain development clearly dominates in this region. Consequently in this case, the observed microstructure evolution away from the crack can also represent the early stage of recrystallization when sub-grain boundaries began to evolve into high angle boundaries followed by fracture development.

4.3 Case Study 2: Accelerated microstructure evolution and crack development after pre-aging and thermal cycling

With 150 ℃ pre-aging and thermal cycling to failure, sub-grain formation and recrystallization in a solder joint occurred not only near the chip-side interface, but it also progressed into the bulk material. Severe cracking was observed in Ball 8 in the 150 °500hrs aged+TC samples. Similar to Figure 4.2, the distribution of orientation gradients in this joint are heterogeneous, and an increase of local orientation gradient is observed in the middle of the ball closer to the recrystallized region.

A characteristic of the continuous recrystallization mechanism is revealed in the bulk orientation part of Ball 8 in Figure 4.3. It is observed in Figure 4.3(c) that a large amount of low-angle grain boundaries developed in the parent grain, which can be attributed to the deformation during thermal cycling. In the lower left part of the parent grain where there is nearly free of low angle boundaries, the Sn grain orientation is similar to the rest of the area in the parent grain. It is likely that, initially, this solder ball has a blue color orientation. Upon straining during thermal cycling, gradual lattice rotation across sub-grain boundaries from the blue orientation to the dark green, and to the light green orientation is apparent in the lower part of the ball. This sense of continuous lattice rotation follows a rotation axis that is close to a Sn [110] axis. From the overlaid Sn unit cells, it is observed that the misorientations between neighboring grains increase gradually towards to the lower right corner of the solder joint. Even though the light green grain is separated from neighboring grains by low angle boundaries, this grain is moderately misoriented from the parent orientation in Figure 4.3 (c). The GROD map shows a light magenta color in this grain, indicating a 15 °-16 °misorientation from the average grain orientation. The lack of high angle grain boundaries with the neighboring grains suggests that the development of this grain with large orientation gradients was accomplished by continuous recrystallization. This grain, highly misoriented from its parent orientation, is recrystallized, but recovery (absorption) of dislocations into the sub-boundaries facilitated this gradual development.

Development of a highly misoriented grain by a primary recrystallization mechanism is facilitated by a continuous recrystallization process. Near the PWB side interface, for instance, a high angle boundary (blue lines in Figure 4.3 (b)) formed from a sub-grain boundary and a recrystallized light green orientation highly misoriented from its neighboring grains is observed in Figure 4.3 (c). The GROD map indicates that this recrystallized grain is nearly free of orientation gradients. In contrast, in Figure 4.3 (d), higher orientation gradients (9° and 15°) are present in the neighboring grains on its left and right, respectively. Development of this new grain without an orientation gradient, surrounded by heavily deformed grains is evidence for a discontinuous recrystallization mechanism. Grain boundary misorientations indicate 33.8° about $[\overline{27}\;\overline{3}\;5]$(close to [100]), 37.4° about $[\overline{28}\;\overline{5}\;4]$(close to [100]), and 37.9° about[21 8 12], respectively, between this grain and the left, top, and right surrounding grains. It is speculated that development of this highly misoriented grain can be a result of a discontinuous recrystallization mechanism in which grain rotation about a Sn [100] axis drove this transition. As described earlier, the surrounding grains developed by a continuous recrystallization process, which may have facilitated the nucleation and coarsening of this grain during primary recrystallization.

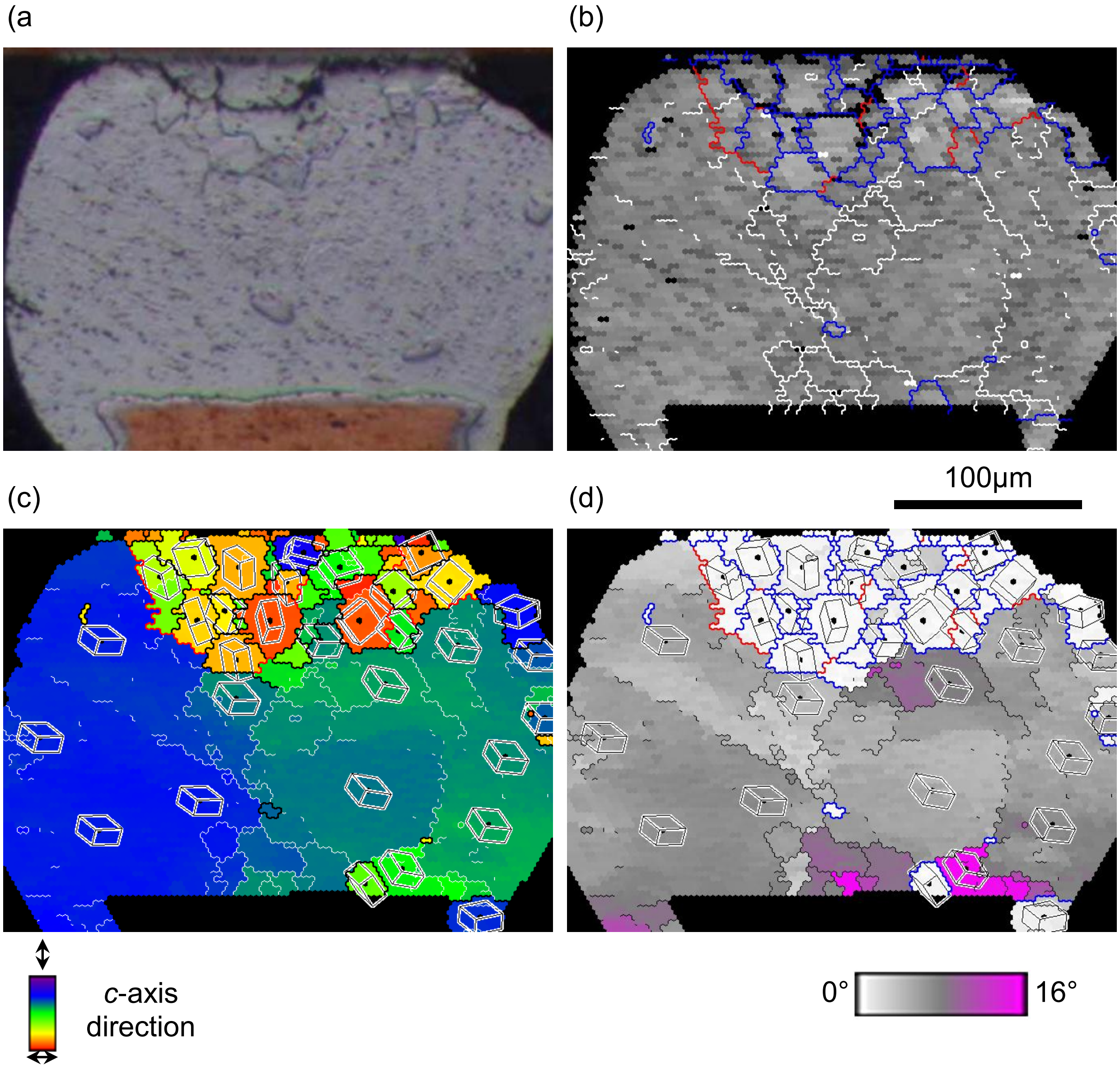

Figure 4.3 Ball #8 (in Figure 4.1) in a fine-pitch BGA package aged at 150 ℃ for 500 hours and thermally cycled to failure; (a) optical micrograph; (b) image quality map and (c) *c*-axis orientation map showing the low angle (white lines), high angle (blue lines) and twin boundaries (red lines); (d) grain reference orientation deviation map with up to 16 °misorientation, in which low angle boundaries are represented instead by black lines.

On the chip-side interface, more discontinuous recrystallization features are observed in a large area. The fine grains developed by recrystallization generated many high angle boundaries. From Figure 4.3 (d), it is clear that these high angle grain boundaries separate the solder ball into two distinct regions. Orientation gradients ranging between 3 °-8 °(grey color) spread across the solder joint in the parent orientation. This change of color from light grey to dark grey, and to magenta from the bulk orientation to the recrystallized grain, and the sharp boundary in Figure 4.3(d) indicate that dislocation accumulation may have occurred that fed the growth of the primary recrystallized grains. In the recrystallized region near the chip-side interface, however, no apparent orientation gradients are present (mostly white in the map), suggesting low GND contents. There are some low angle boundaries in this region, leading to uniform shades of gray in some grains on either side of a low angle boundary.

With a similar *c*-axis bulk orientation as the previous case, much bigger cracks are observed in this blue orientation joint after pre-aging and thermal cycling. Crack propagation is apparently facilitated by the high angle boundaries developed during the dramatic primary recrystallization. In the parent grain, the propagation of cracks follows recrystallized high angle boundaries. Interestingly, when the crack initiated at the corner and grew near the chip-side interface, a detour was taken once the crack tip reached the middle of the ball. Instead of continuing its original path, the crack headed towards the PWB side, and then turned back towards the interface again. This zigzag path is aligned well with high angle boundaries (blue lines in Figure 4.3 (b)) that developed by recrystallization.

As reviewed earlier, recrystallized boundaries may facilitate crack propagation by providing a favorable low energy path. To understand how recrystallized grains may influence crack propagation, the recrystallized grain orientations along the crack path are examined. The path of crack growth is shown in Figure 4.3 (b) and (c). Starting from upper right corner, recrystallized high angle boundaries between the orange and green orientations (distinct *c*-axis orientations) are directly correlated with the crack near the interface. Stress concentration due to CTE mismatch between two highly misoriented grains may have facilitated crack propagation into the bulk Sn. As the crack reached a recrystallized blue orientation grain, it changed direction and expanded along the grain boundary between this blue grain and its neighboring green orientation. A similar phenomenon was discussed in Figure 3.8 for a PBGA package where a blue orientation grain developed by continuous recrystallization was able to retard crack propagation completely. In this case, however, it is possible that due to the larger strain, crack propagation still proceeded, but followed an alternate route. The presence of a blue orientation may account for the first turn along the crack propagation path. Further propagation towards the PWB side was along a portion of a possible twin boundary (red line) before the crack went horizontal towards the upper left corner. In the later stage of the crack propagation, there were fewer recrystallized boundaries and larger recrystallized grains along the crack growth path. It is probable that the crack took the easiest path along these boundaries after turning away from the likely twin boundary. The contribution of grain boundary characteristics on crack propagation is discussed as follows.

Grain boundary characteristics also influence the crack propagation. For instance, a second turn along the crack propagation path was near a boundary with ~60 °misorientation. Observations in the literature suggest higher resistance to grain boundary damage in twin boundaries. Since the misorientation angle itself is not sufficient to determine whether this is a twin boundary, the rotation axis associated with this boundary is also examined. The upper portion of this near 60 °boundary that assisted crack propagation has a misorientation angle of 62 °

about the $[23\,\bar{3}\,18]$ direction (close to [101]). Clearly, this portion of the boundary does not have a [100] type of rotation axis, and thus is not a twin boundary. The lower portion of this near 60 °boundary which is beyond the crack growth path has a misorientation angle of 61.4 ° about $[5\,\overline{17}\,1]$ (close to$[0\,\bar{1}\,0]$). Therefore, the twin signature of this portion of the boundary, due to its higher resistance to boundary damage, may have contributed to the detour of the crack.

From the discussion above, it is clear that dramatic recrystallization and severe cracking were observed in a pre-aged sample after thermal cycling. Crack propagated mainly along the high angle grain boundaries. Continuous recrystallization may set up a possibility for the nucleation of a discontinuous recrystallization process. Both the Sn grain orientation and grain boundary characteristics are correlated with crack propagation. Blue grain orientations and twin boundaries are more resistant to crack development.

The recrystallization mechanisms and grain boundary properties are further examined in detail and correlated with slip activities in the following section. EBSD and DAXM (3D-XRD) were used for surface and sub-surface characterizations.

4.4 Case Study 3: Continuous recrystallization and elastic strain distribution in a solder ball with a dominant red orientation

4.4.1 EBSD characterization

The specimen examined for this case comes from a fine-pitch BGA package with a smaller Si die size. This sample was pre-aged at 100 ℃ for 500 hours before thermal cycling to failure. As shown in Figure 4.4 (a), the smaller die yields a lower strain on solder joints than the larger die configuration during deformation. Except for the die size, all other dimensions of this package are the same as the large-die package (Figure 2.1). Five solder joints near the corner of the package were prepared and examined using the optical microscopy and EBSD. Optical micrographs in Figure 4.4 (b) and (c) show the grain morphology and cracks near the chip-side interface. In Figure 4.4 (d) and (e), different grain orientations are revealed by the PLM and EBSD (see the overlaid Sn unit cells in (e)). It is noted that all five joints cracked after thermal cycling, and development of recrystallization is evident in the vicinity of the cracks.

The relative strain level in this package design is reflected by the extent of microstructure evolution. It is apparent that recrystallization in this sample is mostly confined near the chip-side interface, which is similar to the thermally cycled large-die specimen with no pre-aging. Given that these two packages have different Si die configurations, the effective strain levels on solder joints are different [Lee et al. (2011)]. Moreover, the five balls come from the corner of the small-die package, whereas in Figure 4.1, samples are cut from the middle of the package under the die area. It is thus probable that solder joints in the small-die configuration experienced a lower strain upon thermal cycling. The extent of recrystallization in this small-die pre-aged package is similar to the un-aged large-die sample, but not as dramatic as the pre-aged sample in a large-die package (Figure 4.1).

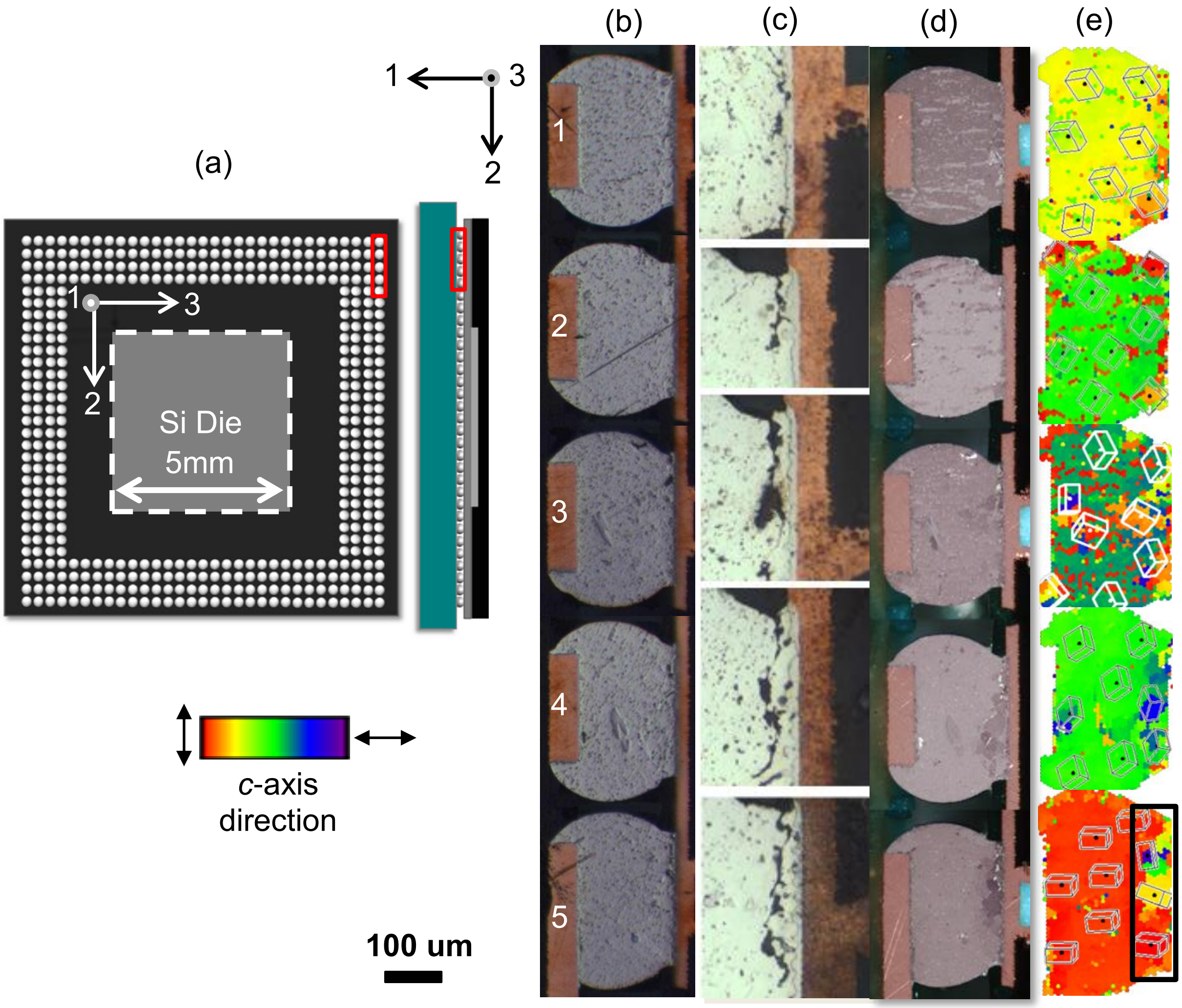

Figure 4.4 Fine-pitch BGA package with a small Si die: (a) plan-view (looking from the substrate to the chip) and cross-section view of the package; five solder joints at the outermost row are highlighted with the coordinate system for the strain tensor; (b) optical micrographs and (c) magnified optical images show cracks at the chip side in all joints; (d) PLM micrographs and (e) *c*-axis EBSD maps reveal recrystallization near the cracks. The chip-side interface region in Ball 5 (black box) is examined in detail [Zhou et al. (2012b)].

In Figure 4.4, the interface region (outlined by a black box) in Ball 5 was characterized in detail using a finer step EBSD scans, revealing both continuous and discontinuous recrystallization features which are correlated the crack development in Figure 4.5. The optical and backscatter electron micrographs show the locations of the partial cracks near the chip-side interface. A small crack on the lower corner of the joint in Figure 4.5(b) has a zigzag shape. The propagation of this crack followed high angle grain boundaries in the same region. The EBSD cleanup process filled in the cracked area in Figure 4.5 (c)-(e). Nevertheless, it is clear that the orange orientation adjacent to the crack came from recrystallization. This observation, again, suggests that the presence of recrystallized high angle boundaries facilitated crack propagation.

Grain boundaries distribute heterogeneously on the sample surface, and more high-angle grain boundaries are observed near the crack. For instance, near the upper corner in Figure 4.5, significant recrystallization occurred and the fine grains highly misoriented from the parent grain are surrounded by high angle boundaries (black line in Figure 4.5 (d)). There are fewer IMC particles in the same region near the crack, due to the observed coarsening of IMCs. The likely outcome of this is a larger spacing between IMCs, which may decrease the pinning effects on dislocations and subgrain boundaries from these particles. Greater grain boundary mobility during recrystallization is thus expected. Low angle (sub-grain) boundaries (white lines) dominate the bulk orientation further away from the cracks. In the same region, the evolution from the red orientation to orange grains by gradual lattice rotation is apparent.

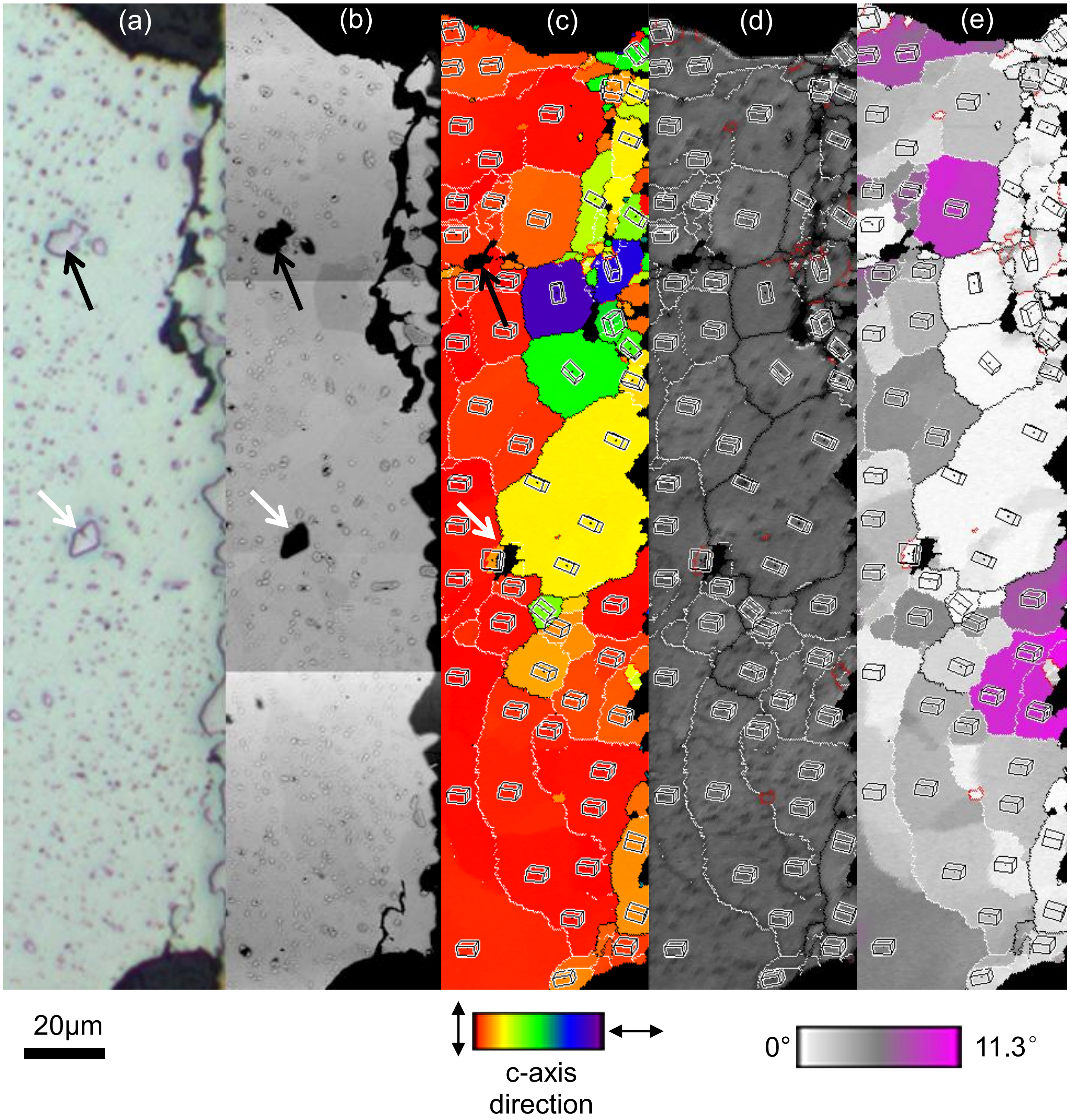

Figure 4.5 (a) Optical micrograph, (b) backscatter electron image and (c) fine-step EBSD *c*-axis orientation map showing the recrystallization and cracking; (d) image quality map; (e) GROD map showing up to 11.3 °orientation gradients; in (c)-(e), low angle boundaries are in white lines, twin boundaries in red lines, and high angle boundaries in black lines [Zhou et al. (2012b)].

A Cu_6Sn_5 particle in the middle of the joint (noted by a white arrow in Figure 4.5) is located at the boundary between the parent red orientation and a recrystallized yellow grain. Figure 4.5 (c) shows a small orange grain adjacent to the IMC particle, which has a twinning relationship with the parent grain (red line in Figure 4.5 (d)). The nucleation of a significantly different orientation in the vicinity of a hard particle indicates particle stimulated nucleation mechanism [Li et al. (2010b)]. However, it is not known whether the twin orientation was initially present near the particle, or was formed by a localized mechanical twinning process.

The heterogeneous distribution of orientation gradients is apparent in Figure 4.5 (e), and a complex sub-grain structure in the parent orientation is revealed by the GROD map. In a GROD map, the average crystal orientation in each grain is used as a reference, and the orientation deviation from the reference value up to 11.3 ° is represented by a color scale between white, grey, and magenta. In the bulk orientation, a large number of low angle boundaries are present, accompanied by greater orientation gradients that indicate how each sub-grain differs from the average orientation. The extent of orientation deviations varies in different sub-grains, and they are separated by sharp sub-grain boundaries. Gradual lattice rotation to form high angle grain boundaries from the sub-grain boundaries is a signature of the continuous recrystallization mechanism. This process is also evident in Figure 4.5 (e) where there is a gradual change of color from light grey to dark grey and to magenta color from the parent grain towards the recrystallized region. It is also revealed in Figure 4.5 (e) that the recrystallized grains in the vicinity of the crack and the grains ahead of the crack tip appear white, suggesting very low orientation gradients. This is similar to the recrystallized grains in previous cases. In the lower part of the recrystallized yellow grain, there is a diffuse band of higher local orientation gradients. Development of this band feature is correlated with slip activities, as will be discussed later.

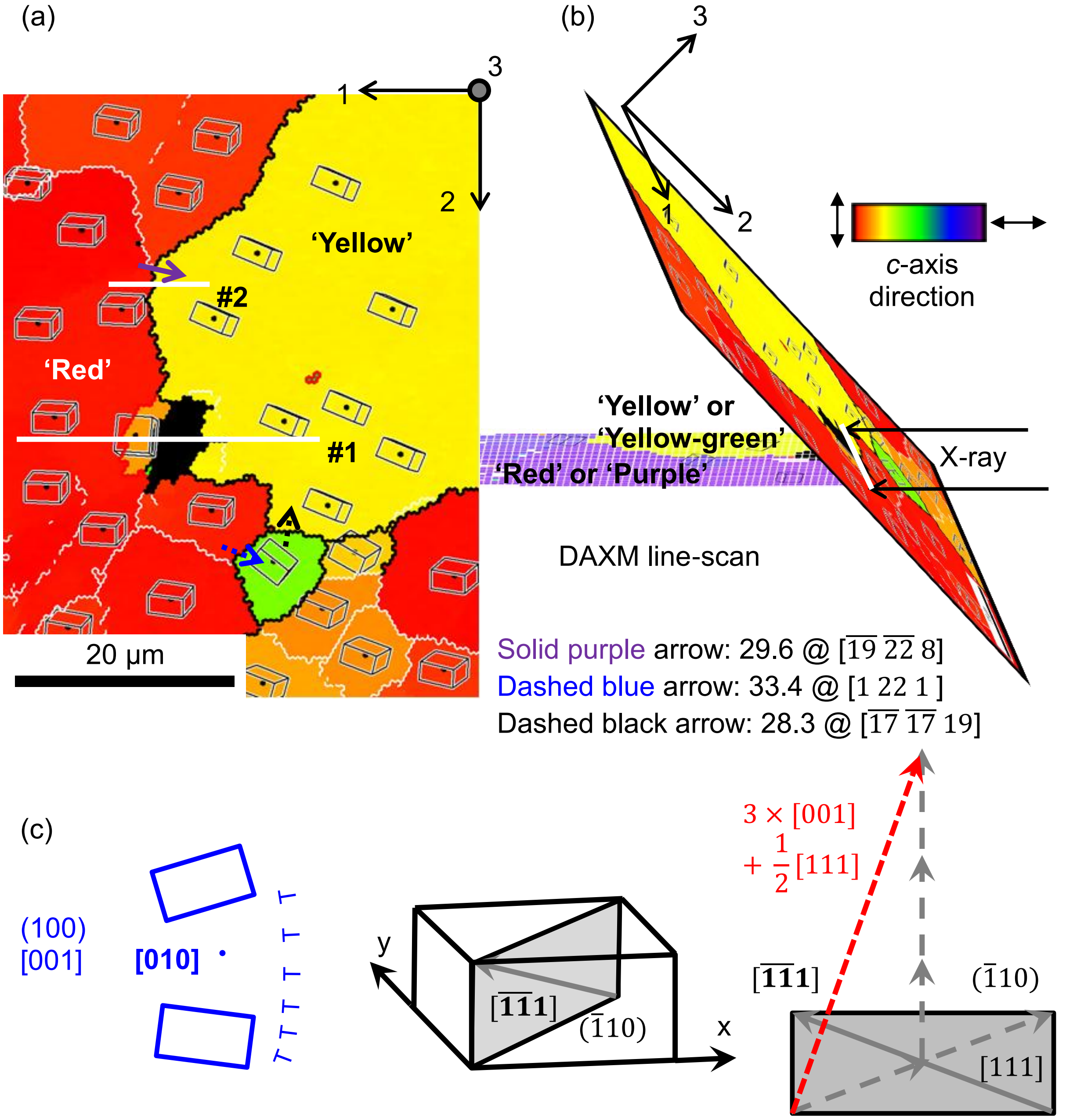

Figure 4.6 (a) *C*-axis orientation map from a fine-step EBSD scan showing two DAXM line scans (#1 and #2) across the parent and recrystallized grains; (b) a schematic showing the sampled diffraction volume beneath the sample surface and the corresponding Sn crystal orientation map (with a different color code); the coordinate system for the orientation and strain tensor is shown in the inset; the misorientation angle and rotation axes are noted for selected boundaries; (c) illustration of rotation axes related to blue and black boundary rotations [Zhou et al. (2012b)].

A more detailed study of the crystal orientation evolution in a smaller area is accomplished by a fine-step EBSD scan. The recrystallization mechanisms are discussed with regard to grain boundary misorientations in Figure 4.6 (a). A *c*-axis orientation map shows sub-grain boundaries and recrystallized high angle boundaries. Selected grain boundary misorientation angles and rotation axes are noted. These boundaries do not correspond to known low-energy configurations. Consequently, they probably are in the midst of a continuous recrystallization process, as the increase in boundary misorientations during thermal cycling leads to formation of high angle boundaries.

A primary recrystallization nucleus may have developed by a two-step lattice rotation about low-index axes by the operation of slip systems that cause such rotations. For instance, as shown in Figure 4.6 (a), the solid purple arrow across a boundary shows a 29.6 °misorientation about the $[\overline{19}\ \overline{22}\ 8]$ direction. It appears that direct formation of this recrystallized yellow orientation grain from the parent red orientation may not be easily accomplished by a slip-recovery process. However, as shown in the lower part of Figure 4.6, by adopting a two-step rotation about low-index axes, this transition from red to yellow orientations may be accomplished via the intermediate green orientation. This transition proceeded first along the dashed blue arrow around the $[1\ 22\ 1]$ (close to $[0\ 1\ 0]$) axis, followed by (or perhaps simultaneously with) the dashed black arrow about the $[\overline{17}\ \overline{17}\ 19]$ (close to $[\bar{1}\ \bar{1}\ 1]$) axis. Both of these can be accomplished by the operation of known facile slip systems. Considering edge dislocations, the lattice rotation (due to dislocation slip) is about an axis on the slip plane and normal to the slip direction. Specifically, a rotation about [010] axis is attributed to slip on the (100)[001] slip system (SS#1). Similarly, the operation of slip on two facile coplanar slip systems, $(1\bar{1}0)[111]$ (slip system #4) and three times as much on $(1\bar{1}0)[001]$ (slip system #2) would lead to a resultant slip direction along the red dashed line in Figure 4.6(c). The rotation axis, determined by the slip plane normal and the slip direction, is $[\bar{1}\bar{1}1]$, which matches with the boundary misorientation pointed by the purple arrow.

Similar to a bigger area, heterogeneous distribution of local orientation gradients is evident in a smaller area in Figure 4.7. Much larger orientation gradients are present in the parent orientation in Figure 4.7 (a), and the majority of sub-grains in the parent orientation have larger than 2 ° orientation gradients. In some subgrains, the local orientation gradient is as high as 6 °. The dramatic difference in the orientation gradient distribution in the parent orientation suggests a complex sub-grain structure developed by gradual lattice rotation. Depending on the local stress state, deformation in some sub-grains may have occurred more than others. The parent orientation gradients are also reflected in the pole figures. As shown in Figure 4.7(c), (001), (100), and (010) poles for the parent and recrystallized grains are overlaid. In the parent grain, the (001) and (010) poles are broader and split. However, the corresponding peaks are sharp in the recrystallized grains, which are also shown as white or light grey colors in Figure 4.7 (a), indicating that these grains are nearly free of orientation gradients.

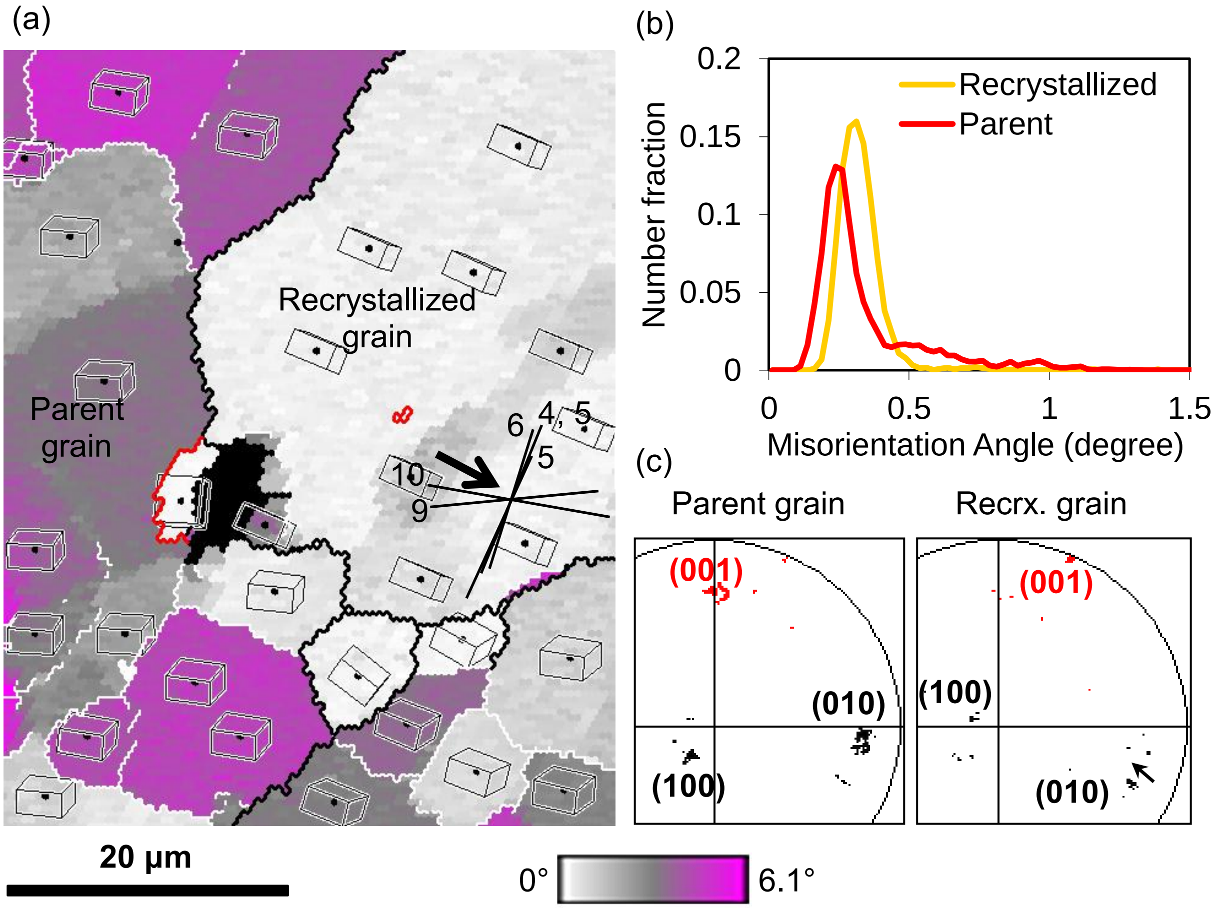

Figure 4.7 (a) GROD map showing up to 6.1 °misorientation; slip traces of slip systems with highest Schmid factors are shown; black arrow marks a sub-grain boundary; low angle, high angle, and twin boundaries are labeled with white, black, and red lines, respectively; (b) local average misorientation (LAM) histogram and (c) overlaid 001 and 100 pole figures of the parent orientation and the recrystallized yellow grain [Zhou et al. (2012b)].

The local average misorientation distribution histogram (LAM) in Figure 4.7 (b) reflects the spread of Sn crystal orientations locally due to the presence of GNDs. Relatively sharp peaks are observed for both the parent and recrystallized grains, suggesting low GND contents. The apparent broadening of the red curve with a shoulder near the 0.5 ° misorientation indicates a bi-modal population in the parent grain. In contrast, the orange curve from the recrystallized grain is relatively smooth and symmetric to the peak center, suggesting low orientation gradients and internal elastic strain.

Interestingly, the shift of the LAM distribution to a larger value in the recrystallized grain is likely attributed to the development of a dark grey band-like structure within the recrystallized grain in Figure 4.7 (a). Closer inspection of this structure reveals a less than 2 ° misorientation from the average orientation. On the lower-right side of the band, the extent of orientation gradients changes gradually. In contrast, the band is sharper on the opposite side of the boundary. This band-feature is present within a recrystallized grain developed during thermal cycling. Localized strain variations may lead to a subsequent heterogeneous deformation along this grey band, suggesting that this band-like sub-grain structure may be an active shear band within a newly recrystallized grain.

The difference in orientation gradients on two opposite side of the band indicates that formation of this structure may be related to dislocation activities associated with slip, and a dislocation pile-up along the sharper upper-left sub-grain boundary is likely. In order to correlate the development of local orientation gradients with dislocation slip activities, Schmid factors (*m*) of all 32 possible slip systems in Sn grouped into ten families (Table 1.2) are calculated using an estimate of the global stress state. As described section 2.4 in Chapter 2, it is assumed that the shear stress due to the CTE mismatch dominates during thermal cycling. The sense of shear is parallel to the chip-side interface in the direction from the solder joint to the package center, which is about 36.2 ° from the sample surface normal direction. The slip plane (***n***), slip direction (***b***), and the corresponding lattice rotation axis (RA) for both edge and screw dislocations of slip systems with highest Schmid factors (greater than 0.42) are listed in Table 4.1. Active Sn slip systems responsible for the development of this band-like feagure can thus be estimated.

Active slip systems can first be estimated based on the calculated Schmid factor and the slip traces. It is observed that one slip system in slip system #10 has the highest Schmid factor, followed by slip systems #4, #9, #6, and #5. The plane traces of these slip systems are drawn on Figure 4.7 (a). Traces of slip systems #4, #5, and #6 are aligned with the grey shear band, but those of slip systems # 9 and 10 are not. Consequently, slip systems #4, #5, and #6 may be active. Further confirmation of the active slip systems estimated by the Schmid factor and slip traces was accomplished by comparing the rotation axes associated with these slip systems with the EBSD result. It is revealed by EBSD that, along the black arrow at the band-like sub-grain structure, there is a misorientation of 1.7 ° about a $[\bar{1}\ 1\ 6]$ axis (close to [001]). This rotation about the Sn [001] direction (*c*-axis) is also revealed the pole figure in Figure 4.7 (c), where all peaks are sharp in the recrystallized grain pole figures except the (010) peak, which is elongated about the (001) pole. The sense of lattice rotation about a [001] axis is marked by a black arrow in the pole figure.

Table 4.1 Slip systems (SS) with highest Schmid factors (*m*) and corresponding rotation axes (RA) for edge (bold) or screw (normal font) dislocations [Zhou et al. (2012b)]

SS	**# 10**	**#4**	**#9**	**#6**	**#5**	**#5**
n & **b**	$(\bar{1}21)[101]$	$(110)[\bar{1}11]$	$(10\bar{1})[101]$	$(010)[101]$	$(110)[1\bar{1}0]$	$(1\bar{1}0)[110]$
m	0.656	0.520	0.466	0.462	0.421	0.421
RA	~$[\mathbf{\bar{1}\,\bar{2}\,4}]$ ~$[\bar{1}23]$	~$[\mathbf{\bar{1}1\bar{7}}]$ $[110]$	~$[\mathbf{010}]$ ~$[10\bar{3}]$	~$[\mathbf{\bar{1}03}]$ $[010]$	~$[\mathbf{001}]$ $[110]$	~$[\mathbf{00\bar{1}}]$ $[1\bar{1}0]$

The rotation axes associated with each slip system is determined by the slip plane normal and the slip direction. In order to form a sub-grain tilt boundary with edge dislocations by simple lattice rotation about the [001] axis, ⟨010], ⟨111], or ⟨110] dislocations should be mobile on {100) or {110)planes. It is thus inferred that operation of slip systems #4 and 5 are able to cause this type of lattice rotation, assuming edge dislocation motion in these slip systems. For screw dislocations, for a given slip system, the rotation axis is parallel to the slip plane normal. Consequently, screw dislocations with burgers vector ⟨100], or ⟨110] on {001) planes (slip systems #7 and #8) may have a similar contribution to lattice rotations as edge dislocations of slip systems #4 and #5. However, in this case, neither slip systems #7 or #8 has a high Schmid factor. Consequently, to satisfy all three criteria (*m*, RA, and the slip trace), edge dislocations in slip systems #4 and #5 (which are relatively facile as suggested in section 1.3 in Chapter 1) are most like to have been mobile, and responsible for the formation of this band-like sub-grain structure. Nevertheless, Schmid factors calculated using the global stress state may not be representative of the local stress state, and thus the relative activity of different slip systems may vary from the condition estimated from the global Schmid factors.

4.4.2 DAXM characterization

In order to acquire detailed Sn crystal orientation and residual elastic strain information beneath the sample surface, DAXM was used for non-destructive assessments. Two DAXM surface line scans were made, as illustrated by two white lines in Figure 4.6 (a). The longer line of 27μm went across the center of the Cu_6Sn_5 particle, covering the parent red, the small orange twin grain, IMC, and the recrystallized yellow orientation. The other portion of the same recrystallized grain boundary between the red and yellow grains was examined by a shorter line (17 μm) scan. The sampled space is shown in Figure 4.6 (b), with the corresponding DAXM orientation map. The coordinate systems used for the DAXM orientation and the internal strain calculation is the same as the one used for the EBSD based analysis, and are indicated in Figure 4.6. As discussed earlier, the off-diagonal deviatoric strain tensor components can be determined from the DAXM scan. Therefore, in the current coordinate system, the shear strains due to the maximum CTE mismatch at the package scale are represented by a combination of ε_{12} and ε_{13}. At the same time, during thermal cycling, the differential CTE normal to the interfaces contributes normal strain in the "*1*" direction, and is thus represented by ε_{11}.

The Sn crystal orientations in the DAXM orientation map are represented by the sample normal inverse pole figure key, as displayed in the inset in Figure 4.8. For this particular color code, white in the center of the sphere is the reference color, and Figure 4.8 is drawn accordingly. In order to examine small orientation gradients, "white" can be assigned to any orientation, and the radius of the new color sphere corresponds to the deviation from the reference color. Consequently, the local orientation gradient is illustrated by different colors in Figure 4.9 (a).

Surface Sn grain orientations obtained by EBSD and the subsurface orientations from DAXM can be correlated. In Figure 4.8, it is apparent that the purple orientation corresponds to the parent red orientation in Figure 4.6. The recrystallized yellow orientation is shown as “Yellow-Green”. The small twin orientation is pink. The Cu_6Sn_5 phase is manually indexed and painted black in the orientation map. Two more orientations are revealed beneath the surface, and they are noted as “Blue 1” and “Blue 2” orientations in Figure 4.8. Since these two orientations are not visible from the EBSD scans on the sample surface, they provide additional information regarding crystal orientation evolution. Sn and Cu_6Sn_5 unit cells are overlaid at corresponding voxels (black dot in the prism) on the DAXM orientation maps. Laue patterns at these voxels are shown in Figures 4.10-4.15.

Grain boundary misorientation relationships between the parent and the recrystallized Sn grains are analyzed, as listed Table 4.2. It is suggested that no grain boundary misorientation is correlated with any known special boundary in Sn, except the twin relation between the parent purple and the small pink grain. Nevertheless, the rotation axis from the “Blue1” grain to the “Yellow-Green” orientation is$[2\ 16\ \bar{1}]$, which is close to the Sn [010] (*a*-axis). In contrast, a rotation of 30 °about $[14\ 17\ \bar{6}]$ is required in order to develop the “Yellow-Green” orientation *directly* from the parent purple orientation. Similar to the discussion of Figure 4.6 regarding the intermediate green grain, it is likely that recrystallization may have occurred by two steps of independent rotation processes 1) rotation from the parent purple grain to the “Blue 1” via a lower angle boundary about $[1\ \overline{16}\ 13]$ (close to $[0\ \bar{1}\ 1]$) axis; and 2) rotation from “Blue 1” to “Yellow” around an *a*-axis. However, a slip activity analysis similar to that discussed above suggests that there is no slip system with a high global Schmid factor to cause these rotations. It is thus inferred that larger angle rotations (16 ° and 22 °) may not be accomplished by a single dominant slip system.

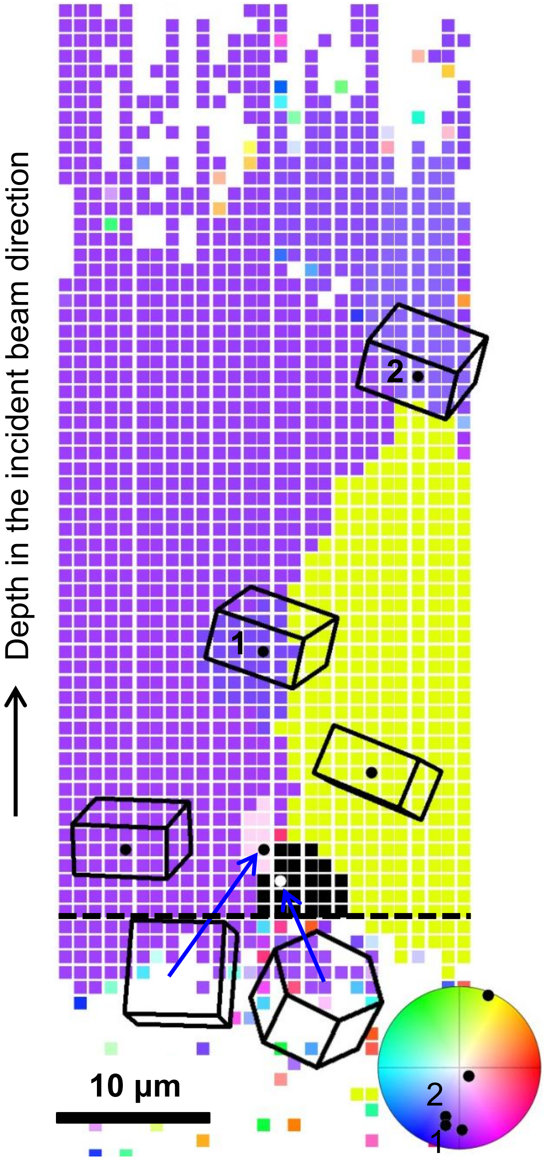

Figure 4.8 DAXM sub-surface orientation map colored with the inverse pole figure color sphere of line scan #1; crystal orientation of selected voxels of the Sn and Cu_6Sn_5 phases are shown as overlaid unit cells (and they are also labeled on the ipf colored sphere) [Zhou et al. (2012b)].

Table 4.2 Euler angles of different Sn crystal orientations (on diagonal) and their misorientation relationships (misorientation angles in degrees and rotation axis) [Zhou et al. (2012b)].

	Purple	**Yellow/Green**	**Blue 1**	**Blue 2**	**Pink**
Purple	**(272, 74, 166)**	30@ $[14\ 17\ \bar{6}]$	16.4@ $[1\ \overline{16}\ 13]$	19.1@ $[14\ 6\ \bar{5}]$	**61.9@[30 0 1]**
Yellow/ Green		**(247, 92, 254)**	22.4@ $[2\ 16\ \bar{1}]$	30.2@ $[1\ 28\ \overline{10}]$	86.9@ $[21\ 4\ \bar{7}]$
Blue 1			**(256, 71, 73)**	9.2@ $[\bar{7}\ 19\ 20]$	64.8@ $[18\ \bar{3}\ 8]$
Blue 2				**(255, 63, 78)**	57.2@ $[27\ \bar{7}\ 12]$
Pink					**(316, 18, 131)**

The elastic strain beneath the sample surface is revealed by the DAXM, and the shear and normal strain tensor components for each voxel are plotted in Figure 4.9 (b)-(d). Since the calculation of elastic strain was performed on the Sn phase only, the region where the Cu_6Sn_5 particle is present was shaded in dark grey. In order to differentiate high angle grain boundaries from sub-grain boundaries, solid and dashed lines are used to label the boundaries, respectively. During thermal cycling, the shear strain at the solder/package interface is thus represented by a combination of ε_{12} and ε_{13} (Figure 4.9 (b) and (c)), as described earlier.

It is shown in the strain map that the heterogeneous distribution of the residual strain varies in different Sn crystal orientations, as well as in sub-grains. In Figure 4.9 (a), it is noted that, in the recrystallized grains (light and yellow green), the values of both shear and normal strain tensor components are low. The light green orientation (which corresponds to the yellow-green orientation in Figure 4.8), for instance, is nearly free of shear and normal strains (ε_{12} and ε_{11}). As described in section 1.4.3 in Chapter 1, the hydrostatic strain tensor component in the full strain tensor are not determined by the automatic post-processing, although the relative value can be related via the parameter Δ. A residual ε_{13} shear strain of about 0.1% is distributed uniformly in this grain. Consequently, the total shear strain (represented by a combination of ε_{12} and ε_{13} with the direction of shear closer to the "13" component) still has a near-zero value. In contrast, much higher shear and normal strains are found elsewhere.

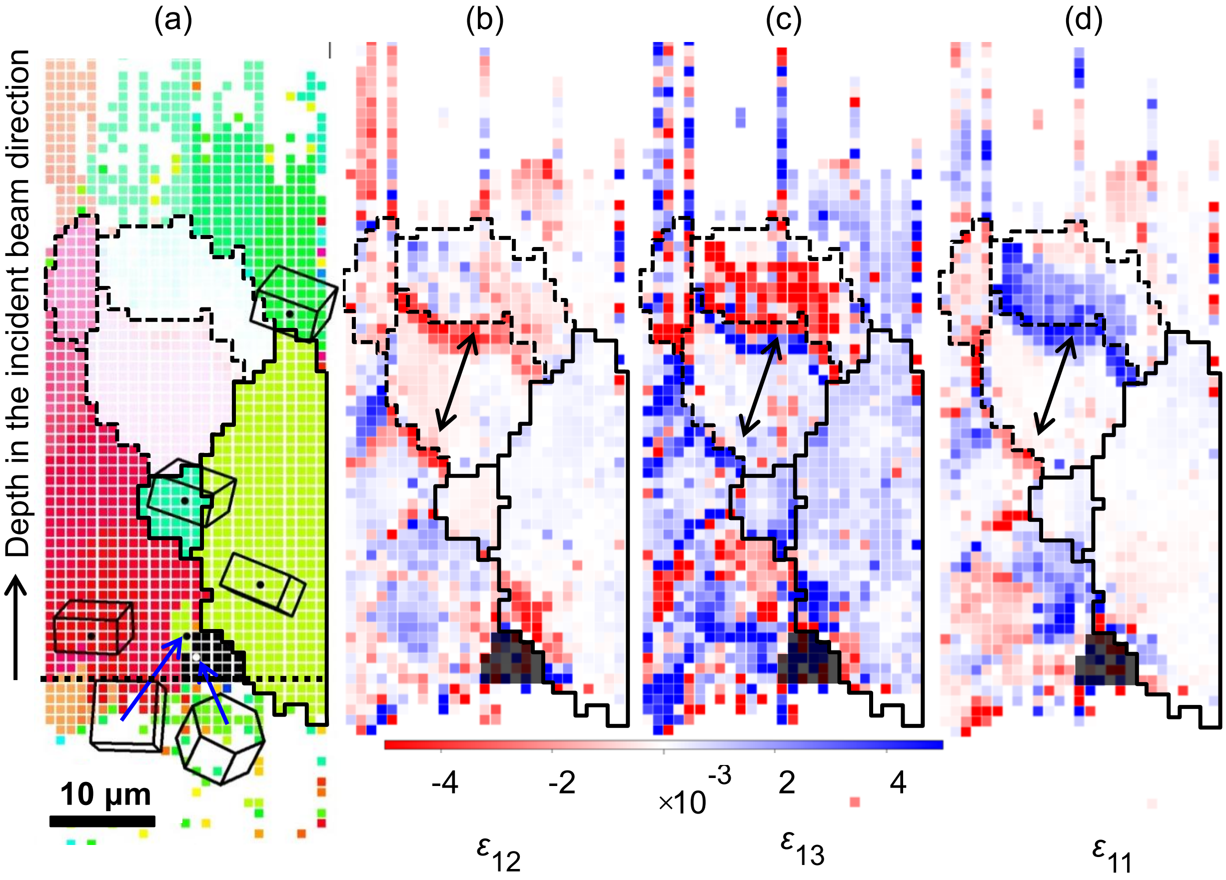

Figure 4.9 (a) Sn and Cu_6Sn_5 unit cells, overlaid on an inverse pole figure showing a 3 ° misorientation spread (white as the reference orientation), and grain boundaries between the parent and recrystallized grains are highlighted; polished sample surface is approximately along the black dotted line; components of the deviatoric strain tensor in the Sn phase are plotted in (b)-(d) using the coordinate system shown in Figure 4.6 [Zhou et al. (2012b)].

Local strain concentrations appear mostly along sub-grain and/or grain boundaries. Figure 4.9 (a) is plotted to show up to a 3 °misorientation spread, which clearly reveals local orientation gradients. Comparing this map with Figure 4.9 (b)-(d), it is clear that high shear and normal strains are observed near the subgrain boundaries. The distribution of residual strain also varies in different sub-grains. For instance, the light pink grain in the center of the orientation map in Figure 4.9 (a) has a similar strain level as the recrystallized grains, and is nearly free of shear and normal strain. Its neighboring white grain, however, has a shear strain component ε_{13} of greater than -0.4% and a normal strain component ε_{11} of about 0.2%. The maximum residual strain is distributed mostly along the sub-grain boundaries between these two neighboring grains. The DAXM orientation map suggests only minor misorientations between these two sub-grains, and yet the strain distribution is dramatically different. It is thus likely that the strain concentration induced by the thermal strain is correlated with dislocation accumulations at or near grain or sub-grain boundaries, which causes locally high stress states.

Elastic strain concentration at the sub-grain or grain boundaries can be correlated with the recrystallization mechanism. These sub-grain boundaries may increase in misorientation during deformation and with greater defect density, gain mobility. With a higher misorientation, the sub-grain boundaries are able to move into the neighboring grains and sub-grains, leaving behind a more perfect crystal. Moreover, due to the high homologous temperature in Sn, recovery process may also stimulate the absorption of dislocations into grain or sub-grain boundaries, and thus reduce the high local strain concentration at these locations. Interestingly, Laue microdiffraction patterns shown in Figures 4.10-4.15 exhibit no apparent streak in the Sn peaks, indicating very low GND content within the 1μm^3 voxel, which implies that dislocations are readily absorbed into the boundaries. Comparison between Laue microdiffraction patterns from the parent and recrystallized grain reveals no dramatic difference in the shape of diffraction peaks. This confirms the above hypothesis that GNDs generated by the heterogeneous strain are efficiently absorbed at the sub-grain boundaries, leaving very few un-paired dislocations in the lattice.

Similar phenomena are observed in the DAXM orientation map and the corresponding elastic strain maps of the second surface line-scan in Figure 4.16. The dominant purple grain in Figure 4.16 (a) corresponds to the same parent red orientation in Figure 4.6. Heterogeneous strain distribution is also evident in Figure 4.16 (c)-(e), and strain concentration in some sub-grains are illustrated by a pair of arrows in Figure 4.16 (b)-(e). However, the lack of complex sub-grain structures and IMC particles may account for a relatively lower strain values in this scan as compared to the other one in Figure 4.9.

In addition to the phenomenon of continuous recrystallization, development of local orientation gradients and sub-grains are also observed in these two surface line scans. This process may be considered as a nucleation process for primary recrystallization. Continuous recrystallization, which involves local lattice rotation, is directly correlated with slip and dislocation activities. This process sets up the possibility for an oriented primary recrystallization nucleus in the strain concentrated areas. GROD maps from EBSD and internal strain distribution obtained using DAXM strongly support this mechanism. The dramatic difference in the recrystallization behaviors across the sample in this joint indicates that any form of recrystallization may occur locally, and the details depend on the strain distribution and the evolution of locally activated slip systems.

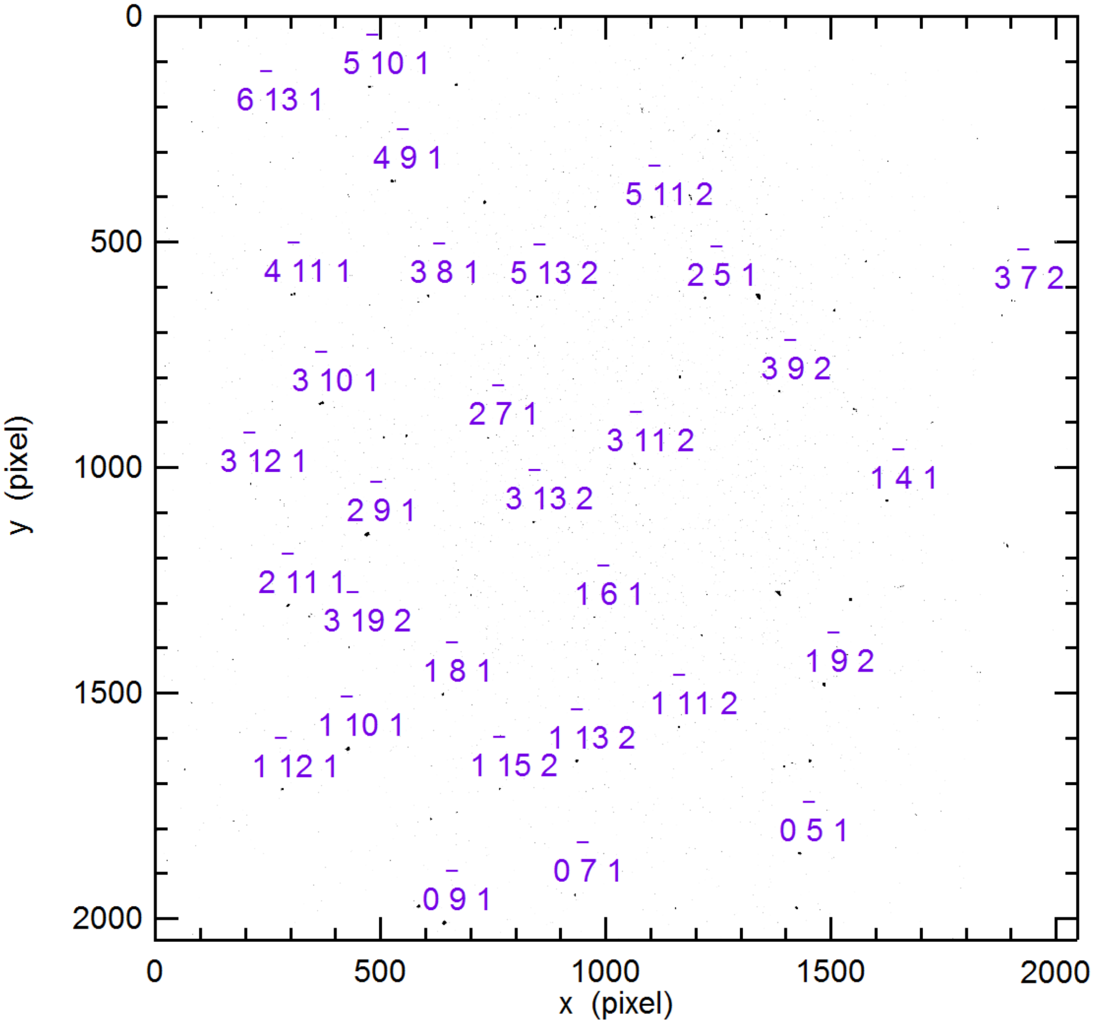

Figure 4.10 Laue microdiffraction pattern from a 1μm^3 voxel illustrated by the overlaid Sn unit cell in the parent purple orientation in Figure 4.8 [Zhou et al. (2012b)].

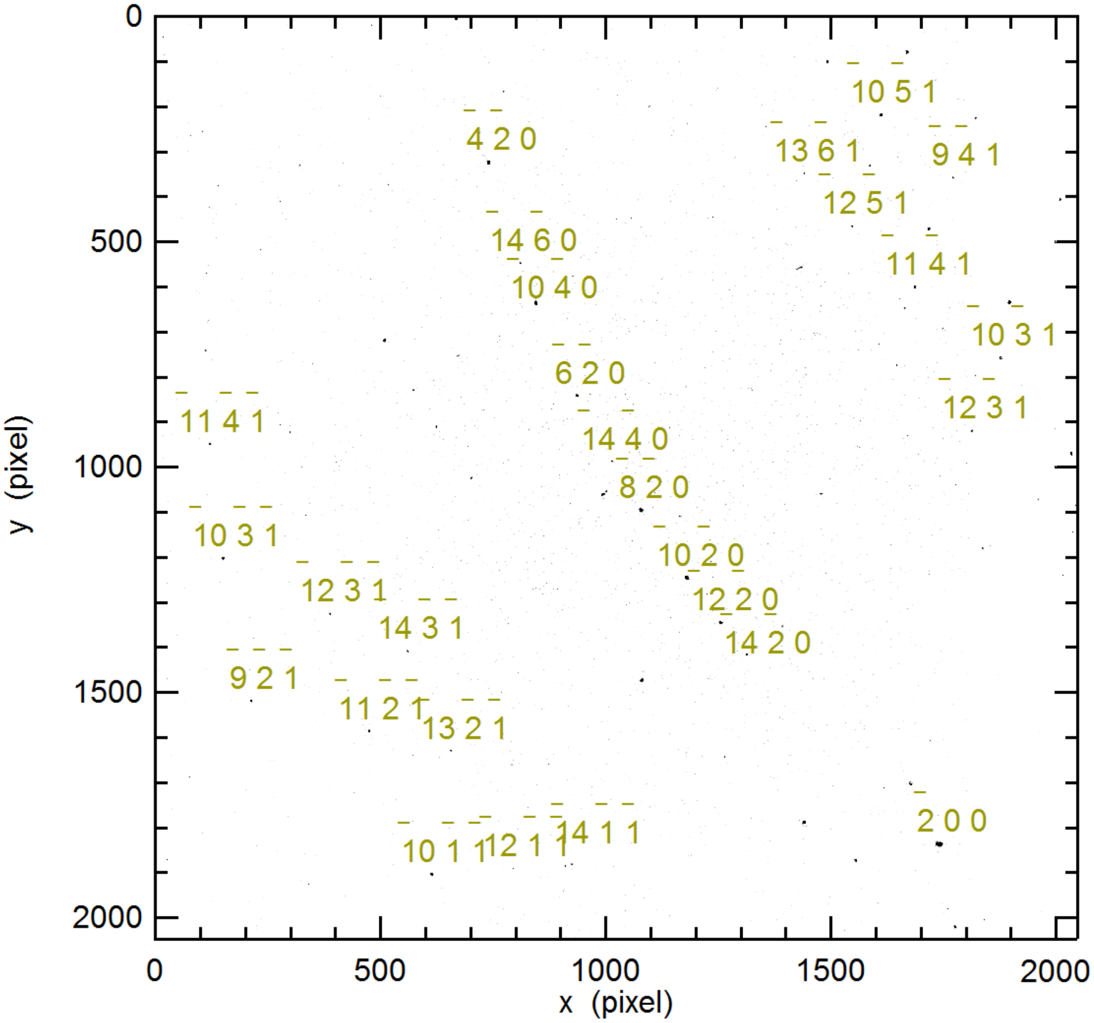

Figure 4.11 Laue microdiffraction pattern from a 1μm^3 voxel illustrated by the overlaid Sn unit cell in the recrystallized yellow-green orientation in Figure 4.8 [Zhou et al. (2012b)].

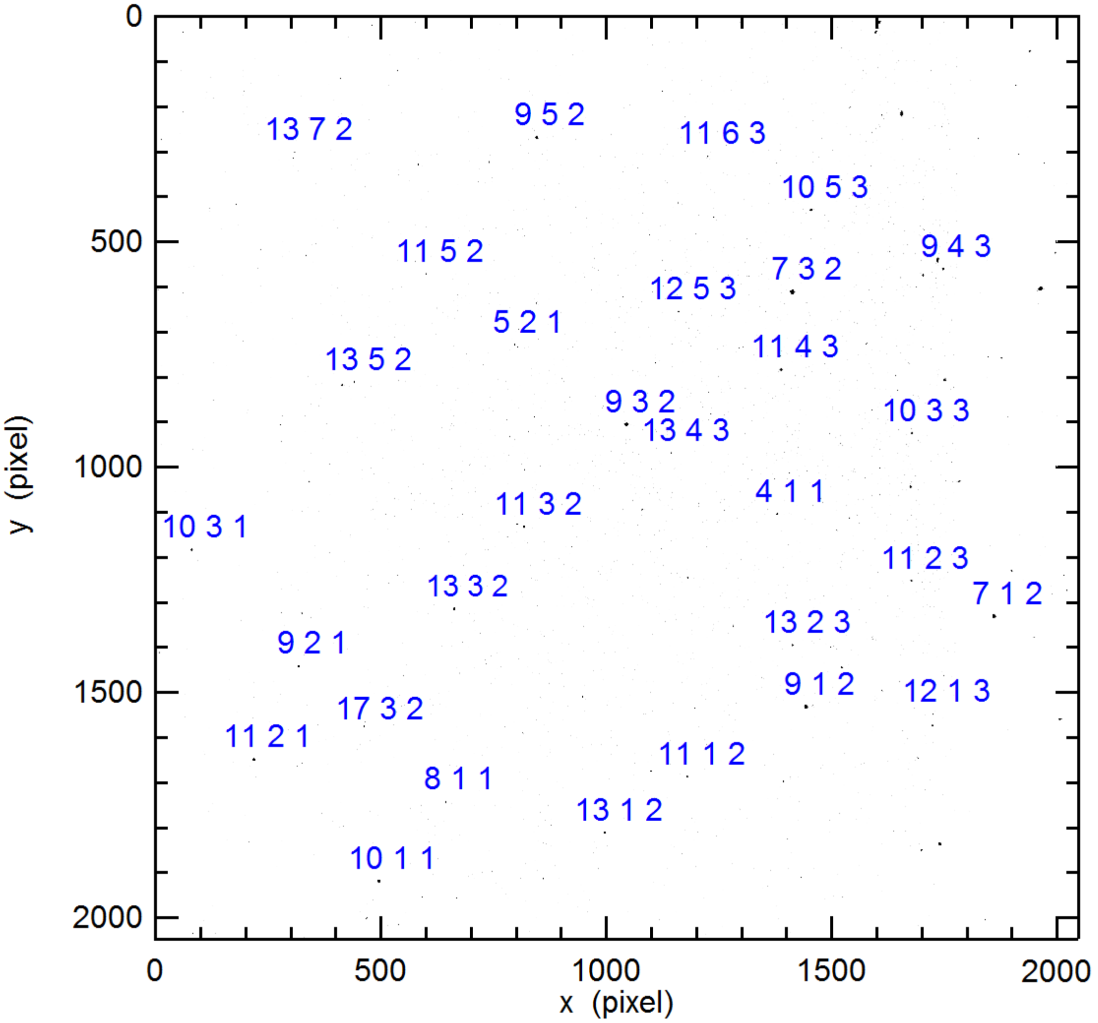

Figure 4.12 Laue microdiffraction pattern from a 1μm^3 voxel illustrated by the overlaid Sn unit cell in the recrystallized "Blue 1" orientation in Figure 4.8 [Zhou et al. (2012b)].

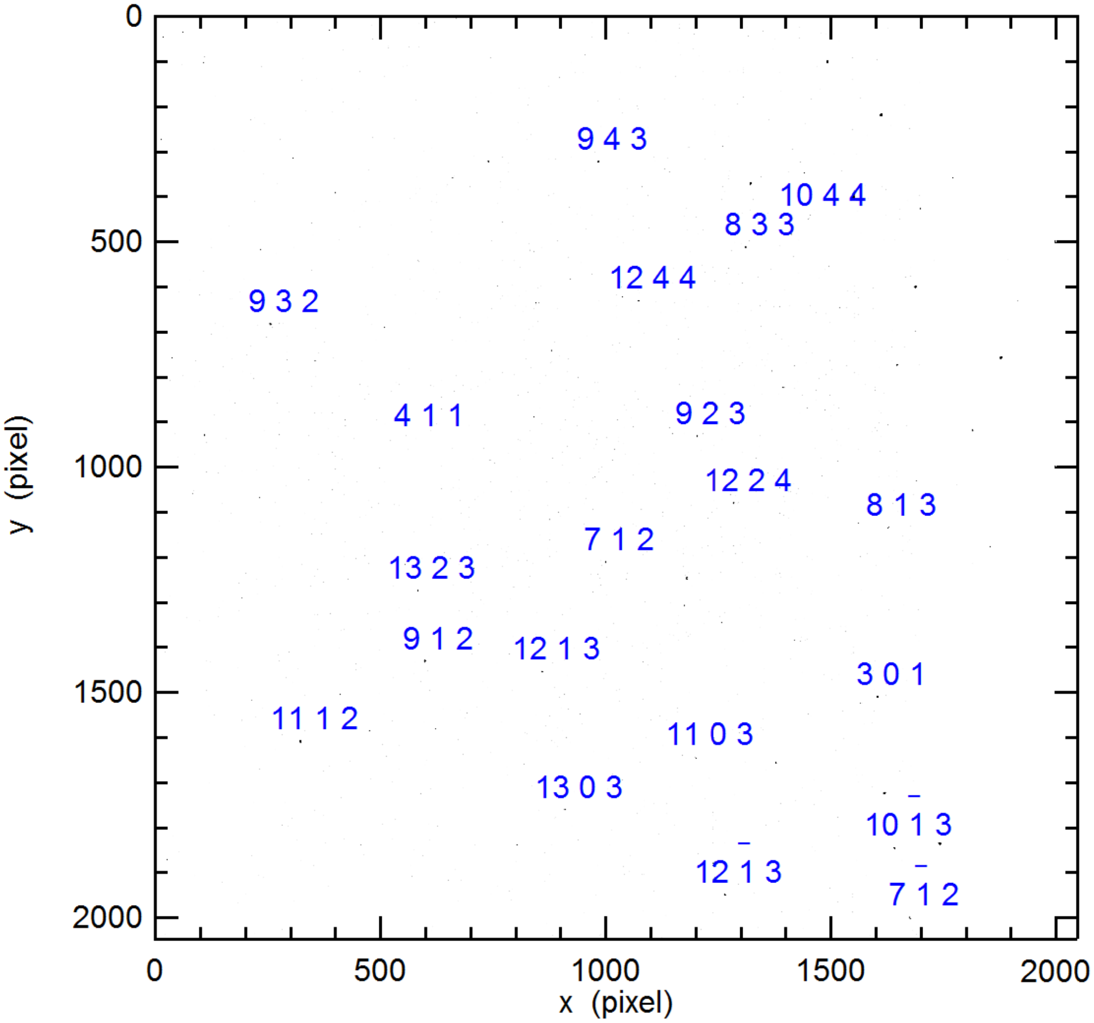

Figure 4.13 Laue microdiffraction pattern from a 1μm^3 voxel illustrated by the overlaid Sn unit cell in the recrystallized "Blue 2" orientation in Figure 4.8 [Zhou et al. (2012b)].

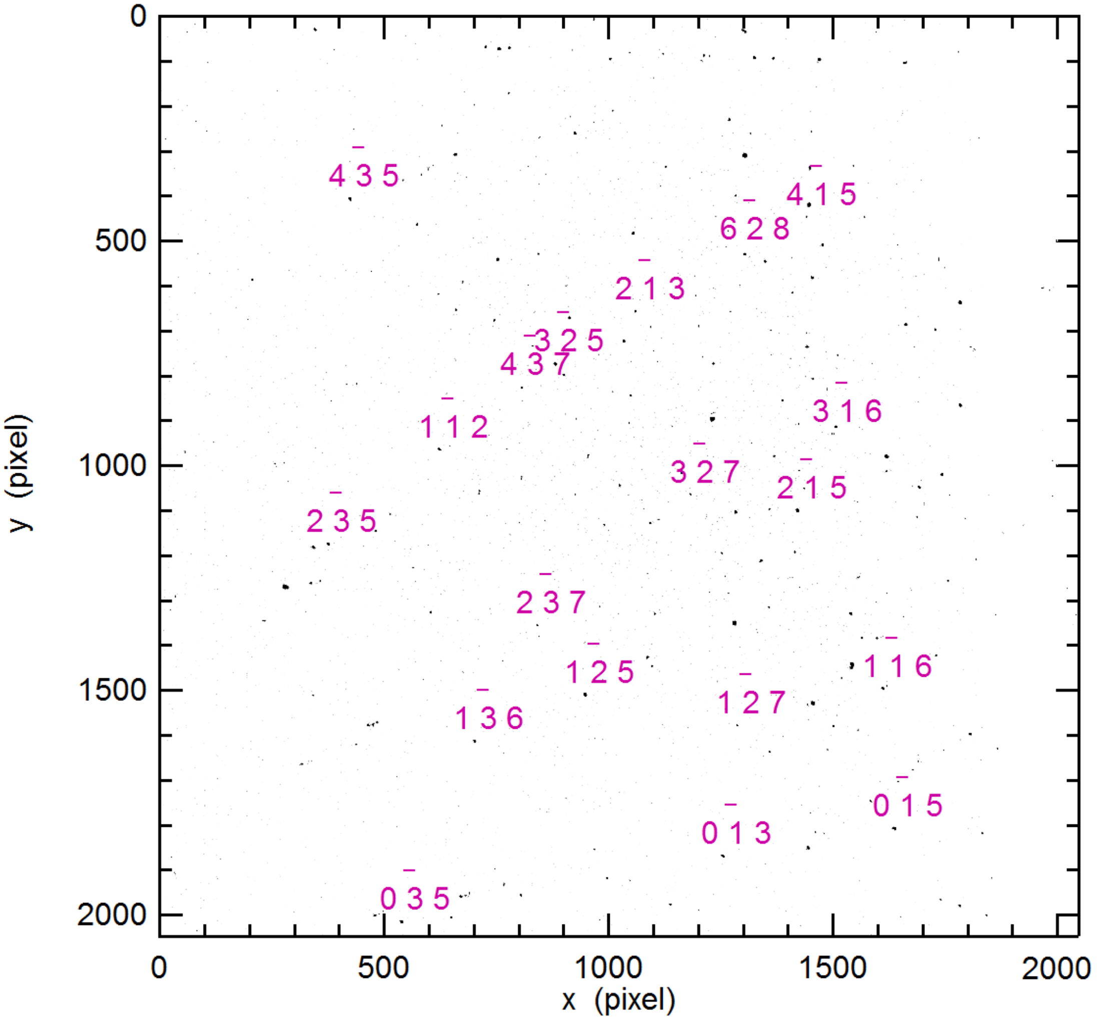

Figure 4.14 Laue microdiffraction pattern from a 1μm^3 voxel illustrated by the overlaid Sn unit cell in the small pink orientation in Figure 4.8 [Zhou et al. (2012b)].

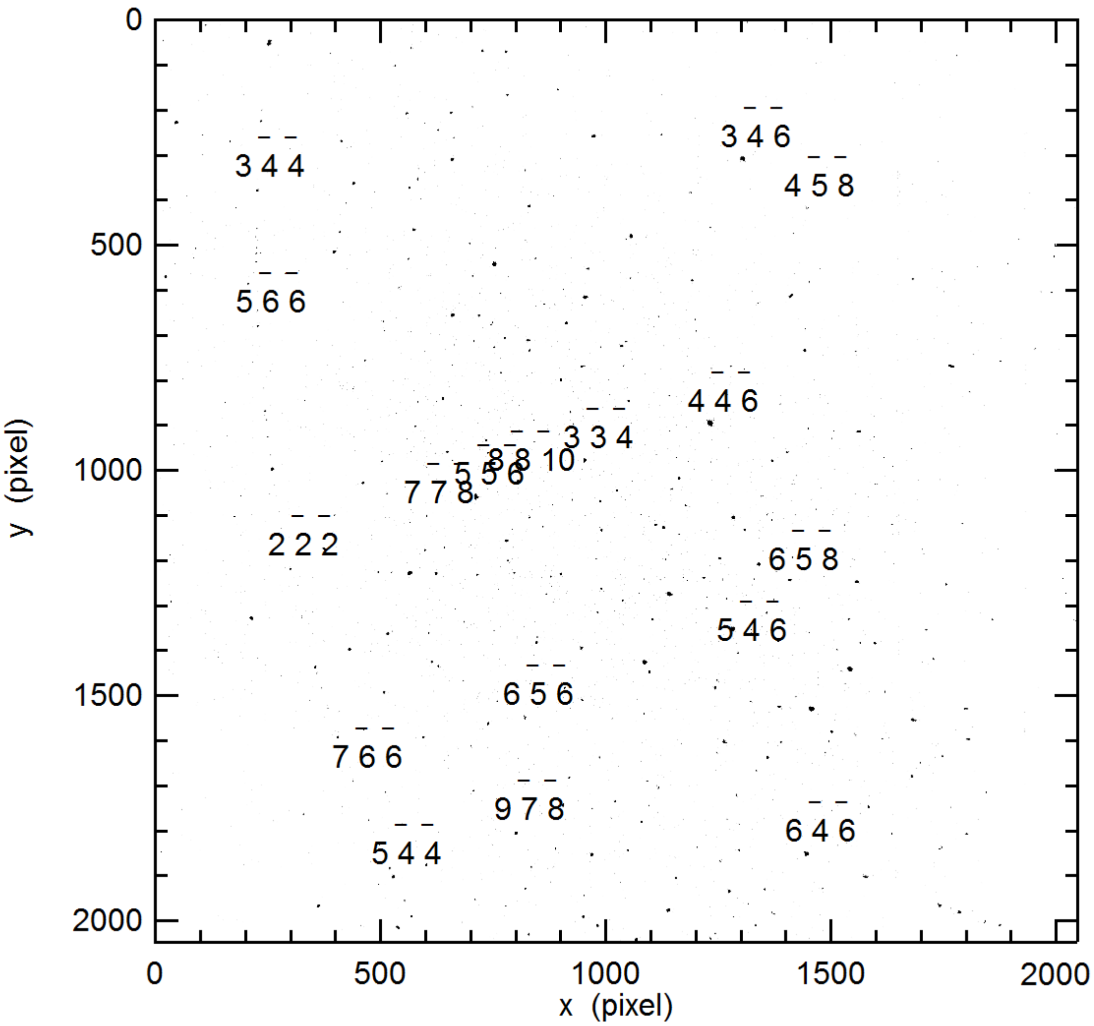

Figure 4.15 Laue microdiffraction pattern from a 1μm^3 voxel illustrated by the overlaid Cu$_6$Sn$_5$ unit cell in the IMC phase shaded in black in Figure 4.8 [Zhou et al. (2012b)].

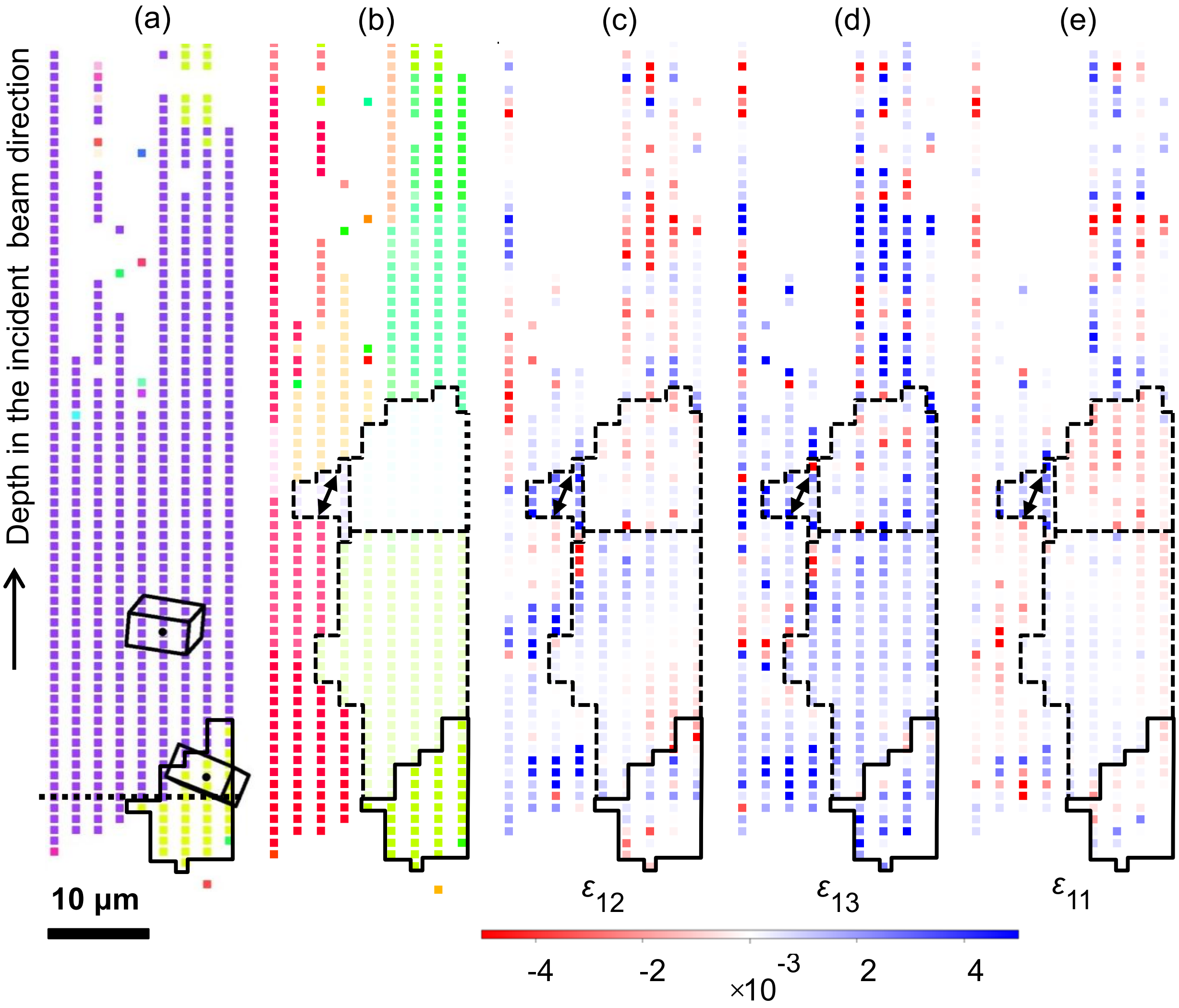

Figure 4.16 (a) DAXM orientation map of the surface line-scan #2 reveals the parent purple orientation and the recrystallized yellow grain; a 3 °orientation spread is shown in (b); components of the deviatoric strain tensor in the Sn phase are plotted in (c)-(e); sub-grain boundaries are highlighted by the black dashed lines, and solid lines for the high angle boundaries; the initial polished sample surface is approximately along the dotted line in (a) [Zhou et al. (2012b)].

4.5 Summary

In the medium-strain fine-pitch BGA package design, microstructure and Sn grain orientation evolution in lead-free solder joints occurred at lower cycle numbers (earlier) during thermal cycling. Dramatic recrystallization and large crack openings were observed in solder joints after thermal cycling to failure, particularly in the samples with pre-aging. In this package design, cracks were not only found to be correlated with a variety of Sn grain orientations, but solder joints with purple/blue orientations (which are resistant to cracking in low-strain PBGA packages) fractured. Cracks in the purple/blue orientation joints are found to be correlated with the same grain boundary evolution characteristics observed in joints with other (more vulnerable) orientations.

Sub-grain formation and recrystallization were observed to have assisted grain boundary sliding and crack propagation during thermal cycling. Gradual lattice rotation during continuous recrystallization facilitated the development of high angle grain boundaries from sub-grain boundaries. In the parent grain, many sub-grain boundaries were present and a complex sub-grain structure was often observed. Moreover, a larger orientation gradient is often present in the parent orientation, whereas the recrystallized grains are nearly free of orientation gradients and GND content. The distribution of crystal orientation gradients is distinct in different grains and sub-grains, and is separated by sharp boundaries. Different grain or sub-grain boundaries have different vulnerabilities to crack propagation. This study shows that random high angle boundaries are more susceptible to cracking, whereas twin boundaries may be able to resist crack development, but more data are needed to be certain about the effect of twin boundaries, as cracking has also been observed at twin boundaries in other studies of creep deformation [Telang

(2004b)]. The effect of grain boundary characteristics on crack development is also discussed later in the high-strain WLCSP package design.

Continuous recrystallization processes are correlated with slip activities. Strain concentrations contribute to a localized lattice rotation. It is probable that the development of recrystallized grains may be accomplished by two-step lattice rotation about low-index axes (due to slip on facile slip systems), which arise from local dislocation accumulations at sub-grain boundaries. Further straining may lead to development of local strain concentrations inside newly developed recrystallized grains, and activation of a single facile slip system can cause a small angle lattice rotation. However, larger and more random lattice rotations are less likely to be achieved by slip on a single slip system.

DAXM reveals the crystal orientation and strain distribution on and beneath the sample surface, and the heterogeneous distribution of elastic strain is correlated with recrystallization. Sharp microdiffraction peaks suggest very low GND contents inside the $1\mu m^3$ voxel. The lack of GNDs inside a crystal may be a combine effect from 1) absorption of dislocation to pre-existing sub-grain boundaries and 2) dislocation climb during the recovery process. Strain concentrations near the sub-grain boundaries are evident, indicating the presence of back stresses in sub-boundaries. Sub-grain development and grain boundary migration and coalescence during continuous recrystallization provide a pre-condition for crack nucleation and propagation. With the formation of coalesced high angle boundaries with random boundary structure, these weaker interfaces become vulnerable to opening up and become propagating cracks. The package design and the effective strain level imposed on the solder joints influence the extent and rate of microstructure evolution, so the package design is therefore crucial for determining the life-time of the solder joints.

Chapter 5

Microstructure, crystal orientation, and internal strain evolution in high-strain WLCSP packages

5.1 In-situ characterization of strain evolution during thermal cycling

In the high-strain WLCSP package, lead-free solder joints are directly connected to the Si chip, and much greater CTE mismatches (and thus larger strain) are expected in solder joints near the chip-side interfaces during thermal cycling. Compared to the other two package designs, microstructure evolution and failure occurred earlier in this package. Moreover, the relatively simple geometry of this package design enables *in-situ* characterizations of a single solder ball during the reflow and the thermomechanical deformation.

The reflow behavior of lead-free solder joints in a WLCSP design was first assessed i*n-situ* using synchrotron high-energy X-ray diffraction. An array of solder joints free-standing on the Si chip (but not attached to the circuit board) were melted and re-solidified [Zhou et al. (2012)]. Diffraction patterns from the Sn and IMC phases were collected *in-situ* during the reflow process. Upon melting, a dramatic change of diffraction peak intensities were observed from the Sn and the Ag_3Sn phases, as they were melted and dissolved, respectively. During cooling, resolidification of the Sn phase and the precipitation of the Ag_3Sn phase altered their diffraction peak intensities again. In contrast, the diffraction peak from Cu_6Sn_5 retained its intensity throughout the reflow process. Sn crystal orientations were extracted from each diffraction pattern. After each reflow, completely new Sn grain orientations always developed in the solder joint. Multiple reflows of the same solder ball yielded different crystal orientations, and there are no apparent crystallographic relationships between the new orientations and the old ones [Zhou et al. (2012)].

Using the same high-energy synchrotron transmission XRD technique, solder joints in an assembled package (with Si chip, solder joints, and PWB) were examined *in-situ* during the reflow process and the subsequent thermal cycling. The experimental set-up is shown in Figure 2.2. The whole volume of the corner ball was exposed to the incident X-ray beam, and diffraction patterns from the Sn and IMC phases were collected continuously during the melting and solidification processes. During the subsequent thermal cycling, diffraction patterns were captured periodically up to a few cycles before the sample was removed and stored for about 10 days. The sample was then thermally cycled for another 220 times off-site. The same solder joint was re-measured *in-situ* during thermal cycling two days after the additional 220TC was completed, using the same thermal cycling apparatus in the synchrotron beamline. The 220 TC was scheduled to be near the starting date of the second synchrotron assessments to minimize the effect of stress relaxations due to the recovery processes at ambient temperature.

The elastic strain evolution on a particular plane in the Sn {420) family during cooling of the reflow process is shown in Figure 5.1. The un-strained d-spacing of this plane is plotted at different temperatures (black lines). The elastic strain on this plane is drawn at corresponding temperatures using blue lines. Following solidification, at 147 ℃, the un-strained d-spacing of this Sn {420) plane is calculated to be about 1.307Å, implying a compressive strain of about 0.2% on this plane. As the solder joint cooled down, the d-spacing decreased, but the compressive strain remained nearly constant until ~97 ℃ when it began to become more negative. A comparison between the shape of this diffraction peak at 150 ℃ and 98 ℃ is shown in the inset of

Figure 5.1 (a). A threshold was set to show only the lower 4.5% of the maximum intensity of the peak at each temperature. The diffraction patterns were then inverted and the peaks appear as black. It is apparent that the same peak became slightly more streaked during the cooling process suggesting some elastic strain build-up, but the change is subtle. Although the lack of apparent change was reported in ref [Zhou et al. (2012)] in free-standing solder joints on a Si wafer, a similar result from a full package suggests that strain build-up due to CTE mismatches at the chip/solder/PWB interfaces during fabrication does not apparently alter the solidification microstructure or Sn grain orientations. The experiment was repeated in 4 different joints, and no easily identified changes were observed during cooling in any of them.

The strain evolution on this Sn {420) plane was tracked during thermal cycling. From Figure 5.1 (b), it is noted that the diffraction spot from this peak is in the lower middle part of the diffraction pattern. Consequently, this crystal plane has its plane normal close to the vertical direction (normal to the incident X-ray beam). Thus, the elastic strain on this plane is representative of the normal strain in the solder joint. During thermal cycling, the strain evolution follows the change of temperature. Figure 5.1(a) clearly illustrates the correlation between strain and temperature. As temperature increases during the heating cycle, the compressive strain is larger, and it becomes smaller (less negative) in the cooling cycle. This behavior indicates that this solder ball experiences more compressive strain at the high temperature regime of the thermal cycle, and thus it is likely to have a dominant purple/blue orientation (with *c*-axis normal to the chip/solder interface).

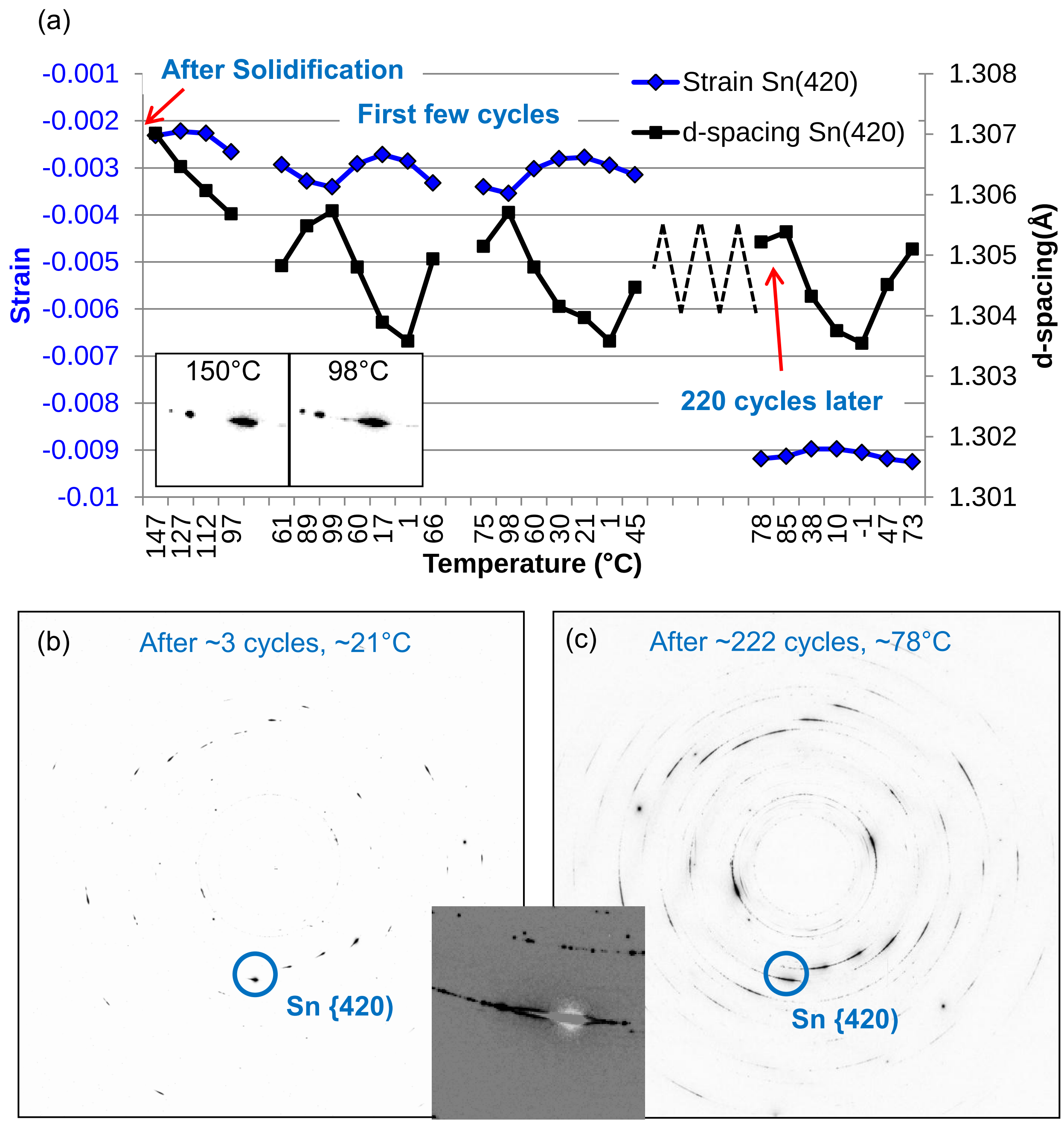

Figure 5.1 (a) Elastic strain evolution (blue lines) on a Sn {420} plane during cooling from solidification (with the diffraction peaks shown in the inset) and thermal cycling; the un-strained d-spacings are plotted in black; (b) and (c) diffraction patterns from the same solder joint showing peak broadening and streaking after 222 thermal cycles; overlaid enlargements of the Sn {420} peak are shown in the inset (with black for 222TC) [adapted from Bieler et al. (2012)].

The diffraction pattern from this solder joint yields rows of distinct streaked Sn diffraction spots in Figure 5.1 (b). It suggests that the solder ball contains one or only a few Sn crystal orientations with orientation gradients or low-angle boundaries. The diffraction peaks were captured at a very early stage of deformation (only after 3 TC). They are apparently streaked along the powder diffraction ring. Actually, the same peak already appeared streaked in this solder ball right after solidification, as shown in the inset in Figure 5.1 (a). It is thus confirmed that these orientation gradient features exist in solder joints even in the as-fabricated condition. An enlargement of this diffraction peak after 3TC is shown in the inset as white, and it is compared with the diffraction peak from the same plane after 222 TC (with the peak in black).

After further thermal cycling, Sn diffraction spots became more streaked with the same crystal orientation and the compressive strain on this plane was built up. Careful examination of the diffraction peak in Figure 5.1 (c) reveals that the Sn diffraction peak not only broadened, but it also became more “spotty” after about 222 thermal cycles (black in the overlaid diffraction pattern). As shown in the inset in Figure 5.1 (c), the diffraction peak from the same plane has a spread shape and a more complex intensity distribution compared to its earlier stage (white). The change of the shape of diffraction peaks indicates that microstructure evolution occurred during thermal cycling. Orientation gradients or sub-grains developed, shown as an expanding of streaking along the azimuth direction with distinct spots in some orientations along the streak with respect to the original peak center. At the same time, the magnitude of the compressive strain on this plane nearly tripled from the first few cycles and became more “negative” (about -0.9%) after about 220TC. Moreover, Figure 5.1 (a) shows the un-strained d-spacing of this plane, which is only a function of temperature during thermal cycling (black lines), and thus has a similar curve after 220 TC. However, strain variation is apparently smaller compared to the first few cycles with the same temperature range. Consequently, it is likely that dislocation accumulation occurred mostly in the first 200 cycles, and their absorption into low angle grain boundaries resulted in an increase of grain boundary misorientations that is evident in the diffraction pattern.

In addition to the peak streaking and broadening, there are small diffraction spots near the original peak center, which probably come from the fine grains developed by continuous recrystallization. These grains have some misorientations with the parent grain, but they have yet formed a high angle boundary. However, the roundish shape of diffraction spots argues that these grains are nearly free of defects. The findings agree with the outcomes of recrystallization mechanisms discussed in the previous chapter, in which newly developed recrystallized grains are nearly free of orientation gradients and elastic strain. The difference is that microstructure evolution and recrystallization occur much earlier in the WLCSP design due to a higher effective strain on the solder joints.

5.2 Study of the microstructure evolution in WLCSP packages using conventional analytical methods

The geometry of the WLCSP package permits only two corner joints of each package to be examined *in-situ* during thermal cycling. Thus, the characterization of a large number of solder joints is not practical by this means. However, in a different approach, two samples from the same package design in the as-fabricated condition were pre-cross-sectioned along the edge and polished without an epoxy mount. The samples were thermally cycled and characterized using the optical microscopy and EBSD before and after 112TC, 219TC, and 320TC.

It is observed from the optical micrographs in Figure 5.2 (a) and (b) that after 112TC, there is more evidence of plastic deformation in sample #1 than the other one. The development of surface topography due to thermal straining has expanded significantly from the interface into the bulk material in Ball 1, 2, 3, 5, 6, and 9 for the sample #1. In sample #2, however, shear band and slip traces in a large area are apparent only in the highest strained Ball 1 and 10 (the corner joints). Deformation is highly localized adjacent to the chip-side interface in the other eight joints in sample #2. The extent of deformation also varies from joint to joint in the same sample. For instance, in Figure 5.2 (a), Ball 6 in sample #1 exhibited shear traces in a larger area near the chip-side interface. In contrast, the deformation is more localized in Ball 10 at the upper right corner in the same sample. In general, optical micrographs from two rows of solder balls suggest that sample #1 may be more prone to deformation, whereas the other sample is more resistant to deformation.

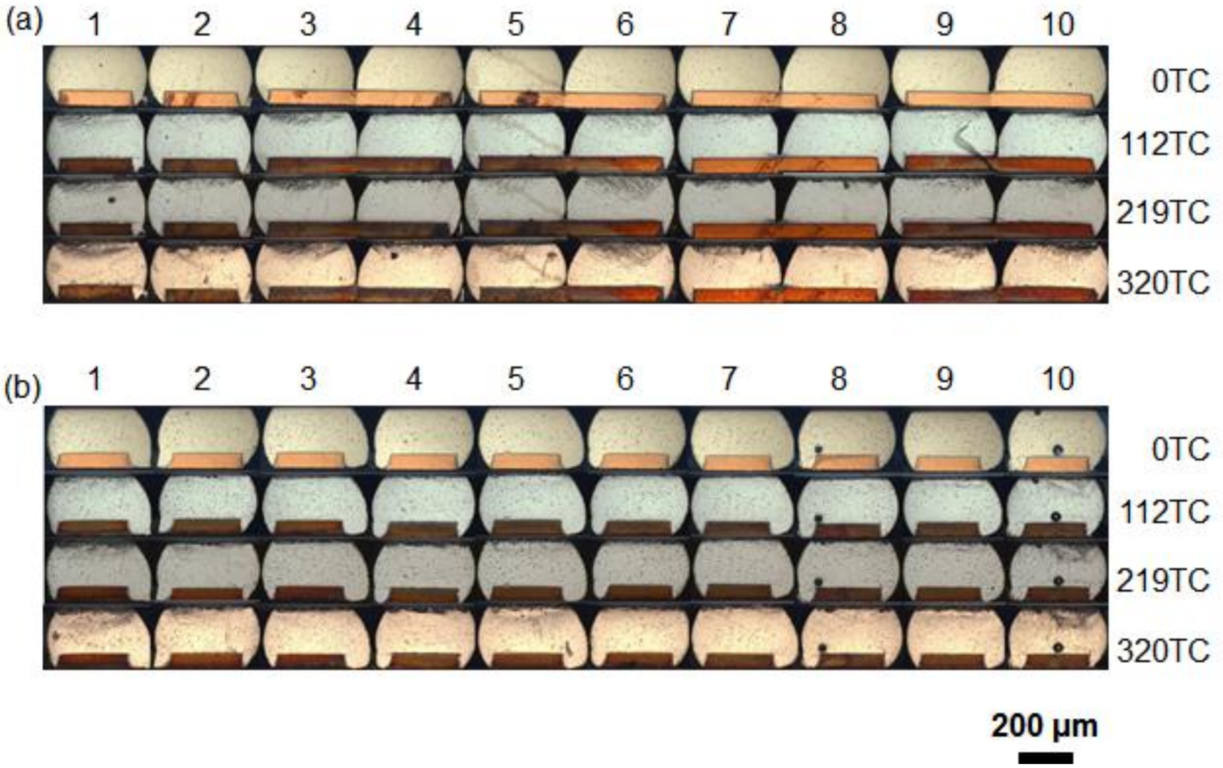

Figure 5.2 (a) and (b) Optical micrographs of the outermost row of solder joints from two WLCSP packages #1 and #2, respectively; both samples were examined in the as-fabricated condition and after 112 TC, 219 TC, and 320 TC between 0 °-100 ℃.

With further deformation after 219 cycles, deformation appears to have continued in the same manner and the heavily deformed areas were enlarged in all solder joints. Nevertheless, more dramatic development of surface topography is observed in the solder joints from sample #1, whereas in Figure 5.2 (b), no dramatic change occurred except in Ball 1 and 10. Continued straining (after 320TC) reveals more deformation and possibly fractures in some of the solder joints. For instance, cracks may have developed at the upper left corner of Ball 2 and the upper right corner of Ball 10 in sample #1.

In order to understand the correlation between the plastic deformation and microstructure evolution during thermal cycling at the corresponding stages, all solder joints in Figure 5.2 were examined using EBSD. Interestingly, before deformation (the first row in Figure 5.2 (a) and (b)) the grain orientations from these two samples are distinctly different, which may explain why plastic deformation was more readily observed in sample #1 than the other one. In Figure 5.3 (a), 8 out of 10 balls have red/orange color in the *c*-axis EBSD orientation map, one joint (Ball 9) is yellow, and only one ball (Ball 3) has a dominant blue orientation. It is also noted in this sample that nine joints are single or near-single crystal, and Ball 2 is the only one that has a multi-grain structure with a diagonal twin boundary. In contrast, 8 solder balls in sample #2 (Figure 5.3 (b)) have dominant green or dark green orientations, and the other two joints have blue orientations. As discussed earlier in this dissertation, solder joints with red/orange orientations are more prone to deformation upon thermal cycling, whereas purple/blue orientations are more resistant to deformation. These two samples have the same thermal fabrication condition, thermal histories, and strain levels at the package scale. However, the findings above further indicate that different responses to thermal strains from these two samples are attributed to the differences in the dominant Sn grain orientations in the initial condition.

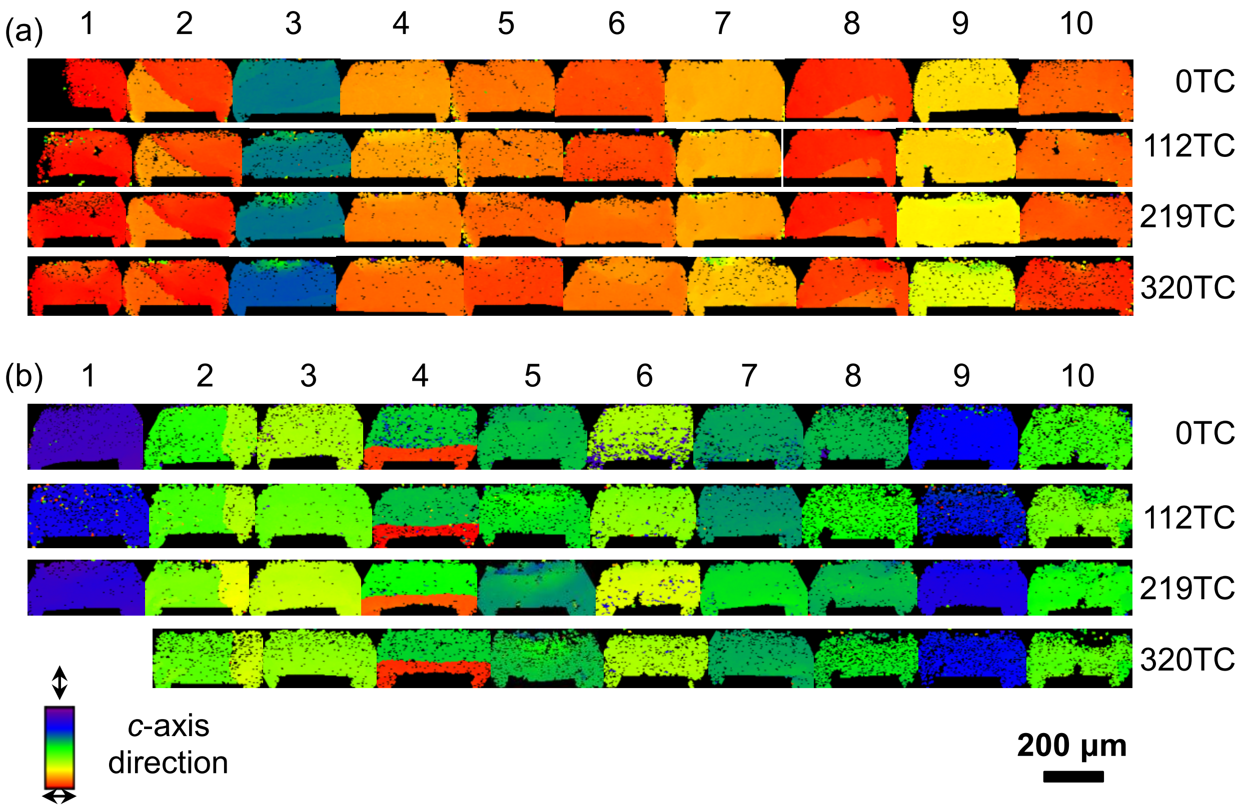

Figure 5.3 Corresponding *c*-axis EBSD orientation maps of the solder joints in Figure 5.2; the row of solder balls in each sample has mostly similar *c*-axis orientations.

It is not common to observe two rows of solder joints with similar *c*-axis orientations in other lower-strain package designs. In the WLCSP package, however, Figure 5.3 suggests preferred orientations may exist in this package design. Prior findings indicate no dramatic change in diffraction patterns from the full volume of the solder joint as it cools down from solidification. This being the case, a solder joint can maintain its solidified grain orientations upon straining during cooling, which excludes the possibility that higher strain can alter the final orientations of the solder ball during the fabrication of this package design. Nevertheless, it is still worthwhile to acquire statistics from other WLCSP samples to examine whether similar preferred Sn grain orientations are observed.

Two *different* WLCSP specimens (in the as-fabricated condition) of the same design were examined using EBSD, and the distribution of different orientation colors from a plan-view appears random in the *z*-axis average CTE maps (Figure 5.4). The distributions of different orientation colors in these two samples are shown in the left and right bars in Figure 5.4 (b), respectively. There is no outermost row in either of the samples that exhibit similarly oriented joints as the two samples in Figure 5.3. Nevertheless, there are significantly more purple and fewer green and red orientation joints in Figure 5.4 (a) than (b). But the overall distribution of Sn grain orientation colors appears random, as observed in the PBGA packages. Consequently, the near-randomness poses challenges in predicting the location of solder joints that are most likely to have early failure. Moreover, the heterogeneity exists in the as-fabricated conditions and each joint should be considered as a special case during deformation.

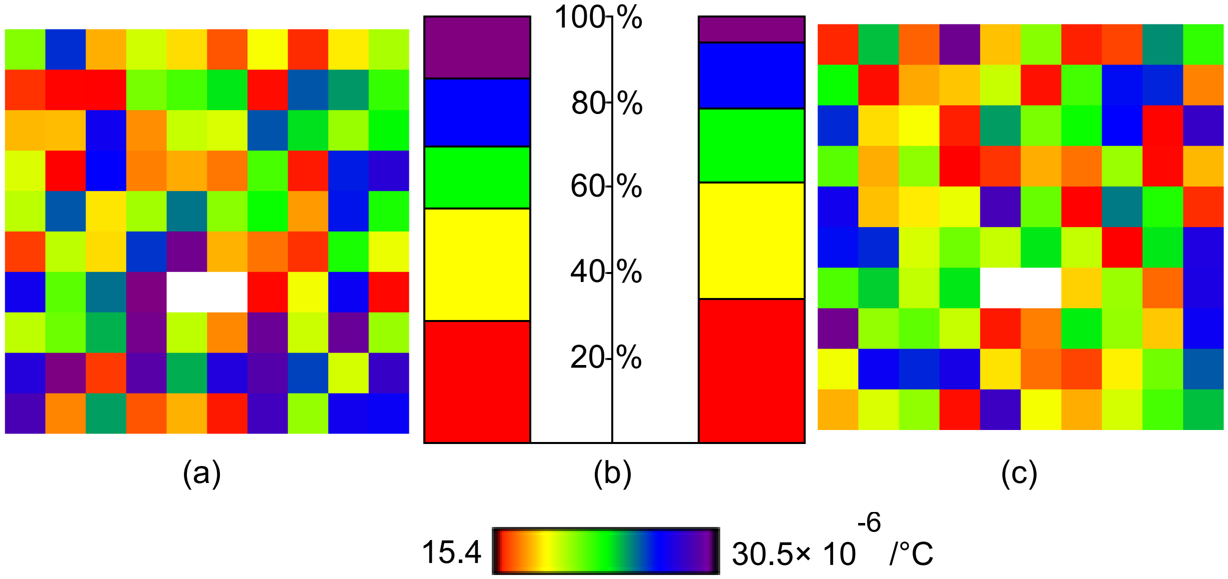

Figure 5.4 (a) and (c) Plan-view *z*-axis (normal direction) average CTE maps from two WLCSP samples in the as-fabricated condition; (b) distribution histograms of different grain orientation colors; the left bar chart corresponds to (a), and the right one corresponds to (c).

Additional information provided by the EBSD relates the plastic deformation behaviors observed in the optical micrographs with the microstructure and Sn grain orientation evolution in solder joints. After 112 TC, shear induced local orientation gradients developed in some solder joints as evident in sample #1 in Figure 5.3 (a). At the upper left corner of Ball 3, Ball 4, and Ball 7, grain orientations show a slightly different color. These orientations don't have large misorientations with the bulk grains, and they are mostly likely to be developed by gradual lattice rotation during thermal cycling, as described earlier. Optical micrographs also reveal severe plastic deformation at the chip-side interfaces in Ball 1 and Ball 10 in specimen #1. However, due to the deformation topography, lack of a flat surface limited a reliable indexation for EBSD in these regions. Use of a finer step size and a different sample orientation in the SEM improved the acquisition of meaningful data near the interface regions, which will be discussed later.

There is no apparent change of dominant Sn grain orientations in sample #2 except in the upper right corner of Ball 10 where a slightly darker green orientation developed. With a similar orientation as the bulk grain, the new grain developed during 112TC correlates well with the triangular feature shown in the same location in Figure 5.2 (b). Other changes in the grain morphology are observed in Ball 4 and Ball 6, in which the number of fine twinned grains (dark blue in the *c*-axis orientation maps) decreased dramatically after 112TC. This observation agrees with the statistics from the PBGA packages, which suggests that the number fraction of low energy low angle and twin boundaries decreases as solder joints are deformed during thermal cycling.

With further thermal cycling, the areas with apparent microstructure evolution expanded from the prior assessments, particularly in Ball 3 and Ball 7 in sample #1. Near the upper right corner of Ball 9, a light green color orientation is distinguishable from its bulk yellow grain, and the color difference indicates a small misorientation. Ball 4 in the same sample, however, developed a recrystallized fine purple grain that has a distinct orientation from the bulk orange grain. Further thermal cycling up to 320TC introduced greater microstructure evolution in both samples. Regions with newly developed grains enlarged mostly in Ball 3, 4, 7 and 9 in sample #1. For sample # 2, the poor surface conditions prevented EBSD analysis in Ball 1, and the package side interface region of Ball 10.

Distinct responses to thermal straining from the two rows of solder joints are later examined in the following paragraphs by comparison and contrast. Microstructure evolution in selected solder joints are examined in greater detail throughout their thermal history, and are correlated with slip activities and grain boundary characteristics in a later section.

5.3 Case study 1: development of grain boundary ledges and discontinuous recrystallization

In Ball 4 in sample #1, development of a grain boundary ledge and a discontinuous recrystallized grains are correlated with dislocation slip activities and the initial condition of the joint. Signatures of the plastic deformation are mostly observed at the chip-side interface in this solder ball in Figure 5.5 (a). No dramatic change of dominant Sn grain orientation is apparent in Figure 5.5 (b) after thermal cycling. Magnified optical micrographs and corresponding EBSD maps show that a grain boundary ledge developed at the upper left corner of the joint (red arrow). In Figure 5.5 (c) and (d), a new blue grain orientation (blue arrow) developed during thermal cycling up to 112TC. This recrystallized grain coarsened with further cycling. In the same location, a purple orientation was present instead after 219TC and 320TC. It is possible that formation of this purple grain was accomplished via the intermediate blue orientation.

Development of a grain boundary ledge after 112TC (marked by a red arrow in Figure 5.5 (c)) is probably correlated with the heterogeneous distribution of orientation gradients in the as-fabricated condition. The lower left part of the ledge is along a low angle grain boundary, shown as white lines in Figure 5.5 (d). After deformation, the misorientation angle and rotation axis across this boundary ledge (black arrow) evolves, but not in a monotonic sense. The grain boundary misorientation angle decreased from 3.3 ° to 2.9 ° after 219TC, and increased to 4.0 ° after 320TC. From the optical micrograph of the same area in the as-fabricated condition, it is not apparent that the initial grain orientation in this area is different from its neighboring regions. It is thus unlikely that local microstructure and IMC distribution contributed to the ledge formation. Nevertheless, an examination of local orientation gradients reveals a difference between the protrusion area and its neighbors. In contrast, other areas do not reveal such a similar distinct orientation difference. In Figure 5.5 (e), the orientation gradient of about 4 ° is present on both sides of the ledge, whereas in the protrusion area, the orientation gradient is less than 1°. This indicates that heterogeneous strain distribution during fabrication may have altered the local Sn grain orientations, which upon further thermal cycling, facilitates development of a grain boundary ledge.

The ledge formation is also correlated with slip activities and Sn slip systems with high Schmid factors are calculated using the grain orientation on the protrusion area, assuming a global shear stress state (Figure 2.3). Plane traces from all Sn slip systems are computed and compared with the morphology of the ledge. This analysis suggests that the plane traces of slip systems (001) [010] (#7) and $(001)[1\bar{1}0]$ (#8) match the trace of the boundary ledge, and both slip systems have relatively high Schmid factors (0.44 and 0.43, respectively). However, from the literature review in this dissertation, these two slip system families are not as frequently observed to be active. As discussed earlier, the global shear stress may not be representative of local stress field. It is also apparent from the grain reference orientation deviation maps that a heterogeneous strain distribution may also be initially present prior to thermal cycling. Development of this grain boundary ledge during thermal cycling may be attributed to a combined effect from both dislocation slip and surface relaxation due to residue strain in the process of fabrication and sample preparation.

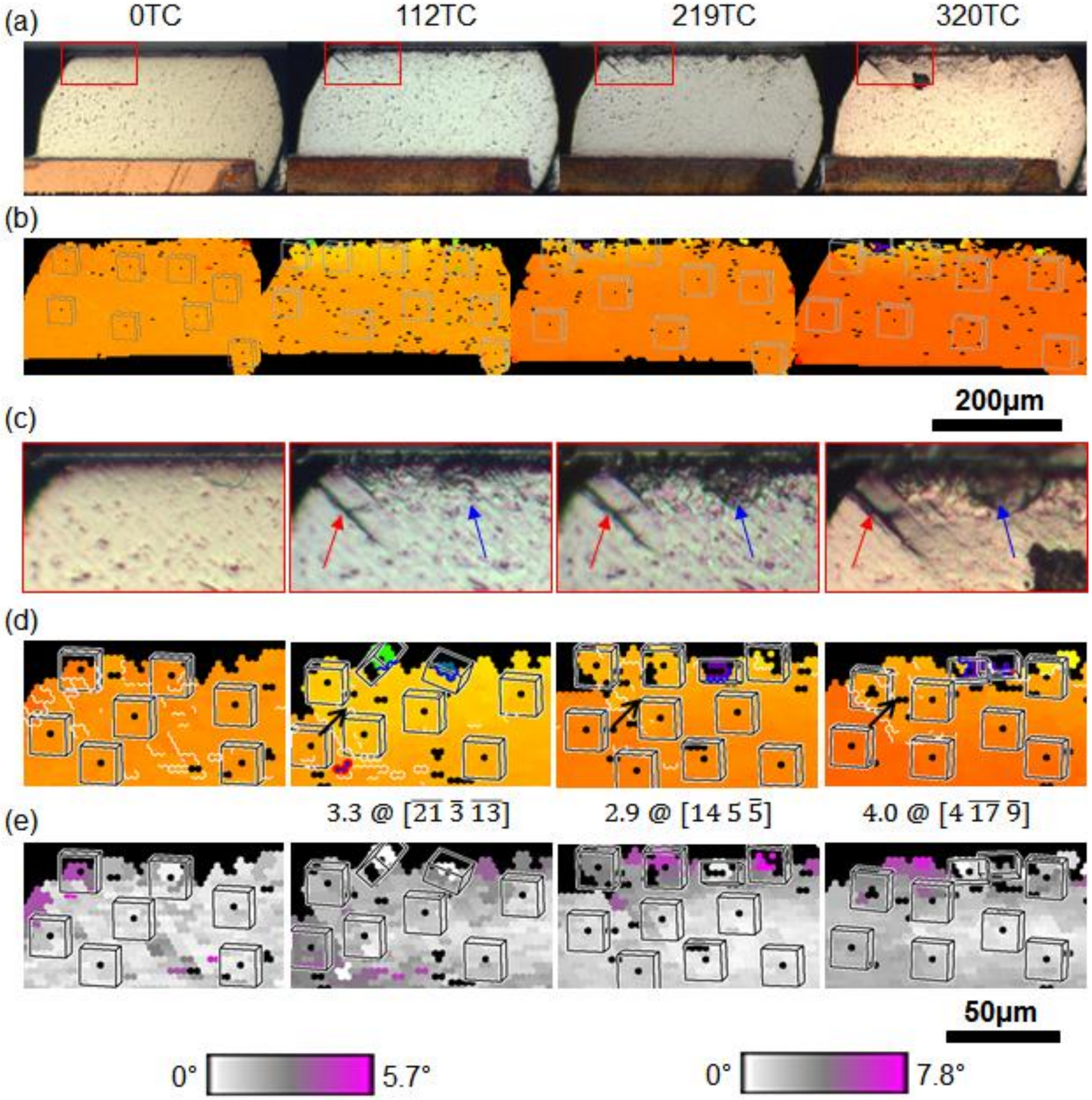

Figure 5.5 (a) Optical micrograph and (b) *c*-axis EBSD maps of the entire polished surface in Ball 4 in WLCSP sample #1 before and after 112, 219, and 320 thermal cycles; (c) magnified optical micrographs, (d) *c*-axis EBSD maps, and (e) grain reference orientation deviation maps from the upper left corner of the ball; features of microstructure evolution are marked by arrows in (c); low angle and high angle boundaries are in white and blue lines, respectively in (d).

In contrast to a surface ledge along a low angle boundary, development of a highly misoriented grain by a discontinuous recrystallization mechanism is evident (blue arrows in Figure 5.5 (c)). After 112TC, the grain boundary misorientation between the recrystallized blue orientation and the parent grain is $88.7° \ @ \ [\bar{4}\ \overline{26}\ \bar{9}]$ (close to$[0\ \bar{3}\ \bar{1}]$). This boundary is not a special boundary configuration in Sn, and the large misorientation angle indicates that the formation of this grain orientation may be difficult by a continuous recrystallization mechanism. In contrast, the purple grain developed later during thermal cycling has a misorientation of $71° \ @ \ [10\ \bar{1}\ 1]$ (close to [1 0 0]), which is a CSL boundary (Table 1.3). If this purple grain developed via the intermediate blue orientation, the resultant purple orientation would have a low-energy grain boundary configuration (a CSL boundary) than the blue orientation (a high angle random boundary). Similar to the prior analysis, the recrystallization grains are nearly free of orientation gradients in Figure 5.5 (e). The left two maps in Figure 5.5 (e) are drawn to show the orientation gradients up to 5.7 °, whereas the right two maps show a larger gradient up to 7.8 °. In both cases, recrystallized grains are displayed by white or light grey color, and their neighboring grains (which belong to the parent orientation) have greater orientation gradients.

Development of a discontinuous recrystallization event in this grain is related to a partial crack (or ledge) in the as-fabricated condition. Enlargements of the optical micrograph reveal a partial crack (or ledge) in the same location where the recrystallized grain emerged after thermal cycling. However, unlike the surface ledge discussed earlier, the *c*-axis EBSD map of this area in the as-fabricated condition does not reveal any new orientation, or an apparent orientation gradient in this neighborhood. It is thus unclear what the role of this pre-existing damage is on the nucleation of a discontinuous recrystallization. Nevertheless, it is possible that a more heterogeneous distribution of stored strain energy may be present in this area, which upon thermal cycling, is able to release and trigger the recrystallization.

In both cases, the initial conditions of the solder joint may have a large impact on the microstructure evolution. Development of both surface features is correlated with inhomogeneous strain fields. Slip on non-facile slip systems may account for the surface ledge, and for its lack of continued growth as nearby microstructural evolution developed. However, the transition from the intermediate blue orientation to the purple grain is not directly correlated with a simple lattice rotation due to slip activities. Further expansion of the discontinuously recrystallized grain could be achieved from a grain with a more stable orientation such as a blue/purple orientation, especially if it has a special boundary relationship with the parent orientation.

5.4 Case study 2: Contribution of slip from different slip systems on microstructure evolution

Development of an apparent deformation band and surface topography are correlated with slip activities in Ball 10 in sample #2. Most of the plastic deformation occurred near the upper right corner of the solder joint where a minority grain orientation is present. From Figure 5.6 (d), it is clear that this grain has a twin relationship with the parent orientation (red lines showing the twin boundary). Both orientations appear as green in the *c*-axis orientation map, suggesting that they have similar *c*-axis orientations. However, they had distinctly different responses to the imposed thermal strain. Slip traces developed after 112TC. Schmid factors of all possible Sn slip system families are calculated assuming a global shear stress, as illustrated in Figure 2.3. The top 8 slip systems with the highest Schmid factor are selected, and the plane traces of three of them match the slip traces on the micrograph, and are drawn in red lines in Figure 5.6 (c).

During the early stage of thermal cycling, slip systems $\{110)\langle 001]$ (#2), $\{101)\langle 10\bar{1}]$ (#9), and $\{121)\langle \bar{1}01]$ (#10) all have high Schmid factors, and the trace analysis finds a good match between the plane traces from slip systems #2 and #9 and the slip traces on the sample surface. There are some traces that match the plane traces from slip system #10, but the features are not very convincing. From the discussion earlier, slip system #2 is a facile slip system, whereas slip sytems #9 and #10 are not as facile. It cannot be determined which slip system was operative first since all three were present after 112TC.

With more thermal cycling (after 219TC), slip system #2 dominated the deformation. It is apparent from Figure 5.6 (c) that a set of heavier slip traces developed to the lower left of the slip trace which matches slip system #9 after 112TC. This set of traces are almost parallel to the trace of slip system #2 after 112TC, suggesting that slip on slip system #2 further expanded with more cycles. In contrast, the morphology of the slip systems #9 and #10 traces remained similar to their original state. It is thus fair to conclude that operation of slip system #2 dominated up to 219TC. With further cycling to 320TC, more surface topography and traces from both slip systems #2 and #9 were enhanced. The resultant microstructure may be the interplay of these two slip systems. The wavy lines and more horizontal features suggest more slip systems were active as thermal cycling proceeded.

Evolution of grain boundary characteristics along the twin boundary was first observed after 112TC. In the as-fabricated condition, the upper right minority grain is completely separated by a twin boundary from the parent orientation. The misorientation angle along this twin boundary are all greater than 60 °, suggesting that the formation of this relationship was probably by the (301) twinning. The twin boundary remained relatively stable up to 112TC. The misorientation angle along the upper right portion of this boundary decreased to below 60 ° (but still a twin relation) during thermal cycling.

After more thermal cycles, grain boundary migration and slip activities further altered the boundary misorientation angle. As shown in Figure 5.6 (d) and illustrated schematically in (e), both the upper left and right portions of the boundary deviated from the twinning relations after 219TC, and they became random high angle boundaries (blue lines). The grain boundary misorientation across the upper left blue line is 66 °@ $[\overline{25}\ 4\ 2]$, and 49.7 °@ $[\bar{6}\ 23\ 3]$on the upper right portion of the boundary. This indicates that the right portion of this twin boundary continued to decrease in misorientation angle after 112TC until it became a high angle random boundary. The left portion of the twin boundary, however, increased in the misorientation angle and transformed to a different random boundary. Nevertheless, the rotation axes of the new misorientations are still close to [100] (*a*-axis in Sn). The evolution of grain boundary misorientation angle may be a result of dislocation pile-up at or transmit from the twin boundary, during which the rotation axes remained stable.

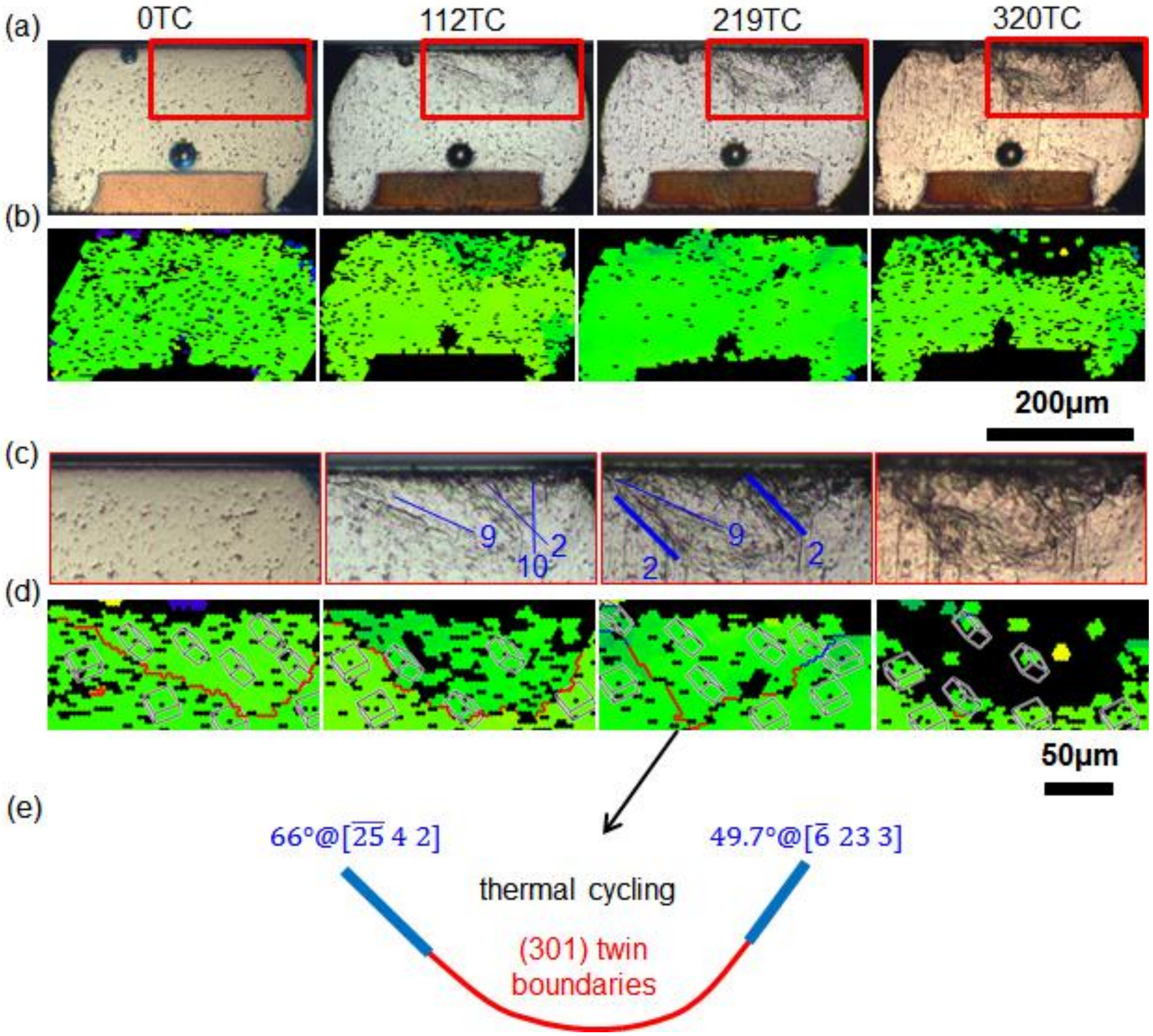

Figure 5.6 (a) Optical micrograph and (b) *c*-axis EBSD maps of Ball 10 in WLCSP sample #2 in the as-fabricated, 112TC, 219TC and 320TC conditions; (c) magnified optical micrograph and (d) *c*-axis EBSD maps of the upper right corner of the joint; calculated plane traces are marked in (c) for the sample cycled up to 112TC and 219TC; twin boundaries and high angle grain boundaries are labeled by red and blue lines in (d); (e) schematics showing the grain boundary evolution from twin boundaries to high angle random boundaries after 219TC.

High angle random boundaries developed during thermal cycling facilitated the damage propagation. It is observed in Figure 5.7 (b) that grain boundary damage initiated at the upper left corner, possibly along the initial twin boundaries. Propagation was facilitated by slip on slip system # 9 in the first 112 thermal cycles, as the trajectory of this grain boundary ledge matches the slip trace. However, further expansion of this ledge did not follow its original path in the next 107 cycles. Instead, in Figure 5.7 (c) and (d), it turned to the lower right (at the tip of the longer black arrow) where along its new path, a high angle random boundary (blue line) was present. The new path of this surface ledge also matches the slip traces of slip system #2. It is probable that operative of slip system #2 helped facilitate the development of a random high angle grain boundary, along which the ledge propagated.

A twin boundary is more resistant against damage propagation. It is clear in Figure 5.7 (e) that after 320TC, further propagation of this grain boundary ledge was inhibited at the tip of the shorter white arrow, and the ledge turned upper right. Right at the tip, the high angle random boundary ended and a twin boundary was present along the original path. This indicates that more resistance may have come from this twin boundary, whereas high angle random boundaries are more prone to facilitate the development of grain boundary damage. Similarly at the upper right corner of the joint, another grain boundary ledge developed at a high angle random boundary after 219TC. Development of the surface topography and microstructure evolution was not very dramatic after 219TC (compare Figure 5.7 (c) and (e)), suggesting that most of the deformation may have occurred in the first 219TC. This echoes the observations in Figure 5.1, where the variation of the elastic strain is less dramatic after ~ 220 cycles than the first few cycles.

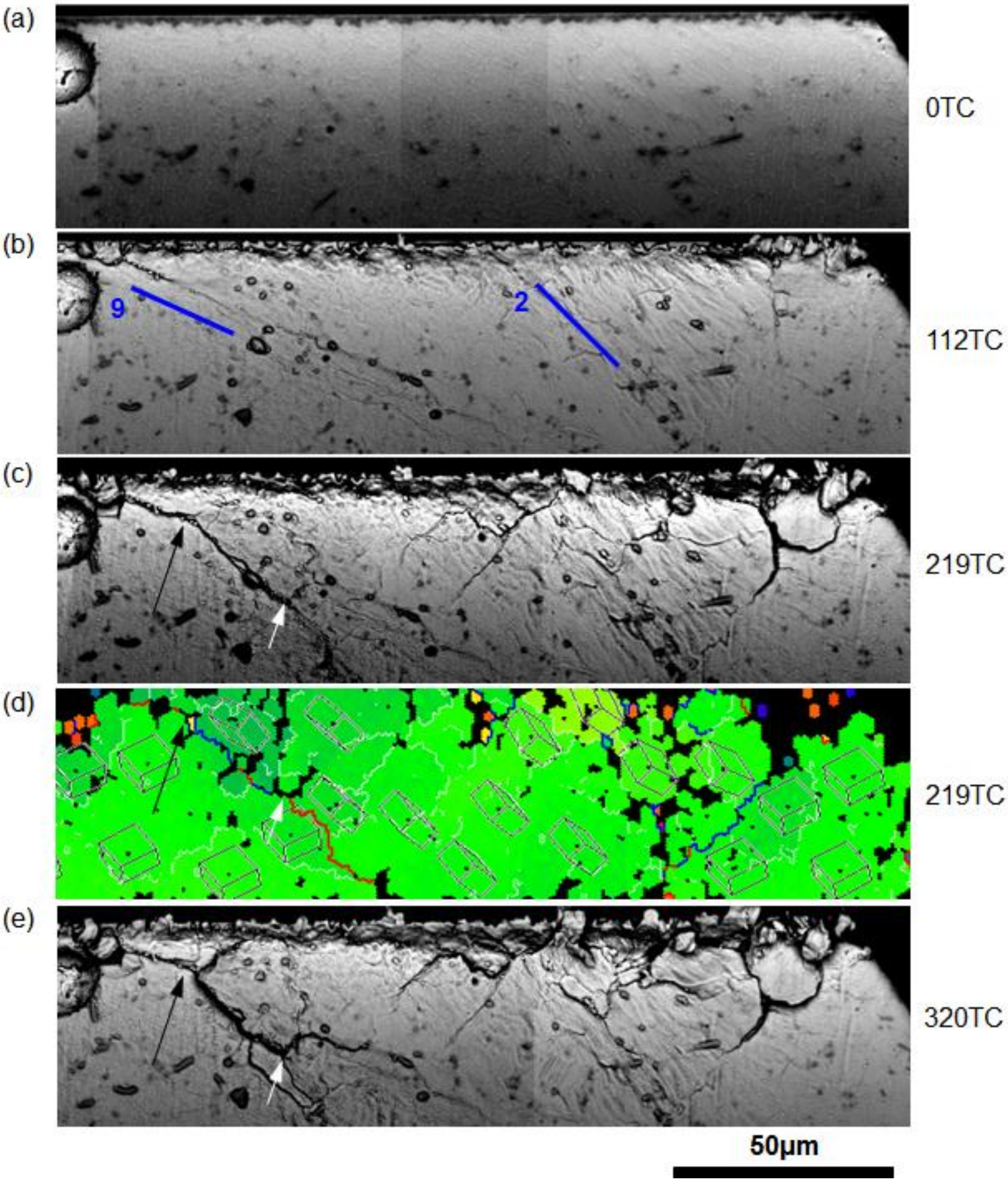

Figure 5.7 (a)-(c) and (e) Magnified BSE images of the upper right corner of Ball 10; plane traces from slip systems # 9 and #2 are shown in (b); (d) *c*-axis EBSD map corresponds to (c); twin boundaries and high angle boundaries are displayed in red and blue lines; the same features are marked in (c)-(e) by black and white arrows.

5.5 Case study 3: Continuous recrystallization in a solder joints with a grain orientation favoring non-facile slip systems

Dislocation slip activities are studied in Ball 3 of sample #1 in Figure 5.3 (a), which has a dominant dark green orientation and a complex stress state. The Sn crystal orientation of this solder joint is distinct from the other joints in the same row. During thermal cycling, due to the differential CTE value in this ball with its neighboring joints, not only shear strain, but also normal strain is imposed on the joint. For instance, with a dominant dark green orientation, the equivalent CTE normal to the interface of this ball is dramatically larger than its neighbors (Ball 2 and 4). When temperature increases, this joint would experience a compressive strain. Similarly, tensile strain is induced when temperature is decreased. Even though one can still assume that the shear strain dominates during thermal cycling, the strain state on this solder ball is likely to be more complex. Nevertheless, it is assumed in slip trace analysis that a global shear stress applies, as shown in Figure 2.3.

Optical micrographs in Figure 5.8 (a) reveal that slip activities occurred mostly near the chip-side interface in this joint. Slip traces were already apparent after 112TC, and expanded with more thermal cycles. After 320TC, the sample was lightly polished using colloidal silica suspension to remove the extensive surface topography and to make the surface a bit flatter for the EBSD characterization. The sample surface before and after re-polishing are shown in Figure 5.8 (a) and (c) after 320TC.

Lattice rotation and subgrain formation are observed in the heavily deformed regions, as shown in the *c*-axis EBSD maps in Figure 5.8 (b). These light green color orientations are separated from the parent grain by low angle boundaries. Formation of the new subgrains is accomplished by gradual lattice rotations about the Sn $\langle 110]$ axes. It is noted that the *c*-axis map from the 320TC condition shows a parent blue orientation, which is distinct from the other conditions. An overall transformation of dominant grain orientation between 219TC and 320TC is less likely. The blue orientation probably comes from the subsurface just beneath the originally polished sample surface, which is revealed by the re-polishing. The slightly different color in the *c*-axis orientation in the subsurface suggests a heterogeneous distribution of Sn crystal orientation *within* the solder joint, which is often not revealed from the view of just one cross-section. In contrast, the light green orientation in the heavily deformed regions appears similar in color to the *c*-axis orientation map before and after polishing. This indicates that the microstructure evolution and grain lattice rotation had expanded beyond the initially polished free surface into the bulk material. However, the extent of continuous recrystallization beneath the sample surface is unknown.

Extensive slip traces shown in the magnified optical micrographs in Figure 5.8 (c) after 112TC are correlated with slip on slip systems $\{121)\langle\bar{1}01]$ (#10) and (001) [010] (#7). By assuming a global shear stress as discussed earlier, plane traces of slip systems with Schmid factor greater than 0.4 are calculated and compared with the apparent slip traces. It is observed that the traces from slip systems #10 and #7 match the slip traces near the chip-side interface during the early deformation. However, there are traces on the left of the magnified micrograph in Figure 5.8 (c) which do not agree with any of the slip systems with high Schmid factors. Instead, one slip system in slip system family #10 has its plane trace aligned with this slip trace, but this slip system has a very low Schmid factor, indicating that it is less likely to be operative. Nevertheless, the discrepancy may be explained by the complex stress states in this particular solder joint. The assumption of a dominant shear stress may not be appropriate. It is not practically easy to obtain the true stress states in the solder joints from common experimental methods. Consequently, a reliable crystal plasticity model is required for simulation which may produce a more probable estimate of the real stress state under thermal cycling. A more accurate Schmid factor values may thus be calculated using the new stress state. Nevertheless, in any case, the assumption used above is still useful for estimation in most cases.

With further cycling up to 219TC, the change of local crystal orientation activated more slip systems, and the trace analysis indicates additional slip activities on $\{110)\langle 001]$ (#2), $\{100)\langle 010]$ (#3), and $\{010)\langle 101]$ (#6). At the same time, similar traces can also be tracked back to slip systems (001) [010] (#7), $\{001)\langle 110]$ (#8), and $\{121)\langle \bar{1}01]$ (#10). As reviewed earlier, all operative slip system here determined by trace analysis are non-facile, expect for slip system #2. It is thus likely that the initial grain orientation only favors non-facile slip systems. As deformation proceeded, gradual lattice rotation led to new grain orientations, in which a facile slip system gained traction when its Schmid factor became higher. Similarly as discussed in the previous chapter, the rotation axis due to the activation of a certain slip system can be calculated based on its plane normal and slip direction. Operation of slip system #2, for instance, will lead to a lattice rotation about [110] axis if an edge dislocation of this slip system is able to glide on the $(1\bar{1}0)$ plane, and in the [001] direction. As revealed from Figure 5.8 (d) that gradual lattice rotation about [110] is more apparent after 219TC and 320TC. The likelihood of an operative facile slip system #2 is quite possible during the later stage of thermal cycling.

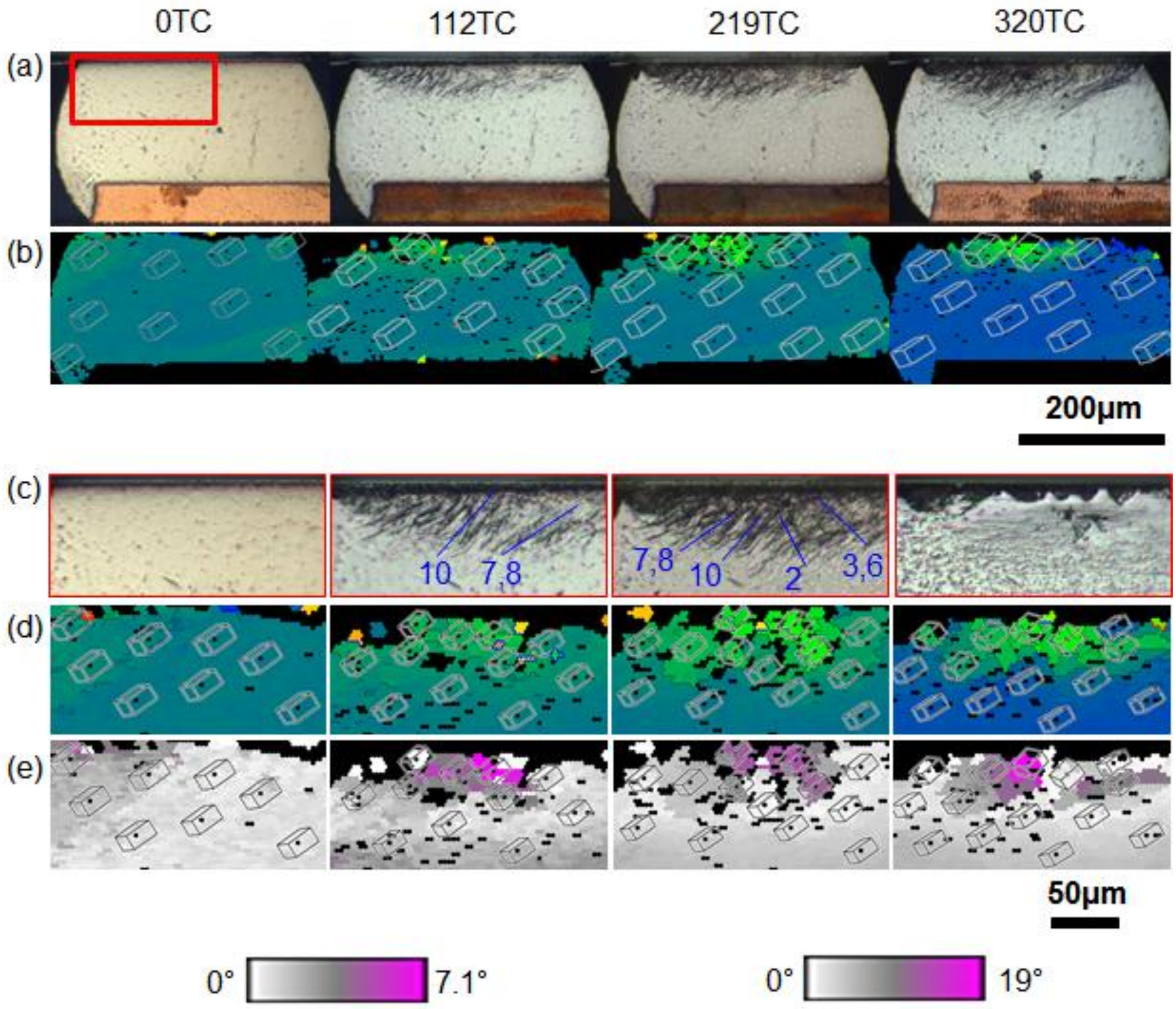

Figure 5.8 (a) Optical micrograph and (b) *c*-axis EBSD maps of Ball 3 in sample #1 in the as-fabricated, 112TC, 219TC, and 320TC conditions; (c) magnified optical micrographs and (d) *c*-axis EBSD maps of the chip-side interface region; calculated plane traces (red lines) from slip systems with high Schmid factors are marked in (c); (e) orientation deviations from the grain average orientation in the as-fabricated and 112TC conditions are drawn up to 7.1 °, and the GROD maps for the 219TC and 320TC show orientation gradients up to 19 °.

Development of sub-grain boundaries and gradual lattice rotation are apparent in Figure 5.8 (e). Grain reference orientation deviation maps are drawn using different scales for the first two and the last two conditions. For the as-fabricated and 112TC cases, the local orientation gradients are much lower in magnitude, and the maps show the gradients up to 7.1 °. Apparently, little orientation gradient was present before thermal cycling. As deformation proceeded up to 112TC, an orientation gradient of about 7 ° is observed near the chip-side interface (magenta color). Development of this magenta color sub-grain may be accomplished by the gradual lattice rotation about a Sn [110] axis due to dislocation slip. A more homogeneous change of orientation gradient colors is observed from the light grey parent orientation toward the magenta subgrain via some dark grey (3 °- 4 ° gradient) regions. This type of transition is continuous, and the change of grain orientations via low angle boundaries (black lines in Figure 5.8 (d)) is apparent.

With further cycling up to 219TC, larger orientation gradients are observed. The dark magenta areas in Figure 5.8 (e) indicate an orientation gradient of about 13 °. In spite of a large gradient from the average grain orientation, development of this subgrain may still be accomplished by gradual lattice rotation through a series of low angle grain boundaries originating from the parent grain. A transition from the light grey, to the dark grey, and to the dark magenta color in Figure 5.8 (e) indicates the continuous recrystallization mechanism. However, the gradual increase of grain boundary misorientation did not yet produce high angle boundaries. The development of new orientations took place slower in this orientation than in other crystal orientations.

Only after 320TC did the development of large orientation gradients occur. As shown in Figure 5.8 (e), a subgrain with an orientation gradient of about 19 ° (magenta color) emerged at the heavily deformed region. The magnitude of orientation gradients suggests that with respect to the bulk grain, this is no longer a subgrain, but it is a recrystallized grain highly misoriented from the average parent orientation. Even so, the lack of high angle grain boundaries between the parent blue orientation and the light green grain near the interface indicates that this grain formed by the continuous recrystallization mechanism via the intermediate transition stage as discussed above. Similar to the earlier observations during thermal cycling, development of this grain was accomplished by the increasing boundary misorientations and gradual lattice rotation. A series of low angle boundaries (black lines in the *c*-axis EBSD map) can be found in the path of this transition. The continuous recrystallization, as discussed earlier, is strongly correlated with slip activities. Activation of a facile slip system #2 may thus be responsible for the required lattice rotation to produce the new grain in this particular solder joint.

As discussed above, the rotation about [110] is likely to be correlated with the operative of slip system #2. In order to quantify this, rotation axes of all grain boundaries in the same region of Figure 5.8 (d) are characterized. A tolerance angle of 0.3 ° was selected to minimize the overlap of different statistics along the same portion of the boundary. The grain boundary length associated with each of the three rotation axes is extracted from EBSD, and the number fraction of each rotation axis among the three is shown in Figure 5.9 for the same thermal cycling conditions. Only [001], [100], and [110] axes are considered, the total lengths of which cover about 40-50% of the total boundary lengths in the scanned areas in Figure 5.8 (d).

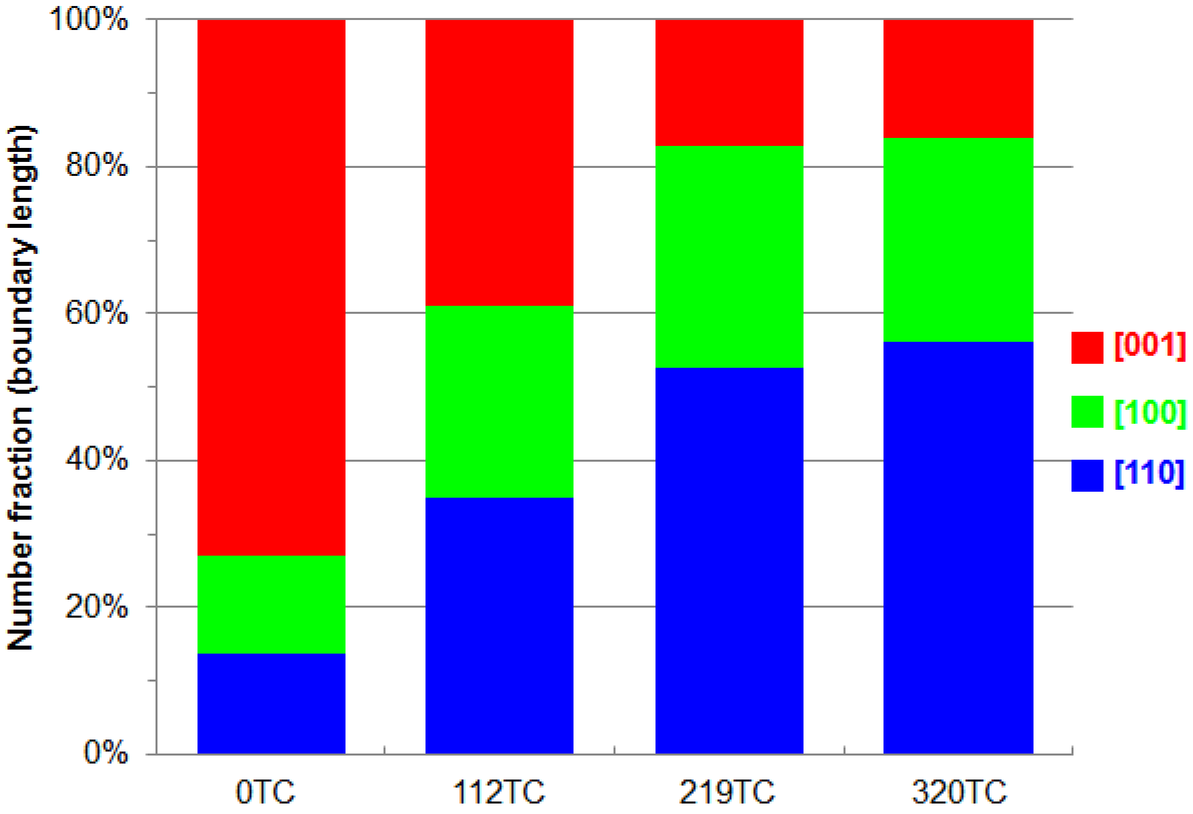

Figure 5.9 The number fraction of the lengths of grain boundaries with rotation axes about [001] (red), [100] (green), and [110] (blue) in the as-fabricated, 112TC, 219TC, and 320TC conditions; a tolerance angle of 0.3 ° was selected to minimize the overlapping of different statistics.

An increase of grain boundaries with [110] rotation axes upon thermal cycling is correlated with the activation of slip system #2. In the as-received condition, boundaries with the [001] rotation axis dominate, and only a small fraction of boundary lengths are correlated with rotations about two other axes. During thermal cycling, the number fraction of boundary rotation axes changed dramatically. Boundaries with [001] rotation axes were reduced in half compared to the initial condition, whereas boundaries with [100] and [110] rotations nearly doubled in lengths after 112TC. With more thermal cycles, the number fraction of boundaries with [100] rotation axes did not change significantly. In contrast, the number fraction of [110] rotation increased nearly monotonically. More grain boundaries exhibited rotation about the [110] axis, particularly after 112TC. This agrees well with the emergence of slip traces from the slip system #2 (Figure 5.8 (c)) in the same condition. An estimation of the lattice rotation due to the activation of this slip system (assuming edge dislocation) suggests that a [110] rotation axis is correlated with slip system {110)⟨001] (#2). The activation of this facile slip system thus led to more boundaries with [110] rotation axes. Evolution of the grain orientation and boundary characteristics may thus be stimulated by the slip activities.

5.6 Summary

Due to the high-strain package design, microstructure evolution and failure occurred earlier in lead-free solder joints in WLCSP packages. The trend of evolution is characterized using both *in-situ* synchrotron XRD and conventional methods. In the first approach, the elastic strain evolution in a single joint was examined during the reflow process and the subsequent thermal cycling. For a particular solder ball (which is likely to have a dominant purple/blue orientation), a compressive strain was built up during cooling after solidification. The magnitude of strain is directly correlated with the temperature during the first few cycles. After about 220TC, however, the magnitude of compressive strain on the same plane was increased, and the fluctuation of strain values within the same temperature range decreased dramatically. This suggests that plastic deformation induced strain hardening may have slowed down due to the interplay between the strain hardening and softening by the annealing process. Microstructure evolution is also visible from the diffraction pattern, as the diffraction peaks from the same plane became more streaked and “spotty” like. It is likely that continuous recrystallization may have occurred and new grain orientations with fewer dislocations developed.

In the other approach, it is found from two rows of solder joints sectioned along the edge of the WLCSP packages that slip occurred more readily in one sample with similar Sn grain orientations, but not in the other. The two specimens were thermally cycled and examined using optical microscopy and EBSD before and after 112TC, 219TC, and 320TC. Even though the two rows of solder balls have the same thermal history, they exhibited distinct deformation behaviors. In one sample, slip traces and shear banding are commonly observed for almost all ten balls, whereas only the corner joints in the other sample show apparent slip traces. EBSD results from these two samples indicate that solder joints from each of the samples have similar *c*-axis Sn crystal orientation. In the sample that show more slip activities, nine out of ten solder joints have dominant red/orange or yellow orientations. In the other sample, however, eight out of ten joints have dominant green orientations, and two have purple/blue orientations. This may explain why upon thermal cycling, the deformation behaviors from these two rows were distinctly different.

Case studies using the conventional characterization methods compare the microstructure and Sn grain orientations before and after different intermediate steps during thermal cycling. It is found that development of grain boundary ledges, as well as highly misoriented grains during continuous recrystallization, are correlated with slip activities. Assuming a global shear stress, operation of Sn slip systems with high Schmid factors may be responsible for the above microstructure evolution. The change of grain boundary characteristics may influence the damage development, particularly the path of crack propagation. Random high angle boundaries are more vulnerable to crack propagation or the development of grain boundary ledge, whereas twin boundaries are more resistant to damage. It is also observed that a gradual lattice rotation about the Sn [110] axes may be responsible for the development of new grains during continuous recrystallization. In a particular ball, more grain boundaries are associated with the [110] rotation axes, and less with the [001] axes, as thermal cycling proceeded. The increase of grain boundaries with preferred rotation axes may be correlated with the operative of a facile slip system $\{110\}\langle 001]$ (#2) during a later stage in thermal cycling.

The evolution of Sn crystal orientation and recrystallization during thermal cycling in three package designs with different pre-aging conditions is summarized in Table 5.1. As discussed earlier, in the low-strain PBGA package, both the initially dominant and later developed red orientations (with *c*-axis nearly aligned with the interface plane) are strongly correlated with cracking. This is evaluated using the cumulative crack length (CCL) and the number of cracked joints (CJ). Development of vulnerable high angle grain boundaries during grain orientation evolution (from the yellow to red and green orientations, and from the green to red and blue orientations, etc.) facilitated intergranular cracking (IGC), and this was also observed in higher strain packages. In addition, transgranular cracking also occurred in the low-strain packages, particularly in solder joints with dominant red orientations regardless of pre-aging conditions.

In the medium-strain fine-pitch BGA package, however, no apparent transgranular cracks were observed. Crack mainly propagated along the recrystallized grain boundaries. Compared to the low-strain packages, more dramatic recrystallization occurred in the higher strain design, and the newly developed recrystallized grains have a variety of orientations (“mix” in Table 5.1). Intergranular cracking was observed even in solder joints with dominant purple/blue orientations.

Sn crystal orientation evolution during thermal cycling in the high-strain WLCSP was assessed in terms of recrystallization characteristics. As described earlier, slip occurred more readily in one sample with most red/orange orientation joints, and both continuous recrystallization (CR) and discontinuous recrystallization (DR) events were observed. In the other sample with most blue and green orientation joints, only continuous recrystallization occurred and the Sn grain orientations tend to evolve into the neighboring color orientations (green to blue and blue to green, etc.).

Table 5.1 A summary of the Sn crystal orientation evolution in different package designs and pre-aging conditions.

	Low strain PBGA			**Medium strain fine-pitch BGA**		**High strain WLCSP**
Dominant *c*-axis	Unaged+ 6400TC	100 ℃ 500hr +6400TC	150 ℃ 1khr +6400TC	Unaged+TC	150 ℃ 500hr+TC	Unaged+ 320TC
Red	~62% CCL Rx ~31% CJ IGC(red, yellow), TGC	~47% CCL Rx ~64% CJ IGC(red, green), TGC	~41% CCL Rx ~78% CJ IGC(red), TGC	IGC(red, green)	IGC(red, orange, mix)	CR(orange, yellow, green), DR(red, orange, purple)
Yellow	~19% CCL IGC (red),TGC	~32% CCL IGC(red, green)	~47% CCL IGC(red, green)	IGC(red, green)	IGC(mix)	CR(orange)
Green	~19% CCL IGC(red, blue), TGC	~21% CCL IGC(red, blue)	~12% CCL IGC(red, blue), TGC	IGC(blue)	IGC(blue, red)	CR(blue)
Purple/blue	No crack	No crack	No crack	IGC(blue)	IGC(green, mix)	CR(green)

CCL: cumulative crack length CJ: cracked joints (in numbers) TGC: transgranular cracking

IGC: intergranular cracking CR: continuous recrystallization DR: discontinuous recrystallization

The orientation colors inside the parentheses represent the new orientation developed by recrystallization.

Chapter 6

Conclusions and Future work

6.1 Conclusions

In this dissertation, the microstructure and Sn grain orientation evolution in lead-free solder joints during thermal cycling was examined in three different package designs, low-strain PBGA, medium-strain fine-pitch BGA, and high-strain WLCSP. EBSD and synchrotron XRD were used for surface and sub-surface assessments. As summarized in Table 5.1, distinct microstructure evolution trends were observed in different package types with various pre-aging conditions. The findings in this study shed a light on the fundamental understanding of the correlation between Sn grain orientation (evolution) and damage development.

The effective strain level is considered when the microstructure evolution and damage development are addressed in different package designs. Specifically, in low-strain PBGA packages, the dominant and recrystallized red orientations (with the Sn [001] direction aligned within about 18 ° of the interface plane) are strongly correlated with crack development, whereas purple orientations (with Sn [001] direction inclined greater than ~72 ° from the interface) joints are more resistant to cracking. In higher strain packages, however, the dominant Sn grain orientation has less influence on cracking, but the recrystallization induced high angle boundaries facilitated crack propagation. Nevertheless, at the early stage of deformation, the dominant red orientations do have a strong impact on the deformation behaviors of solder joints in the high-strain WLCSP. It is thus concluded that the strong correlation between Sn grain orientation and damage/cracking is significant in low-strain packages and the early stage of deformation in higher strain packages.

Microstructure evolution and recrystallization preceding cracking is apparent in all three package designs. The comprehensive study in this dissertation promotes the understanding of the recrystallization behavior in solder joints during thermal cycling. Both continuous recrystallization and discontinuous recrystallization processes were observed. With the knowledge of the relative activities of different Sn slip systems from our prior study [Zhou et al. (2009b)], the evolution of microstructure and grain boundary characteristics in lead-free solders was successfully correlated with dislocation slip activities. During continuous recrystallization, the development of new grain orientations may be accomplished by two-step lattice rotation about low-index axes, by means of slip on facile slip systems. The highly recovered defect-free grains developed by continuous recrystallization provide a pre-condition for the nucleation of the primary recrystallization process. These findings connect the two recrystallization mechanisms, which are mainly responsible for developing high angle grain boundaries that are prone to crack propagation.

Grain boundary evolution is also correlated with slip activities. A preferred grain boundary rotation axis (Sn [110]) was developed when a facile slip system $\{110)\langle 001]$ (#2) was activated, which facilitated grain boundary ledge formation as deformation proceeded. On the other hand, when the grain boundary had a twin orientation relationship, it impeded crack propagation.

The heterogeneous distribution of orientation gradients and residual elastic strains in solder joints after thermal cycling was revealed non-destructively by DAXM. The parent grain has large orientation gradients and the recrystallized grains are nearly free of orientation gradients. Higher orientation gradients were also observed near sub-grain boundaries and IMC precipitates, where the residual elastic strain value is also high. Local strain concentrations and an increase in the orientation gradients are probably correlated with the operative facile slip systems, and have been demonstrated in a few instances where deeper analysis was made. The ability to be able to assess recrystallization behaviors non-destructively does permit further understanding of the microstructure evolution and the deformation mechanisms during thermal cycling in lead-free solder joints.

6.2 Future work

A similar approach to characterize the microstructure and Sn grain orientation evolution in pre-cross-sectioned WLCSP samples can be proposed to examine the solder joints with pre-aging conditions. It will be quite helpful to understand the evolution of grain boundary characteristics during aging, and its effect on recrystallization upon the subsequent thermal cycling. At the same time, the coarsening of IMCs during the pre-aging treatment can also be studied for the same sample, which allows a direct comparison on the effectiveness of pinning on grain boundary migration. The size and distribution of IMCs and its evolution upon pre-aging and at different stages during thermal cycling can be examined from both optical and SEM micrographs. Tracking the interplay between the change of IMC morphology and sub-grain boundaries can shed a light in answering why recrystallization occurs in the location where it is observed. The contribution of coarsened IMC particles on the Sn grain boundary mobility during thermal cycling can be studied using DAXM. The evolution of local orientation gradients and the residual strain distribution near the IMC particle can be obtained at different stages during thermal cycling. This can be done using a pre-cross-sectioned sample, and both surface and sub-surface characterization can be accomplished using EBSD and DAXM.

During the life-time of electronic devices, it is common that more than one type of deformation occurs. In order to assess the reliability issues of lead-free solder joints more completely, a combined deformation mode (high strain rate impact test and thermal cycling) can be implemented. The deformation mechanisms revealed from the individual test can be compared with that from a combined test. Both mechanical twining and dislocation slip need to be addressed. Different response of Sn and IMC phases to deformation can be examined.

In the present work, active Sn slip systems were determined from the Schmid factor and plane trace analysis, in which a big assumption of a global stress state was implemented. Although this serves as a way to estimate which slip systems would be the most active, a representation of the local stress states can be obtained from the crystal plasticity finite element models (CPFEM). Microstructure and grain boundary evolution can thus be linked with local strain/stress variation, which would be useful for refining modeling approaches and rules for slip activation.

REFERENCES

REFERENCES

Abtew M. and Selvaduray G., 2000, Lead-free solders in microelectronics, MAT SCI ENG R, Vol. 27, No. 5-6, 95-141

Adams B.L., Wright S. I., and Kunze K., 1993, Orientation imaging: the emergence of a new microscopy, METALL MATER TRANS A, Vol. 24, No. 4, 819-831

Alam M. N., Blackman M., and Pashley D. W., 1954, High-angle Kikuchi patterns, P R SOC LONDON, Vol. 221, No. 1145, 224-242

Anderson I. E., 2007, Development of Sn–Ag–Cu and Sn–Ag–Cu–X alloys for Pb-free electronic solder applications, J MATER SCI-MATER E, Vol. 18, No. 1-3, 55-76

Arfaei B., Tashtoush T., Kim N., Wentlent L., Cotts E., and Borgesen P., 2011, Dependence of SnAgCu solder joint properties on solder microstructure, ELEC COMP C, 61st IEEE, 125-132

Bieler T. R., Jiang H., Lehman L. P., Kirkpatrick T., Cotts E. J., and Nandagopal B., 2008, Influence of Sn grain size and orientation on the thermomechanical response and reliability of Pb-free solder joints, IEEE T COMPON PACK T, Vol. 31, No. 2, 370-381

Bieler T. R. and Telang A. U., 2009, Analysis of slip behavior in a single shear lap lead-free solder joint during simple shear at 25 ℃ and 0.1/s, J ELECTRON MATER, Vol. 38, No. 12, 2694-2701

Bieler T. R., Lee T. –K., and Liu K. –C., 2009b, Methodology for analyzing strain states during in situ thermomechanical cycling in individual lead-free solder joints using synchrotron radiation, J ELECTRON MATER, Vol. 38, No. 12, 2712-2719

Bieler T. R., Zhou B., Blair L., Zamiri A., Darbandi P., Pourboghrat F., Lee T. –K., and Liu K. –C., 2011, The role of elastic and plastic anisotropy of Sn on microstructure and damage evolution in lead-free solder joints, Reliability Physics Symposium (IRPS), 2011 IEEE International, 5F.1.1-5F.1.9

Bieler T. R., Zhou B., Blair L., Zamiri A., Darbandi P., Pourboghrat F., Lee T. –K., and Liu K. –C., 2012, The role of elastic and plastic anisotropy of Sn in recrystallization and damage evolution during thermal cycling in SAC305 solder joints, J ELECTRON MATER, Vol. 41, No. 2, 283-301

Borgesen P., Bieler T., Lehman L. P., and Cotts E. J., 2007, Pb-free solder: new materials considerations for microelectronics processing, MRS BULL, Vol. 32, No. 4, 360-365

Chen H., Mueller M., Mattila T. T., Li J., Liu X., Wolter K. –J., and Paulasto-Kröckel M., 2011, Localized recrystallization and cracking of lead-free solder interconnections under thermal cycling, J MATER RES, Vol. 26, No. 16, 2103-2116

Chen H., Han J., and Li M., 2011b, Localized recrystallization induced by subgrain rotation in Sn-3.0Ag-0.5Cu ball grid array solder interconnects during thermal cycling, J ELECTRON MATER, Vol. 40, No. 12, 2470-2479

Chen H., Wang L., Han J., Li M. Y., Wu Q. B., and Kim J. M., 2011c, Grain orientation evolution and deformation behaviors in Pb-free interconnects under mechanical stresses, J ELECTRON MATER, Vol. 40, No. 12, 2445-2457

Chen H., Li J., and Li M., 2012, Dependence of recrystallization on grain morphology of Sn-based solder interconnects under thermomechanical stress, J ALLOY COMPD, Vol. 540, 32-35

Chen K., Tamura N., Kunz M., Tu K. N., and Lai Y. –S., 2009, In situ measurement of electromigration-induced transient stress in Pb-free Sn-Cu solder joints by synchrotron radiation based x-ray polychromatic microdiffraction, J APPL PHYS, Vol. 106, 023502

Choi S., Subramanian K. N., Lucas J. P., and Bieler T. R., 2000, Thermomechanical fatigue behavior of Sn-Ag solder joints, J ELECTRON MATER, Vol. 29, No. 10, 1249-1257

Choi W. J., Lee T. Y., Tu K. N., Tamura N., Celestre R. S., MacDowell A. A., Bong Y. Y., and Nguyen L., 2003, Tin whisker studied by synchrotron radiation scanning X-ray micro-diffraction, ACTA MATER, Vol. 51, No. 20, 6253-6261

Chu S. N. G. and Li J. C. M., 1979, Impression creep of β-Tin single crystals, MATER SCI ENG, Vol. 39, No. 1, 1-10

Coombs C. F. Jr., 2008, Printed Circuits Handbook, Fifth Edition, The McGraw-Hill Companies

Daymond M. R. and Withers P. J., 1996, A synchrotron radiation study of transient internal strain changes during the early stages of thermal cycling in an Al/SiCw MMC, SCRIPTA MATER, Vol. 35, No. 10, 1229-1234

Dingley D. J. and Babakishi K., 1986, Use of electron back scatter diffraction patterns for determination of crystal symmetry elements, SCAN ELECTRON MICROS, Vol. 2, 383-391

Doherty R.D., Hughes D. A., Humphreys F. J., Jonas J. J., Jensen D. J., Kassner M. E., King W. E., McNelley T. R., McQueen H. J., and Rollett A. D., 1997, Current issues in recrystallization: a review, MAT SCI ENG A-STRUCT, Vol. 238, No. 2, 219-274

Düzgün B. and Aytaş I., 1993, Investigation of operative slip system in β-Sn single crystal and the relation between the crystal orientation and the slip systems, JPN J APPL PHYS, Vol. 32, No. 7, 3214-3216

Düzgün B., Ekinci A. E., Karaman I., and Ucar N., 1999, Investigation of dislocation movements and deformation characteristics in β-Sn single crystals, J MECH BEHAV MATER, Vol. 10, No. 3, 187-203

Dyson B. F., Anthony T. R., and Turnbull D., 1967, Interstitial diffusion of copper in tin, J APPL PHYS, Vol. 38, No. 8, 3408

Elmer J. W., Specht E. D., and Kumar M., 2010, Microstructure and in situ observations of undercooling for nucleation of β-Sn relevant to lead-free solder arrays, J ELECTRON MATER, Vol. 39, No. 3, 273-282

EPA, 2005, Solders in electronics: a life-cycle assessment summary, EPA-744-S-05-001

Fiedler R. and Lang A. R., 1972, Dislocation generation at surfaces of tin single crystals, J MATER SCI, Vol. 7, No. 5, 531-542

Fiedler R. and Vagera I., 1975, On the Burgers vectors in β-Sn single crystals, PHYS STATUS SOLIDI A, Vol. 32, No. 2, 419-424

Fit2d2maud, http://merkel.zoneo.net/Fit2d2maud/instructions.php

Foreman A. J. E. and Lomer W.M., 1955, Dislocation energies and choice of slip plan in face-centered cubic metals, PHILOS MAG, Vol. 46, No. 372, 73-76

Frear D. R., Jang J. W., Lin J. K., and Zhang C., 2001, Pb-free solders for flip-chip interconnects, JOM-J MIN MET MAT S, Vol. 53, No. 6, 28-32

Fujiwara M. and Hirokawa T., 1987, The strength of main obstacles to dislocation motion in white tin crystals, J JPN I MET, Vol. 51, No. 9, 830-838

Glazer J., 1994, Microstructure and mechanical properties of Pb-free solder alloys for low-cost electronic assembly: a review, J ELECTRON MATER, Vol. 23, No. 8, 693-700

Gong J., Liu C., Conway P. P., and Silberschmidt V. V., 2009, Formation of Sn dendrites and SnAg eutectics in a SnAgCu solder, SCRIPTA MATER, Vol. 61, No. 7, 682-685

Hales S. J., McNelley T. R., and McQueen H. J., 1991, Recrystallization and superplasticity at 300 ℃ in an aluminum-magnesium alloy, METALL MATER TRANS A, Vol. 22, No. 5, 1037-1047

Handwerker C. A., Kattner U., Moon K., Bath J., Bradley E. and Snugovsky P., 2007, Alloy Selection, in Lead-Free Electronics: iNEMI Projects Lead to Successful Manufacturing (eds E. Bradley, C. A. Handwerker, J. Bath, R. D. Parker and R. W. Gedney), John Wiley & Sons, Inc., Hoboken, NJ, USA

Henderson D. W., Gosselin T., Sarkhel A., Kang S. K., Choi W. –K., Shih D. –Y, Goldsmith C., and Puttilitz K. J., 2002, Ag_3Sn plate formation in the solidification of near ternary eutectic Sn-Ag-Cu alloys, J MATER RES, Vol. 17, No. 11, 2775-2778

Henderson D. W., Woods J. J., Gosselin T. A., Bartelo J., King D. E., Korhonen T.M., Korhonen M.A., Lehman L.P., Cotts E.J., Kang S. K., Lauro P., Shih D.-Y., Goldsmith C. and Puttlitz K. J., 2004, The microstructure of Sn in near-eutectic Sn–Ag–Cu alloy solder joints and its role in thermomechanical fatigue, J MATER RES, Vol. 19, No. 6, 1608-1612

Honda K., 1978, Configuration, formation and Burgers vector of coupled dislocations straddling a polygon wall in white tin single crystals, JPN J APPL PHYS, Vol. 17, No. 1, 33-41

Honda K., 1979, Dislocation walls consisting of double arrays in white tin single crystals, JPN J APPL PHYS, Vol. 18, No. 2, 215-224

Honda K., 1987, Dislocation reactions in a boundary of a white tin crystal, JPN J APPL PHYS, Vol. 26, No. 4, 637-638

Hornbogen E., 1979, Combined reactions, METALL MATER TRANS A, Vol. 10, No. 8, 947-972

Hua F., Mei Z., and Glazer J., 1998, Eutectic Sn-Bi as an alternative to Pb-free solders, ELEC COMP C, 48th IEEE, 277-283

Humphreys F. J. and Hatherly M., 2004, Recrystallization and related annealing phenomena, second edition, ELSEVIER Ltd, Kidlington, Oxford, UK

Ice G. E., Larson B. C., Tischler J. Z., Liu W., and Yang W., 2005, X-ray microbeam measurements of subgrain stress distributions in polycrystalline materials, MAT SCI ENG A-STRUCT, Vol. 399, No. 1-2, 43-48

Ice G. E. and Barabash R. I., 2007, White beam microdiffraction and dislocation gradients, in Dislocation in Solids (eds Nabarro F. R. N. and Hirth J. P.), Elsevier B. V.

Kang S. K. and Sarkhel A. K., 1994, Lead (Pb) – free solders for electronic packaging, J ELECTRON MATER, Vol. 23, No. 8, 701-707

Kang S. K., Choi W. K., Shih D. –Y., Henderson D. W., Gosselin T., Sarkhel A. Goldsmith C., and Puttlitz K. J., 2003, Formation of Ag_3Sn plates in Sn-Ag-Cu alloys and optimization of their alloy composition, ELEC COMP C, 53rd IEEE, 64-70

Kang S. K., Lauro P. A., Shih D. –Y., Henderson D. W., and Puttlitz K. J., 2005, Microstructure and mechanical properties of lead-free solders and solder joints used in microelectronic applications, IBM J RES DEV, Vol. 49, No. 4/5, 607-620

Kattner U. R. and Boettinger W. J., 1994, On the Sn-Bi-Ag ternary phase diagram, J ELECTRON MATER, Vol. 23, No. 7, 603-610

Kinyanjui R., Lehman L. P., Zavalij L., and Cotts E., 2011, Effect of sample size on the solidification temperature and microstructure of SnAgCu near eutectic alloys, J MATER RES, Vol. 20, No. 11, 2914-2918

Korhonen T. M., Lehman L., Korhonen M., and Henderson D., 2007, Isothermal fatigue behavior of the near-eutectic Sn-Ag-Cu alloy between -25 ℃ and 125 ℃, J ELECTRON MATER, Vol. 36, No. 2, 173-178

Korsunsky A. M., Wells K. E., and Withers P. J., 1998, Mapping two –dimensional state of strain using synchrotron X-ray diffraction, SCRIPTA MATER, Vol. 39, No. 12, 1705-1712

Krieger Lassen N. C., Conradsen K., and Juul Jensen D., 1992, Image processing procedures for analysis of electron back scattering patterns, SCANNING MICROSCOPY, Vol. 6, 115-121

Larson B. C., Yang W., Ice G. E., Budai J. D., and Tischler J. Z., 2002, Three dimensional X-ray structural microscopy with submicrometre resolution, NATURE, Vol. 415, No. 6874, 887-890

Larsson A. –K., Stenberg L., and Lidin S., 1994, The superstructure of domain-twinned η’-Cu_6Sn_5, ACTA CRYSTALL B-STRU, Vol. B50, 636-643

Lee A., Liu W., Ho C. E., and Subramanian K. N., 2007, Synchrotron X-ray microscopy studies on electromigration of a two-phase material, J APPL PHYS, Vol. 102, 053507

Lee J. G., Telang A., Subramanian K. N., and Bieler T. R., 2002, Modeling thermomechanical fatigue behavior of Sn-Ag solder joints, J ELECTRON MATER, Vol. 31, No. 11, 1152-1159

Lee K., Kim K. –S., Tsukada Y., Suganuma K., Yamanaka K., Kuritani S., and Ueshima M., 2011, Effects of the crystallographic orientation of Sn on the electromigration of Cu/Sn-Ag-Cu/Cu ball joints, J MATER RES, Vol. 26, No. 3, 467-474

Lee T. –K., Liu K. –C., and Bieler T. R., 2009, Microstructure and orientation evolution of the Sn phase as a function of position in ball grid arrays in Sn-Ag-Cu solder joints, J ELECTRON MATER, Vol. 38, No. 12, 2685-2693

Lee T. –K., Zhou B., Blair L., Liu K. –C., and Bieler T. R., 2010, Sn-Ag-Cu solder joint microstructure and orientation evolution as a function of position and thermal cycles in ball grid arrays using orientation imaging microscopy, J ELECTRON MATER, Vol. 39, No. 12, 2588-2597

Lee T. –K., Xie W., Zhou B., Bieler T., and Liu K. –C., 2011, Impact of isothermal aging on long-term reliability of fine-pitch ball grid array packages with Sn-Ag-Cu solder interconnects: die size effects, J ELECTRON MATER, Vol. 40, No. 9, 1967-1976

Lee T. –K., Liu B., Zhou B., Bieler T., and Liu K. –C., 2011b, Correlation between Sn grain orientation and corrosion in Sn-Ag-Cu solder interconnects, J ELECTRON MATER, Vol. 40, No. 9, 1895-1902

Lee T. –K., Zhou B., Bieler T., and Liu K. –C., 2011c, Impact of microstructure evolution and isothermal aging on Sn-Ag-Cu solder interconnect board-level high-G mechanical shock performance and crack Propagation, J ELECTRON MATER, Vol. 41, No. 2, 273-282

Lee T. –K., Ma H., 2012, Aging impact on the accelerated thermal cycling performance of lead-free BGA solder joints in various stress conditions, ELEC COMP C, 62nd IEEE, 477-482

Lee T. –K., Zhou B., and Bieler T. R., 2012b, Impact of isothermal aging and Sn grain orientation on the long-term reliability of wafer-level chip-scale package Sn-Ag-Cu solder interconnects, IEEE T COMPON PACK T, Vol. 2, No. 3, 496-501

Lehman L. P., Athavale S. N., Fullem T. Z., Giamis A. C., Kinyanjui R. K., Lowenstein M., Mather K., Patel R., Rae D., Wang J., Xing Y., Zavalij L., Borgesen P., and Cotts E. J., 2004, Growth of Sn and intermetallic compounds in Sn-Ag-Cu solder, J ELECTRON MATER, Vol. 33, No. 12, 1429-1439

Lehman L. P., Xing Y., Bieler T. R., and Cotts E. J., 2010, Cyclic twin nucleation in tin-based solder alloys, ACTA MATER, Vol. 58, No. 10, 3546-3556

Li J., Karppinen J., Laurila T., and Kivilahti J. K., 2009, Reliability of lead-free solder interconnections in thermal and power cycling tests, IEEE T COMPON PACK T, Vol. 32, No. 2, 302-308

Li J., Mattila T. T., and Kivilahti J. K., 2010, Multiscale simulation of microstructural changes in solder interconnections during thermal cycling, J ELECTRON MATER, Vol. 39, No. 1, 77-84

Li J., Xu H., Mattila T. T., Kivilahti J. K., Laurila T., and Paulasto-Kröckel M., 2010b, Simulation of dynamic recrystallization in solder interconnections during thermal cycling, COMP MATER SCI, Vol. 50, No. 2, 690-697

Lin W. H., Wu A. T., Lin S. Z., Chuang T. H., and Tu K. N., 2007, Electromigration in the flip chip solder joint of Sn-8Zn-3Bi on copper pads, J ELECTRON MATER, Vol. 36, No. 7, 753-759

Liu W., Ice G. E., Larson B. C., Yang W., Tischler J. Z., and Budai J. D., 2004, The three-dimensional X-ray crystal microscope: A new tool for materials characterization, METALL MATER TRANS A, Vol. 35, No. 7, 1963-1967

Liu W., Ice G. E., Larson B. C., Yang W., and Tischler J. Z., 2005, Nondestructive three-dimensional characterization of grain boundaries by X-ray crystal microscopy, ULTRAMICROSCOPY, Vol. 103, No. 3, 199-204

Liu, J., Salmela, O., Sarkka, J., Morris, J. E., Tegehall, P. –E., and Andersson, C., 2011, Reliability of Microtechnology, Interconnects, Devices and Systems, Springer Science+Business Media, LLC

Loomans, M. E. and Fine, M. E., 2000, Tin-silver-copper eutectic temperature and composition, METALL MATER TRANS A, Vol. 31A, No. 4, 1155-1162

Lu M., Shih D. –Y., Lauro P., Goldsmith C., and Henderson D. W., 2008, Effect of Sn grain orientation on electromigration degradation mechanism in high Sn-based Pb-free solders, APPL PHYS LETT, Vol. 92, No. 21, 211909

Lyman T., 1961, Metals Handbook (eds Lyman T., Boyer H. E., Foster J. E., Hontas J. P., and Lawton H.), American society for metals, Metals Park, Ohio

Lyon K. G., Salinger G. L., Swenson C. A., and White G. K., 1977, Linear thermal expansion measurements on silicon from 6 to 340K, J APPL PHYS, Vol. 48, No. 3, 865-868

Matin M. A., Coenen E. W. C., Vellinga W. P., and Geers M. G. D., 2005, Correlation between thermal fatigue and thermal anisotropy in a Pb-free solder alloy, SCRIPTA MATER, Vol. 53, No. 8, 927-932

Matin M. A., Vellinga W. P., and Geers M. G. D., 2006, Microstructure evolution in a Pb-free solder alloy during mechanical fatigue, MAT SCI ENG A-STRUCT Vol. 431, No. 1-2, 166-174

Matin M. A., Vellinga W. P., and Geers M. G. D., 2007, Thermomechanical fatigue damage evolution in SAC solder joints, MAT SCI ENG A-STRUCT Vol. 445-446, 73-85

Mattila T. T., Vuorinen V., and Kivilahti J. K., 2004, Impact of printed wiring board coatings on the reliability of lead-free chip-scale package interconnections, J MATER RES, Vol. 19, No. 11, 3214-3223

Mattila T.T., Mueller M., Paulasto-Kröckel M., and Wolter K.-J. , 2010, Failure mechanism of solder interconnections under thermal cycling conditions, ELECTRONIC SYSTEM-INTEGRATION TECHNOLOGY CONFERENCE, 3rd ESTC, 1-8

Mattila T. T., Xu H., Ratia O., and Paulasto-Kröckel M., 2010b, Effects of thermal cycling parameters on lifetimes and failure mechanism of solder interconnections, ELEC COMP C, 60th IEEE, 581-590

Mattila T.T. and Paulasto-Kröckel M, 2011, Toward comprehensive reliability assessment of electronics by a combined load approach, MICROELECTRON RELIAB, Vol. 51, No. 6, 1077-1091

Mattila T. T. and Kivilahti J. K., 2012, The failure mechanism of recrystallization-assisted cracking of solder interconnections, in Recrystallization (eds Sztwiertnia K.), InTech, Janeza Trdine 9, 51000 Rijeka, Croatia

Miettinen S., 2005, Recrystallization of lead-free solder joints under mechanical load, Master's Thesis

Mills D. M., 2002, Third-generation hard X-ray synchrotron radiation sources: Source properties, Optics, and Experimental Techniques, John Wiley and Sons

Moon K., Boettinger W., Kattner U., Biancaniello F., and Handwerker C., 2000, Experimental and thermodynamic assessment of Sn-Ag-Cu solder alloys, J ELECTRON MATER, Vol. 29, No. 10, 1122-1136

Nagasaka M., 1989, Temperature dependence of plastic deformation in white tin single crystals, JPN J APPL PHYS, Vol. 28, No. 3, 446-452

Nishikawa S. and Kikuchi S., 1928, Diffraction of cathode rays by Mica, NATURE, Vol. 121, 1019-1020

Noh B. –I., Yoon J. –W., Ha S. –O., and Jung S. –B., 2011, Effects of different kinds of underfills and temperature-humidity treatments on drop reliability of board-level packages, J ELECTRON MATER, Vol. 40, No. 2, 224-231

Obinata J. and Schmid E., 1933, Über die Dehnung von Zinnkristallen, Z PHYS, Vol. 82, No. 3-4, 224-234

Ojima K. and Hirokawa T., 1983, Motion of individual dislocations in white tin single crystal deformed in tension, JPN J APPL PHYS, Vol. 22, No. 1, 46-51

Park S., Dhakal R., Lehman L., and Cotts E., 2007, Measurement of deformations in SnAgCu solder interconnects under in situ thermal loading, ACTA MATER, Vol. 55, No. 9, 3253-3260

Peng W. and Marques M. E., 2007, Effect of thermal aging on drop performance of chip scale packages with SnAgCu solder joints on Cu pads, J ELECTRON MATER, Vol. 36, No. 12, 1679-1690

Qasaimeh A., Jaradat Y., Wentlent L., Yang L., Yin L., Arfaei B., and Borgesen P., 2011, Recrystallization behavior of lead-free and lead containing solder in cycling, ELEC COMP C, 61st IEEE , 1775-1781

Sector 34-ID-E: http://www.aps.anl.gov/Sectors/33_34/microdiff/downloads/

Seo S. –K., Kang S. K., Cho M. G., Shih D. –Y., and Lee H. M., 2009, The crystal orientation of β-Sn grains in Sn-Ag and Sn-Cu solders affected by their interfacial reactions with Cu and Ni(P) under bump metallurgy, J ELECTRON MATER, Vol. 38, No. 12, 2461-2469

Seo S. –K., Cho M. G., and Lee H. M., 2010, Crystal orientation of β-Sn grain in Ni(P)/Sn-0.5Cu/Cu and Ni(P)/Sn-1.8Ag/Cu joints, J MATER RES, Vol. 25, No. 10, 1950-1957

Shnawah D. A., Sabri M. F. M., and Badruddin I. A., 2012, A review on thermal cycling and drop impact reliability of SAC solder joint in portable electronic products, MICROELECTRON RELIAB, Vol. 52, No. 1, 90-99

Sidhu R. S., Madge S. V., Deng X., and Chawla N., 2007, On the nature of the interface between Ag_3Sn intermetallic and Sn in Sn-3.5Ag solder alloys, J ELECTRON MATER, Vol. 36, No. 12, 1615-1620

Sidhu R. S. and Chawla N., 2008, Thermal fatigue behavior of Sn-Rich (Pb-free) solders, METALL MATER TRANS A, Vol. 39, No. 4, 799-810

Sobiech M., Wohlschlogel M., Welzel U., Mittemeijer E. J., Hugel W., Seekamp A., Liu W., and Ice G. E., 2009, Local, submicron, strain gradients as the cause of Sn whisker growth, APPL PHYS LETT, Vol. 94, No.22, 221901

Sundelin J. J., Nurmi S. T.,and Lepistö T. K., 2008, Recrystallization behavior of SnAgCu solder joints, MAT SCI ENG A-STRUCT, Vol. 474, No. 1-2, 201-207

Telang A. U., Bieler T. R., Choi S., and Subramanian K. N., 2002, Orientation imaging studies of Sn-based electronic solder joints, J MATER RES, Vol. 17, No. 9, 2294-2306

Telang A. U., Bieler T. R., Lucas J. P., Subramanian K. N., Lehman L. P., Xing Y., and Cotts E. J., 2004, Grain-boundary character and grain growth in bulk tin and bulk lead-free solder alloys, J ELECTRON MATER, Vo. 33, No. 12, 1412-1423

Telang A. U., 2004b, Dissertation: Characterization of deformation in Sn-Ag lead-free solders during thermomechanical fatigue using orientation imaging microscopy, ProQuest Dissertations and Theses

Telang A. U. and Bieler T. R., 2005, The orientation imaging microscopy of lead-free Sn-Ag solder joints, JOM-J MIN MET MAT S, Vol. 57, No. 6, 44-49

Telang A. U., Bieler T. R., and Crimp M. A., 2006, Grain boundary sliding on near-7°, 14°, and 22° special boundaries during thermomechanical cycling in surface-mount lead-free solder joint specimens, MAT SCI ENG A-STRUCT, Vol. 421, No. 1-2, 22-34

Telang A. U., Bieler T. R., Zamiri A., and Pourboghrat F., 2007, Incremental recrystallization/ grain growth driven by elastic strain energy release in a thermomechanically fatigued lead-free solder joint, ACTA MATER, Vol. 55, No. 7, 2265-2277

Terashima S., Kariya Y., Hosoi T., and Tanaka M., 2003, Effect of silver content on thermal fatigue life of Sn-xAg-0.5Cu flip-chip interconnects, J ELECTRON MATER, Vol. 32, No. 12, 1527-1533

Terashima S., Kariya Y., and Tanaka M., 2004, Improvement on thermal fatigue properties of Sn-1.2Ag-0.5Cu flip chip interconnects by nickel addition, MATER TRANS, Vol. 45, No. 3, 673-680

Terashima S., Takahama K., Nozaki M., and Tanaka M., 2004b, Recrystallization of Sn grains due to thermal strain in Sn-1.2Ag-0.5Cu-0.05Ni solder, MATER TRANS, Vol. 45, No. 4, 1383-1390

Terashima S., Kohno T., Mizusawa A., Arai K., Okada O., Wakabayashi T., Tanaka M., and Tatsumi K., 2009, Improvement of Thermal Fatigue Properties of Sn-Ag-Cu Lead-Free Solder Interconnects on Casio's Wafer Level Packages Based on Morphology and Grain Boundary Character, J ELECTRON MATER, Vol. 38, No.1, 33-38

Trumble B., 1998, Get the lead out! [lead free solder], IEEE SPECTRUM, Vol. 35, No. 5, 55-60

Tu K. N., Chen C., and Wu A. T., 2007, Stress analysis of spontaneous Sn whisker growth, J MATER SCI-MATER E, Vol. 18, No. 1-3, 269-281

Tyson W., 1967, Basal and prismatic slip in h.c.p. crystals, ACTA METALL MATER, Vol. 15, No. 3, 574-577

Tyte L. C., 1938, The rate of viscous flow of metals: Part 1, tin, P PHYS SOC, Vol. 50, No. 2, 153-175

Ulrich R. K. and Brown W. D., 2006, Advanced Electronic Packaging, 2nd Edition, Wiley-IEEE Press

Wanner A. and Dunand D. C., 2000, Synchrotron X-ray study of bulk lattice strains in externally loaded Cu-Mo composites, METALL MATER TRANS A, Vol. 31A, No. 11, 2949-2962

Wanner A. and Dunand D. C., 2001, Methodological aspects of the high-energy synchrotron X-ray diffraction technique for internal stress evaluation, Journal of Neutron Research, Vol. 9, No. 2-4, 495-501

Watanabe T., 1993, Grain boundary design and control for high temperature materials, MAT SCI ENG A-STRUCT, Vol. 166, No. 1-2, 11-28

Watanabe T., Tsurekawa S., Kobayashi S., and Yamaura S., 2005, Structure-dependent grain boundary deformation and fracture at high temperatures, MAT SCI ENG A-STRUCT, Vol. 410-411, 140-147

Weaver R., 2003, Rediscovering polarized light microscopy, AM LAB, Vol. 35, No. 20, 55-61

Weertman J. and Breen J. E., 1956, Creep of tin single crystal, J APPL PHYS, Vol. 27, No. 10, 1189-1193

Westgren A. and Phragmén G., 1928, Röntgenanalyse der Kupfer–Zinnlegierungen, Z ANORG ALLG CHEM, Vol. 175, No.1, 80-89

Wright S. I. and Adams B. L., 1992, Automatic analysis of electron backscattering patterns, METALL MATER TRANS A, Vol. 23, No. 3, 759-767

Wright S. I., 2000, Fundamentals of automated EBSD, in Electron backscatter diffraction in Materials Science (eds Schwartz A. J., Kumar M., and Adams B. L.), New York: Kluwer Academic

Wu G. and Zaefferer S., 2009, Advances in TEM orientation microscopy by combination of dark-field conical scanning and improved image matching, ULTRAMICROSCOPY, Vol. 109, No. 11, 1317-1325

Yang S., Tian Y., and Wang C., 2010, Investigation on Sn grain number and crystal orientation in the Sn-Ag-Cu/Cu solder joints of different sizes, J MATER SCI-MATER E, Vol. 21, No. 11, 1174-1180

Yeh D. C. and Huntington H. B., 1984, Extreme fast-diffusion system: nickel in single-crystal tin, PHYS REV LETT, Vol. 53, No. 15, 1469-1472

Yin L., Wentlent L., Yang L., Arfaei B., Oasaimeh A., and Borgesen P., 2012, Recrystallization and precipitate coarsening in Pb-free solder joints during themomechanical fatigue, J ELECTRON MATER, Vol. 41, No. 2, 241-252

Zeng K. and Tu K. N., 2002, Six cases of reliability study of Pb-free solder joints in electronic packaging technology, MAT SCI ENG R, Vol. 38, No. 2, 55-105

Zhou B., Bieler T. R., Wu G., Zaefferer S. , Lee T. –K., and Liu K. –C., 2009, Characterization of Microstructure and internal strain (stress) evolution during thermal cycling, INTERNATIONAL SYMPOSIUM ON MICROELECTRONICS PROCEEDINGS, 42nd IMAPS

Zhou B., Bieler T. R., Lee T. –K., and Liu K. –C., 2009b, Methodology for analyzing slip behavior in ball grid array lead-free solder joints after simple shear, J ELECTRON MATER, Vol. 38, No. 12, 2702-2711

Zhou B., Bieler T. R., Lee T. –K., and Liu K. –C., 2010, Crack development in a low-stress PBGA package due to continuous recrystallization leading to formation of orientations with [001] parallel to the interface, J ELECTRON MATER, Vol. 39, No. 12, 2669-2679

Zhou B., Bieler T. R., Wu G., Zaefferer S., Lee T. –K., and Liu K. –C., 2012, In situ synchrotron characterization of melting, dissolution, and resolidification in lead-free solders, J ELECTRON MATER, Vol. 41, No. 2, 262-272

Zhou B., Bieler T. R., Lee T. –K., and Liu W., 2012b, Characterization of recrystallization and microstructure evolution in lead-free solder joints using EBSD and 3D-XRD, J ELECTRON MATER, DOI: 10.1007/s11664-012-2307-z

Zhu L. and Marcinkiewicz W., 2005, Drop impact reliability analysis of CSP packages at board and product levels through modeling approaches, IEEE T COMPON PACK T, Vol. 28, No. 3, 449-456